

# VU Research Portal

## Optically and Electrically assisted Micro-Indentation

Marrese, Marica

2021

### **document version**

Publisher's PDF, also known as Version of record

[Link to publication in VU Research Portal](#)

### **citation for published version (APA)**

Marrese, M. (2021). *Optically and Electrically assisted Micro-Indentation*.

### **General rights**

Copyright and moral rights for the publications made accessible in the public portal are retained by the authors and/or other copyright owners and it is a condition of accessing publications that users recognise and abide by the legal requirements associated with these rights.

- Users may download and print one copy of any publication from the public portal for the purpose of private study or research.
- You may not further distribute the material or use it for any profit-making activity or commercial gain
- You may freely distribute the URL identifying the publication in the public portal ?

### **Take down policy**

If you believe that this document breaches copyright please contact us providing details, and we will remove access to the work immediately and investigate your claim.

### **E-mail address:**

[vuresearchportal.ub@vu.nl](mailto:vuresearchportal.ub@vu.nl)

# **Optically and Electrically assisted Micro-Indentation**

This thesis was reviewed by:

prof. dr. Davide Iannuzzi

Vrije Universiteit, Amsterdam  
Amsterdam, The Netherlands

prof. dr. ir. G.J.L. Wuite

Vrije Universiteit Amsterdam, BETA, Fysica  
van Levende Systemen

prof.dr. A.G.J.M. van Leeuwen

Universiteit van Amsterdam, AMC

prof.dr. F.P. Battaglia

Radboud Universiteit Nijmegen

Dr. M. Vassalli

University of Glasgow

Dr. S. Thorsteinsdottir

University of Lisbon

© 2020, Marica Marrese. All rights reserved. No part of this thesis may be reproduced or transmitted in any form or by any means without permission from the author.

Printed by RIDDERPRINT

A digital version of this thesis is available at [www.ubvu.vu.nl](http://www.ubvu.vu.nl).

The research in this thesis was performed in the Biophotonics and Medical Imaging section of the Department of Physics and Astronomy and LaserLaB at the VU University Amsterdam.

VRIJE UNIVERSITEIT

**OPTICALLY AND ELECTRICALLY ASSISTED-MICRO-  
INDENTATION**

ACADEMISCH PROEFSCHRIFT

ter verkrijging van de graad Doctor aan  
de Vrije Universiteit Amsterdam,  
op gezag van de rector magnificus  
prof.dr. V. Subramaniam,  
in het openbaar te verdedigen  
ten overstaan van de promotiecommissie  
van de Faculteit der Bètawetenschappen  
op maandag 25 januari 2021 om 13.45 uur  
in de online bijeenkomst van de universiteit,  
De Boelelaan 1105

door

Marica Marrese

geboren te Piedimonte Matese (Ce), Italia, Italië

promotor:

prof.dr. D. Iannuzzi



# Contents

<b>CHAPTER 1  -----</b>	<b>5</b>
-------------------------	----------

<b>INTRODUCTION-----</b>	<b>5</b>
--------------------------	----------

<b>1.1 Introduction to biomechanics .....</b>	<b>6</b>
1.1.1 Measure tissue mechanical properties-----	7
1.1.2 Ferrule-Top micro-indentation -----	9
<b>1.2 Optically assisted micro-indentation .....</b>	<b>10</b>
1.2.1 Optical Coherence Tomography -----	11
1.2.2 Common-Path OCT -----	13
<b>1.3 Electrically assisted micro-indentation .....</b>	<b>14</b>
1.3.1 HD-MEAs-----	14
<b>1.4 Scope and relevance of the thesis .....</b>	<b>16</b>
<b>1.5 Outline of the thesis .....</b>	<b>17</b>

<b>CHAPTER 2  -----</b>	<b>20</b>
-------------------------	-----------

<b>MICRO-INDENTATION AND OPTICAL COHERENCE TOMOGRAPHY FOR THE MECHANICAL CHARACTERIZATION OF EMBRYOS: EXPERIMENTAL SETUP AND MEASUREMENTS ON CHICKEN EMBRYOS-----</b>	<b>20</b>
---	-----------

<b>2.1 Introduction.....</b>	<b>21</b>
<b>2.2 Materials and Methods .....</b>	<b>23</b>
2.2.1 Chicken embryo cultures -----	23
2.2.2 Experimental setup-----	25
2.2.3 Indentation protocol and data analysis-----	27
2.2.4 Optical Coherence Tomography -----	27
2.2.5 Statistics -----	28
<b>2.3 Results .....</b>	<b>28</b>
<b>2.4 Discussion and conclusion.....</b>	<b>36</b>

<b>CHAPTER 3  -----</b>	<b>42</b>
-------------------------	-----------

<b>IN VIVO CHARACTERIZATION OF CHICK EMBRYO MESODERM BY OPTICAL COHERENCE TOMOGRAPHY ASSISTED</b>	
---	--

## **MICROINDENTATION----- 42**

3.1	Introduction.....	43
3.2	Material and Methods.....	44
3.2.1	Chicken embryo cultures-----	44
3.2.2	Experimental setup-----	44
3.3	Results and Discussion.....	48
3.4	Conclusion .....	53
3.5	Supplementary figures .....	54

## **CHAPTER 4 | ----- 58**

### **ULTRATHIN OPTICAL PROBES FOR COMMON PATH OPTICAL COHERENCE TOMOGRAPHY ----- 58**

4.1	Introduction.....	59
4.2	Material and Methods.....	59
4.2.1	Experimental details -----	59
4.3	Results and discussion .....	61
4.4	Conclusion .....	66
4.5	Supplementary material .....	67
4.6	Notes .....	68
4.6.1	Axicon vs. 20 $\mu$ m microlenses -----	68
4.6.2	75 $\mu$ m polystyrene microspheres-----	71
4.6.3	Conclusion -----	73

## **CHAPTER 5 | ----- 76**

### **INDENTATION PROBE WITH OPTICAL FIBER ARRAY FOR OPTICAL COHERENCE TOMOGRAPHY----- 76**

5.1	Introduction.....	77
5.2	Material and Methods.....	78
5.2.1	Ferrule-Top sensor: design and fabrication-----	78
5.2.2	Experimental Setup -----	80
5.2.3	OCT calibration procedure -----	81
5.2.4	Sample preparation -----	81
5.3	Results .....	81
5.4	Discussion and conclusion.....	86
5.5	Supplementary figures .....	88



## **CHAPTER 6 | -----92**

### **INVESTIGATING THE EFFECTS OF MECHANICAL STIMULATION ON RETINAL GANGLION CELL SPONTANEOUS SPIKING ACTIVITY --- 92**

<b>6.1</b>	<b>Introduction.....</b>	<b>93</b>
<b>6.2</b>	<b>Material and Methods.....</b>	<b>95</b>
6.2.1	Ethics Statement -----	95
6.2.2	Experimental Setup -----	95
6.2.3	Indentation protocol for mechanical characterization -----	96
6.2.4	Retina electrophysiology -----	97
6.2.5	Experimental protocol for electrophysiological characterization -----	97
6.2.6	Data Analysis -----	99
6.2.7	Clustering of similar spiking activity -----	99
6.2.8	Classification of ON_OFF RGC cell types-----	99
6.2.9	Decision Tree Classifier -----	100
<b>6.3</b>	<b>Results .....</b>	<b>100</b>
6.3.1	Characterization of Mechanical Properties of the retina tissue -----	100
6.3.2	Mechanical indentation affects the spontaneous activity of retinal ganglion cells	102
6.3.3	HD-MEAS recordings-----	102
6.3.4	Mechanical stimulation determine correlated spiking activity-----	104
6.3.5	Processing of mechanical vs. visual sensory inputs -----	106
<b>6.4</b>	<b>Discussion.....</b>	<b>109</b>
<b>6.5</b>	<b>Supplementary figures .....</b>	<b>112</b>

## **CHAPTER 7 | ----- 114**

### **SUMMARY AND CONCLUSION ----- 114**

### **REFERENCES----- 120**

### **PUBLICATIONS LIST ----- 142**

### **ACKNOWLEDGMENTS----- 144**



# Chapter 1 |

## Introduction

This chapter is a preface of the thesis. It introduces the field of optical imaging and tissue mechanics. It provides the reader with a brief overview of the development of advanced methodologies to study the interaction between different fields and forces: optical, electrical, and mechanical. By combining the mechanical characterization of biological samples with optical and electrical techniques, one can open new paths to better explore the field of mechanotransduction and mechanosensing. This chapter also contains the scope and outline of the thesis.

## 1.1 Introduction to biomechanics

The human body is continuously exposed to a variety of external forces while performing a multitude of activities. Mechanical forces are thus involved in several aspects of biology, depending on the specific scale size under consideration: at the molecular scale [1] (i.e., protein folding and unfolding); at cellular scale (i.e., cell proliferation and differentiation); at tissue scale (growth and remodeling) [2]; and at organ scale (in locomotion) [3].

Probably the most straightforward application of biomechanics is at organ scale [4]. Most of the everyday actions, such as walking, running, and jumping, are, in fact, driven by biomechanics. During those activities, the muscles in our body generate forces that are transferred to the ground by bones and soft connective tissue [3]. To this end, each bone of our body is precisely molded to meet peculiar mechanical requirements to support specific extrinsic or intrinsic loads, depending on its location in the skeleton [5]. Moving down the length scale, tissues are also exposed to a myriad of forces, including compressive, tensile, fluid shear stress, and hydrostatic pressure, each of which plays an intricate part in the shaping, development, and maintenance of the tissue [6]. Embryogenesis and tissue development are two examples of how mechanics influences tissue formations and organization.

The role of mechanics is even more crucial at cellular level [7,8]. Cells are sensitive to their surrounding environment through mechanoreceptors that are present in the cell membrane. They can respond and transduce external mechanical inputs into biochemical and electrical signals that influence processes such as cell proliferation, adhesion, migration, and fate [9,10]. The ability of cells to migrate, differentiate, and proliferate based on mechanical cues is also essential in processes such as infections and inflammation [3].

Since cells have evolved to sense differences in intrinsic mechanical cues, including mechanosensitive transmembrane proteins such as integrin, receptors, and ion channels, it is evident that biomechanics plays a crucial role also at the molecular scale as well [11]. Here, mechanical cues, perceived as changing in strain, are able to alter protein conformation and to drive protein-protein interactions and membrane organization in diseases.

In light of what discussed above, it is not surprising that biomechanics also plays a role in some diseases such as atherosclerosis [12], osteoarthritis [13], osteoporosis[14], and cancer [15,16]. One example is glaucoma, where the elevated intraocular pressure leads to a pathological state, and the resulting biomechanical stresses can cause damages to the optic nerve, inducing a progressive loss of vision [17–19]. A second example is atherosclerosis – a common arterial disease in which stress distributions cause endothelial injuries and the formation of atherosclerotic plaque [12]. An increase in tissue stiffness is also the main characteristic of cancer [20]. In tumor tissues, the extracellular matrix (ECM) is extensively remodeled by an increase of collagen fibers density, thus

altering its stiffness [21].

The investigation of mechanical properties is, therefore, crucial for many research fields, including cell biology, tissue engineering, and medical diagnosis. Thus, in the past decade, biomechanics has been extensively explored to develop new advanced techniques able to probe and quantify the response of cells and tissue to external forces, ranging from microscopy-based tools to nano and micro- force sensors.

### 1.1.1 Measure tissue mechanical properties

Micro and nanoindentation [22–25] have been routinely used to investigate the mechanical properties of biological tissues, modified surfaces, and biomaterials, by measuring their response to an external load imposed by a probe with known geometry [24,25]. Simply put, the instrument measures the amount of force one needs to apply to obtain a certain deformation of the object. The main parameter derived from indentation experiments is the elastic modulus, which is formally defined as the ratio between stress and strain, with the aid of several analytical models. The first elastic model for indentation was developed by Hertz [26–28], and it describes the simple case of elastic deformation of two perfectly homogeneous smooth and curved surfaces touching each other under an imposed load [29]. The estimation of the elastic modulus from the force–deformation curves was determined for the Hertzian case by Doerner and Nix in 1986 [30,31]. The Hertzian contact model can be used under certain conditions: the material properties of the tip and the sample should be isotropic and homogeneous, and the normal contact of the two bodies should be adhesionless and frictionless. The contact geometry is assumed to be axisymmetric, smooth, and continuous, whereas the tip has to be spherical, undeformable, and infinitely stiff compared to the sample. In 1992, the Hertzian theory was redefined to account for the change in the contact area at different points in the unloading curve by Oliver and Pharr [32].

Over the years, the Hertz theory, which is still used today under certain constraints, has been extended to a range of indenter geometries by Sneddon [33] and further exploited for the case of adhesive contact. As a point in case, the effects of adhesion were considered by several groups in various contact mechanics models, such as the Derjaguin, Muller and Toporov (DMT) [34], Johnson, Kendall and Roberts (JKR) [35], and Maugis models [36–38]. These models analyze the changing of the contact shapes and stresses that occur when the surface energy and the adhesive forces in the proximity of the contact area are significant

However, the main limitations of the Hertzian theory are related to the assumption of the material properties under investigation: the sample should be, in fact, flat, homogeneous, isotropic. Furthermore, the theory is applicable only for time-independent material, which implies that the material can deform under the application of an external load and instantaneously resume its original (unstressed) shape when the

load is removed. These materials are known as elastic materials. However, many polymers and biological materials exhibit gradual deformation and recovery when they are subjected to loading and unloading. The response of such materials depends on the rate at which the external load is applied. This time-dependent material behavior is known as viscoelasticity. Viscoelasticity derived from two words: viscosity and elasticity. Viscosity is a fluid property and is a measure of resistance to flow. Elasticity, on the other hand, is a solid material property. Therefore, a viscoelastic material is one that possesses both fluid and solid properties [39]. In order to investigate viscoelastic materials, the well-known theory of contact mechanics (Hertzian theory) cannot be fully employed. However, there are several mathematical models that, assuming that the material behaves like a combination of springs and dashpots, are able to describe the mechanics of viscoelastic objects. Each model is different from another because of a different arrangement of the springs and dashpots to describe elastic and viscous components. The simplest models are three: the Kelvin-Voigt model, the Maxwell model, and the standard linear solid model [40,41]. Another interesting approach to evaluate the mechanics of a viscoelastic material is by performing a dynamic indentation test. In this case, a small force oscillation is superimposed to a constant loading [42,43], also known as dynamic mechanical analysis [44]. Here, an oscillating load is applied to the indentation probe, and the amplitude and phase shift between the peak values for the penetration and the prescribed load history is measured. With these two parameters, the complex modulus and the phase angle of the sample can be determined. The complex dynamic modulus ( $E^* = E' + i E''$ ) takes into account both the elastic and viscous contributions. The real part of the complex modulus is also known as storage modulus ( $E'$ ) and it is the in-phase stress-strain ratio, whereas the imaginary part called loss modulus ( $E''$ ) is the out-of-phase stress to strain ratio. The relative contribution of the moduli can be measured using the phase shift  $\varphi$  for an oscillatory strain response to stress (or vice versa):

$$E^* = \frac{\sigma}{\varepsilon} = \frac{\sigma_0}{\varepsilon_0} (\cos \varphi + i \sin \varphi);$$

This derivation of storage and loss modulus, given by Hebert et al. [45,46], uses Sneddon's equation to relate stress and strain to load an indentation. The derivation yields the following expression for dynamic moduli for a spherical indenter:

$$\begin{aligned} \frac{E'(\omega)}{1-\nu^2} &= \frac{F_0}{h_0} \cos \varphi \frac{\sqrt{\pi}}{2} \frac{1}{\sqrt{A}}; \\ \frac{E''(\omega)}{1-\nu^2} &= \frac{F_0}{h_0} \sin \varphi \frac{\sqrt{\pi}}{2} \frac{1}{\sqrt{A}}; \end{aligned}$$

where  $F_0$  is the amplitude of the dynamic load,  $h_0$  the amplitude of oscillatory

indentation depth,  $\varphi$  the phase shift between load and indentation, and  $A$  is the contact area. Performing a dynamic indentation test, it is thus possible to obtain both the storage and loss modulus and to characterize the material properties in terms of both elasticity and viscoelasticity.

1

### 1.1.2 Ferrule-Top micro-indentation

The local mechanical properties of soft biological materials are typically assessed via nano and micro-indentation [47]. Here, a nanometer size tip is mounted on the free-hanging end of a cantilever to indent the sample with a small force. By measuring the deflection of the cantilever, one can then obtain the elasticity or viscoelasticity of a various range of material at the nano and microscale [48]. Over the last ten years, our group has pioneered a new indentation protocol that has been tailored to precisely and locally map tissue viscoelasticity at those scales [49–56]. The technique relies on the use of ferrule-top probes, whose main components are a micro-machined glass ferrule, a gold-coated cantilever, and an optical fiber.

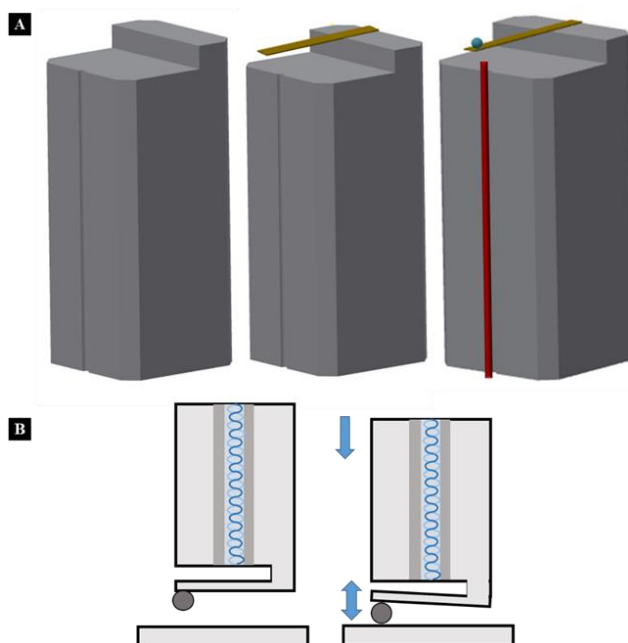


**Figure 1.1 | Ferrule-Top probe fabrication.**

(A) The building block of the probe is a borosilicate glass ferrule. The ferrule is cut to obtain a ridge on which an Au-coated cantilever is glued. The free ending of the cantilever is equipped with a glass bead. Next, a single-mode fiber (in red) is positioned on the top facet of the ferrule to form an interferometric cavity over which the cantilever deflection is measured (B).

In a nutshell, a ferrule top probe consists of a cantilever mounted on top of a glass ferrule with a small sphere attached to its free-hanging end. An optical fiber is then rigidly mounted on a groove on the top surface of the ferrule (Figure 1.1 A). The gap between the flat edge of the optical fiber and the gold-coated face of the cantilever creates an optical cavity. Specifically, part of the light coming out from the optical fiber is back-reflected from the fiber-to-air interface, whereas another portion of the light is reflected back from the gold-coated surface of the cantilever (Figure 1.1 B). The interference between the two reflected waves can thus be detected by an interferometer, acting as both light source and detector. High-frequency wavelength modulation is used to linearize the signal encoded by the detector and to quantify the deflection of the cantilever as described elsewhere [51,52,57].

## 1.2 Optically assisted micro-indentation

As argued above, the measurement of the mechanical properties of tissues can provide valuable information on the interplay between mechanics and the biology of living systems. Yet, it is undeniable that simultaneously investigating the morphological features of the investigated tissue, one could probably obtain a more complete picture of the occurring phenomenology. It is thus interesting to explore whether, by equipping ferrule-top indentation with microscopy technique, one could gain some new insight on mechanobiology.

Microscopes have always been one of the essential instruments for research in the biomedical field. The biological, medical, and material sciences would not be what they are today without the microscope. Optical imaging techniques, ranging from mesoscopic to microscopic levels, have been developed to provide a non-invasive and highly sensitive investigation of biological tissues with different spatial resolution, penetration depth, and contrast mechanisms. In the last decades, several medical imaging technologies have provided new opportunities to improve the diagnosis and the treatment of various diseases [58].

The impact of three-dimensional imaging technologies such as magnetic resonance imaging (MRI), X-ray computed tomography, radioisotope imaging (PET and SPECT), and ultrasound, for instance, can be seen as a milestone in clinical research due to their ability to understand the pathogenesis of multiple diseases and to provide new therapies and interventions [59–61]. Despite their success, however, each of these imaging techniques has limitations due to the low sensitivity and spatial resolution (in the range of half a millimeter), making the achievement of observing the smallest details at the disease site difficult. Optical imaging methods that do offer higher special resolution such as confocal, light sheet, fluorescence, and multi-photon microscopy are limited at imaging superficial tissue layers [58]. In this context, Optical Coherence Tomography (OCT) – a light-interference based optical technique – lies between the deep and the



superficial imaging techniques conveying high spatial resolution (10  $\mu\text{m}$  or less) at imaging depths of millimeters into the tissue. After its introduction in the late 1980's, Optical Coherence Tomography (OCT) was first suggested for medical diagnostic applications by Fercher et al. [62], who reported, for the first time, the ability of OCT to visualize deep tissues in the eye [63,64]. Further in vivo studies later demonstrated that OCT could detect many relevant pathologies in tissue, particularly in skin [65–67] and teeth [68], for neurological diseases [64,69–71], and in the vascular system [72–74]. Over the last decade, OCT has been further developed to enable high-resolution, real-time, and in-situ imaging of tissue microstructures without the need for tissue excision and processing. OCT has many important advantages over the existing clinical imaging modality, making it an essential complementary medical imaging tool. It is minimally invasive, noncontact, nonionizing, and it has a very high spatial resolution and sensitivity [75]. It provides high speed and real-time data acquisition. All these aspects widely justify the use of OCT in many research fields [63,76,77].

### 1.2.1 Optical Coherence Tomography

OCT is a light-based optical technique that allows the investigation of composite samples to obtain high-resolution 3D images with a spatial resolution of approximately 10  $\mu\text{m}$  and an imaging depth of 2 to 4 mm [77]. The functional principle behind an OCT image is Michelson interferometry. The light from a low coherence light source is split via a beam splitter into two separate optical paths: the reference and the sample arm. The light backscattered from the reference and the sample arms recombine in the beam splitter and generate an interference pattern that is recorded by a detector system [78]. The signal can be mathematical expresses as:

$$I_0(k) \sim |E_r(k)|^2 + |E_s(k)|^2 + 2E_s(k)E_r(k) \cos(2k\Delta L);$$

where  $I_0$  is the intensity of the light at the detector as a function of the wavenumber  $k$ ,  $E_s$  and  $E_r$  represent the electrical fields of the sample and the reference beam, respectively, and  $\Delta L = (L_s - L_r)$ , is the optical path length difference between the sample arm  $L_s$  and the reference arm  $L_r$ . Measuring  $I_0$  as a function of either  $k$  or  $\Delta L$ , one can then determine the distance between the different layers the sample is made of, and, scanning the beam in the plane, eventually, reconstruct a 3D image.

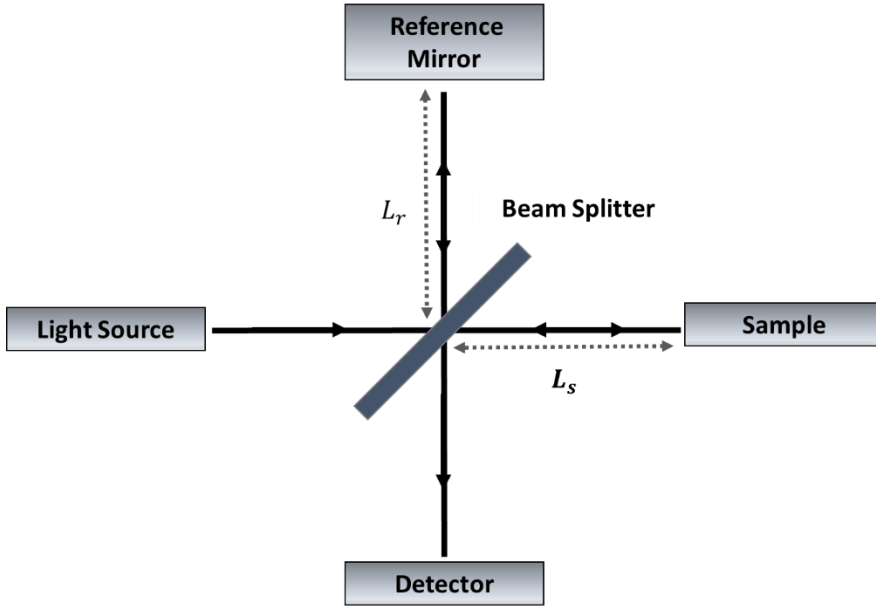


**Figure 1.2 | Schematic drawing of a Michelson interferometer.**

The light from a light source is split in two: the reference beam and the sample illumination beam. The reflected beams from both arms recombine at the beam splitter, and the interference pattern is measured at the detector as a function of the optical length difference.  $L_s$  and  $L_r$  are the corresponding optical paths of the sample and the reference arm.

The lateral and the axial resolution of OCT are decoupled from one another [79]; the axial resolution  $\Delta z$  of an OCT is defined by the coherence length of the light source axial resolution:

$$\Delta z = \frac{2 \ln 2}{n\pi} \frac{\lambda_0^2}{\Delta \lambda};$$

where  $\Delta \lambda$  and  $\lambda_0$  are the spectral width and the central wavelength of the source with a Gaussian spectral distribution, whereas  $n$  is the refractive index of the medium. The lateral resolution is a function of the optics the OCT interferometer is coupled to.

There are two leading OCT designs: Time-Domain OCT (TD-OCT) and Fourier Domain OCT (FD-OCT) [80]. The main difference between these two configurations lies in the approach used to change the optical path difference during the OCT scan. In TD-OCT, the mirror of the reference arm is mounted on a moving stage, which is used to change  $\Delta L$ . FD-OCT, on the contrary, relies on recording data as a function of  $k$ , and, therefore, offers the possibility to achieve higher acquisition speeds.

FD-OCT systems can be further branched in Sweep Source OCT (SS-OCT) and Spectral-

Domain OCT (SD-OCT). SS-OCT relies on a swept light source and a balanced detection scheme. SD-OCT uses broadband light sources at the entrance of the interferometer and then analyzes the output signal via a spectrometer. The spectrometer detects the spectral fringes in the interferometer output, which is inversely proportional to the sample depth. An A-line in the sample can be simply reconstructed by taking a Fourier transform of a calibrated and background subtracted spectrum fringe. To form a 2D image, the sample arm is translated across the sample surface with an A-scan being recorded at each position of the beam. A set of consecutive A-scans produces a cross-sectional OCT image, called B-scan, which, when combined with the other B-scans, provides the 3D final 3D image of the sample.

### 1.2.2 Common-Path OCT

In Common-Path OCT (CP-OCT), the Michelson type interferometer uses a common beam path for both the sample and the reference arm [81–84]. As reported in Figure 1.3, the light is coupled to the first arm of a circulator and exits out from the second arm, which acts as both the sample and the reference arm. The reference and the sample signals get coupled back into the third arm of the circulator to obtain an A-scan [81,82,85,86]. A CP-OCT system can be easily implemented via fiber optics, where the reference plane can be defined by a mirror positioned at the distal end of the fiber or by the fiber facet itself.

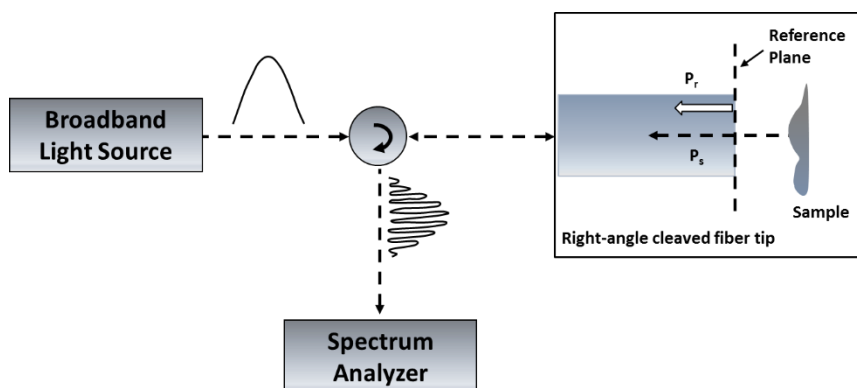


**Figure 1.3 | Schematic drawing of a Common-Path-OCT (Fourier Domain).**

The light from a broadband source is sent to the first arm of the circulator to illuminate the sample. The beams reflected by this arm are sent back to the detector.

This OCT configuration is well suited for FD-OCT imaging of biological samples. First, the reference and sample signals share the same path; thus, there is no need to adjust the reference arm. In addition, the CP-OCT approach requires no alignment and has higher

imaging stability. These features facilitate the development of fiber-optic CP-OCT probes, which can then be better integrated into microsurgical instruments or directly used for minimally invasive imaging of biological tissues.

### 1.3 Electrically assisted micro-indentation

In the previous paragraph, I empathized the crucial role of mechanical forces in cell differentiation, tissue organization, and diseases. Simultaneously, I highlighted the importance of microscopy techniques to visualize and investigate those biological processes, with a focus on OCT. There is however another aspect of biology that needs to be addressed, and it is related to how intercellular communication, muscle contraction, neural signaling, and sensory perception are carried out through the joint actions of neurons [87,88]. Living organisms are continually receiving, transmitting, and interpreting environmental inputs [89]. To this end, specialized sensory neurons use electrical impulse and environmental input to transmit information between different areas of the brain and from one cell to another one.

Electrophysiology has been the preferred means to analyze brain activity, as it can capture a wide range of neuronal phenomena, from spiking activity of single neurons to the combined activation of cell populations [90]. At the macroscale, the brain activity is often assessed via functional magnetic resonance imaging (fMRI), positron emission tomography (PET), or electroencephalography (EEG) [91]. In the last decade, fMRI has become the most dominant method to assess neuronal activity over a large brain area. However, the correlation between spiking activity and blood oxygenation level measured by fMRI is still not clear. Similarly, EEG detects spontaneous and evoked electrical activity from the scalp but with low spatial resolution. At the microscale, the function of single neurons can be investigated by means of patch-clamp or sharp microelectrode – two powerful methods that, however, are limited to the investigation of few neurons per experiment. Finally, at the mesoscale, the extracellular activity can be monitored via microelectrode arrays. This methodology allows one to monitor and stimulate the extracellular action potentials from a large population of neurons with sub-cellular resolution.

#### 1.3.1 HD-MEAs

Among the different methodologies used for electrophysiological measures in the brain, micro-electrodes arrays have become the key methodology for recording high-quality intracellular signals from single neurons to a cluster of cells or entire tissues [91–94]. Microelectrode arrays (MEA) have the unique features of bidirectionality, which enables recording and stimulation of cells (or tissues) simultaneously, and offer the mechanical and electrical long-term stability necessary for stimulation and cell recordings and large-

signal bandwidth, which allow the user to detect action potentials from multiple neurons and the different site of the same chip. These unique features make MEA systems a valuable experimental tool to collect high-density electrophysiological data from brain slices, human-derived stem cells, retinal, neuronal, cardiac, and muscular tissue. The dimension, distance, and spatial arrangement of the microelectrodes over large areas are specifically designed to allow one to collect as many details as possible without neglecting the essence of the network dynamics. The development of these types of MEAs started in 1970 and progressed in parallel with the advancement of microfabrication processes and microelectronics. Therefore, over the past years, a wide range of terminology has been used to discriminate different kind of MEA system, based on the type of transducers used (i.e., multi-transistor array, microelectrode array, multi-electrode array, 3D MEA), the type of substrate (i.e., active array or passive array) and the shape of the system (needle-type probe or neurodish) [91]. Additional discrimination between all MEAs depends on the electrode's arrangement and the sensor application. One can refer to multichannel arrays (depending on the number of channels), High-Density MEA (HD-MEA) based on the electrode density, and to *in vivo*/*in vitro* and implantable MEA related to the sensor application. In this thesis, only the planar microelectrode array for *in vitro* testing and based on Complementary Metal Oxide Semiconductor (CMOS) technology are considered.

*In vitro* CMOS MEAs have been used to record and stimulate single neurons or tissue in a wide variety of applications [95,96]. The technology is attractive because it allows one to detect several biophysical events as, for instance, an action potential (AP) that occurs once the potential of a neuron's transmembrane reaches a threshold value due to stimuli or other inputs. In neurons, action potentials play a central role in cell-to-cell communication by providing the propagation of signals along the neuron's axon. Action potentials in neurons are also known as spikes or nerve impulses. The temporal sequence of action potentials is called spike train. An HD-MEA enables direct readout and classification of spikes based on the magnitude and sign of voltage signals that exceed a threshold, and the distance from the recording site. The recorded extracellular voltage is typically in the range of tens to hundreds of microvolts; therefore, for the sake of the experiment, it is crucial to place the cell and tissue as close as possible to the electrodes. Finally, it is worth mentioning that *in vitro* HD-MEAs allows the placement of multiple electrodes at once rather than individually, offering the possibility to select different recordings sites within the same array and the ability to simultaneously receive data from multiple sites.

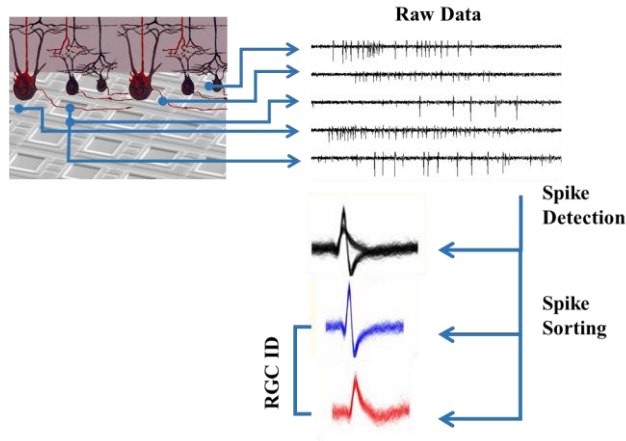


**Figure 1.4 | HD MEA spike detection in the retina.**

The cell biological sample is attached to the substrate with the embedded microelectrodes. The raw data are acquired from each of the 4096 electrodes of the chip and further analyzed to detect and sort the spike activity, adapted from [97–99].

## 1.4 Scope and relevance of the thesis

In this thesis, I present the development of two new instruments based on ferrule-top indentation, where the indentation technique is combined with OCT and with HD-MEA, respectively. By combining indentation with OCT imaging, it is possible to measure the viscoelastic properties of living tissues while simultaneously investigating tissue morphology *in situ*. This approach has been tested on *in vivo* and formaldehyde-fixed chicken embryos. The combination of HD-MEA recordings with micro-indentation offers a unique opportunity to investigate the interplay between mechanical forces and electrical signaling in neuronal tissues. This allows one to precisely monitor over a wide portion of biological tissue the functional effects that controlled mechanical stimuli induce on the electrophysiological activity of single neurons in neuronal tissue. Since mechanical stress can modulate physiological processes at the molecular and cellular levels, we expect that these tools will be a significant step forward in identifying new insights on the relationship between altered mechanosensitive signaling, stiffness, and pathologies [100].

## 1.5 Outline of the thesis

The thesis is organized as follows:

1

**Chapter 1** introduces the methods that can be used to measure the mechanical properties of biological samples and simultaneously acquire their morphological information. A brief literature overview and theoretical background of relevant areas such as tissue mechanics, optical coherence tomography, and high-density multi-electrode array are presented.

**Chapter 2** describes the possibility of combining the mechanical characterization of biological samples via microindentation with OCT imaging. To provide an efficient method for the biomechanical characterization of soft biological tissues, we introduce, in this chapter, a new tool in which the combination of non-invasive OCT imaging and depth-controlled indentation measurements allows one to map the viscoelastic properties of biological tissues and investigate correlations between local mechanical features and tissue morphology with unprecedented resolution. This approach has been tested on formaldehyde-fixed chicken embryos.

**Chapter 3** presents a study where the micro-indentation + OCT system is used to determine spatiotemporal distributions of mechanical properties of *in vivo* chicken embryos. Here we try to tackle fundamental embryological questions, namely: What is the correlation between viscoelastic properties and embryonic development from the tail towards the somites? By analyzing the storage and the loss moduli of the chicken embryo mesoderm and its surrounding tissue, we were able to better understand how the paraxial mesoderm physically develops. Furthermore, the current status and opportunities for further improvement and limitations of the setup are discussed.

**Chapter 4** is a technical chapter that explains the fabrication of new lenses fabricated on top of a single-mode fiber for CP-OCT. For most micro-imaging, endoscopy, needle-based OCT applications, CP-OCT instruments rely on an optical fiber probe that transmits light into and from the sample via graded-index (GRIN) lenses, chemically-etched axicons, or ball-shaped lenses. However, all those approaches yield probes that have an outer diameter of at least 125  $\mu\text{m}$ . The possibility to overcome the existing OCT probe miniaturization limit in a controllable way can foster the development of novel endoscopic prototypes. Therefore, we developed a new ball-lensed CP-OCT probe based on an etched optical fiber equipped with a  $\approx 65 \mu\text{m}$  diameter barium titanate microsphere, which is mounted on the inward cone left by the etching process on the cleaved end of the fiber. This approach yields probes that have a smaller outer diameter than any of the GRIN-lensed and ball-lensed CP-OCT systems reported so far in the literature. Thanks to its low cost, flexibility, and ease of use, the probe holds promise for the development of a new generation of ultrathin needle-based OCT systems.

**Chapter 5** demonstrates a new approach to simultaneously perform micro-indentation experiments and OCT imaging. A modified version of the ferrule-top sensor presented in

section 1.1.2 is used to develop a new hybrid tool based on ferrule top indentation, which is combined with optical coherence tomography in common-path mode. The sensor is therefore capable of compressing a sample with a small force and simultaneously collecting OCT depth profiles underneath and around the indentation point. This method offers the opportunity to characterize the mechanical properties of soft materials and simultaneously visualize the depth profile underneath the indentation point. The ability to integrate OCT imaging with indentation technology is promising for the non-invasive and precise characterization of different biological tissues.

**Chapter 6** describes how micro-indentation can be combined with HD-MEA systems to investigate the effects of mechanical stimulation on the electrophysiological activity of neuronal tissue at the single-cell resolution, over a wide portion of biological tissue. In particular, we studied whether retinal ganglion cells spiking activity of explanted mice retinas respond to mechanical micro-stimulations of their photoreceptor layer. In the future, the combination of HD-MEA with micro-indentation could offer a unique opportunity to investigate the effects of mechanical stimulation on the electrophysiological activity of neuronal tissue also at a single-cell resolution as well as over a wide range of biological cells and organ-tissues such as stem cells, heart, lungs, muscle, and skin.

A considerable part of the experiments described in this thesis was performed in collaboration with other research groups. The work has been financially supported by the European Research Council under the European Union's Seventh Framework Programme (FP/20072013)/ERC grant agreement no. [615170].





# Chapter 2 |

## Micro-indentation and optical coherence tomography for the mechanical characterization of embryos: Experimental setup and measurements on chicken embryos

### Abstract

The investigation of the mechanical properties of embryos is expected to provide valuable information on the phenomenology of morphogenesis. It is thus believed that, by mapping the viscoelastic features of an embryo at different stages of growth, it may be possible to shed light on the role of mechanics in embryonic development. To contribute to this field, we present a new instrument that can determine spatiotemporal distributions of mechanical properties of embryos over a wide area and with unprecedented accuracy. The method relies on combining ferrule-top micro-indentation, which provides local measurements of viscoelasticity, with Optical Coherence Tomography, which can reveal changes in tissue morphology and help the user identify the indentation point. To prove the working principle, we have collected viscoelasticity maps of fixed and live HH11-HH12 chicken embryos. Our study shows that the instrument can reveal correlations between tissue morphology and mechanical behavior.

---

Based on: M Marrese<sup>†</sup>, N Antonovaité<sup>†</sup>, B K A Nelemans, T H Smit, D Iannuzzi. "Micro-indentation and optical coherence tomography for the mechanical characterization of embryos: Experimental setup and measurements on fixed chicken embryos" Acta Biomater. 2020

<sup>†</sup> These authors contributed equally.

## 2.1 Introduction

During embryogenesis, embryos experience a sequence of morphogenetic processes that, under the influence of a complex signaling network, shape the organism and form the organs [101,102]. As the mechanical properties of biological tissues are known to influence cell behavior in terms of differentiation, migration, and body formation [103–106], one would expect that also the local viscoelastic features of a growing embryo have a strong effect on this process [102,104–109]. However, the origin and roles of the forces driving morphogenesis are still in large part unclear. Furthermore, the mechanical properties of embryos are essentially heterogeneous because of the appositional growth of the axial skeleton with tissues at the cranial end of the embryo being older and stiffer than the tissues at the caudal end. It is therefore worth asking whether, from a technical point of view, it is possible to implement novel experimental approaches that could provide new data on the mechanical properties of growing embryos and thus allow the development of more accurate morphogenetic theoretical models.

The mechanical properties of embryonic tissues have already been investigated via a wide variety of techniques, including uniaxial and compression study [110], micro-aspiration [111], macroscopic rheology [112], indentation [13–17], and imaging [118–121]. Uniaxial and compression tests, macroscopic rheology, and imaging techniques only measure bulk properties of the embryonic structure and are not suitable to assess the local mechanical response of the different morphological regions of the embryo. Micro-aspiration, which relies on the application of negative pressure on small portions of the embryonic tissue for the evaluation of its elastic modulus, does provide information about the local elastic properties of the tissue, but the technique is highly invasive.

Micro- and nano-indentation setups have in principle the capability to measure local viscoelastic properties without damaging the embryo. So far, these techniques have been mainly used for specific embryonic structures, such as the embryonic chicken heart [114,115] and brain tissue [122]. Other studies focused on the elastic characterization of cells aggregated from extracted embryonic tissue [123] or on the elastic modulus of embryonic tissue from *Xenopus laevis* [110,124–127]. For instance, in 2010, Agero et al., examined the Young's modulus of chicken embryos using a micropipette indenter attached to a micromanipulator mounted on an inverted microscope [116]. These measurements provided new insights concerning Young's modulus of the midline ( $2.4 \pm 0.1$  kPa), the area pellucida ( $2.1 \pm 0.1$  kPa) and the area opaca ( $11.9 \pm 0.8$  kPa), but lacked information about the local structures (i.e., somites, presomitic mesoderm, and tail) of the embryonic tissue. A few studies have proposed micro- and nano-indentation as a tool to measure the mechanical properties of embryos at specific developmental stages.

More recently, Chevalier and coworkers [117] used Atomic Force Microscopy (AFM) and a calibrated glass fiber cantilever indenter to assess, respectively, the local and bulk measurements of native (8-day old embryonic midgut) and fixed embryonic tissue, and

observed that the elasticity inferred from the AFM measurements was an order of magnitude lower than obtained with bulk tests. This discrepancy suggests that bulk tests describe the whole tissue as a composite material, while micro- and nano-indentations are more suitable to extract material properties at local scales. The latter may be more relevant, as the mechanical properties of the microenvironment are known to affect tissue development and change with development. While this study shows that the AFM can provide local and direct mechanical measurements of native (small) embryonic tissue, it seems that also this approach, as all the ones previously discussed, is not capable of investigating possible correlations between mechanics, morphology, and tissue structure at the micro- and mesoscopic scale.

The need to image and mechanically characterize embryonic tissue has driven scientists to use different techniques to image the sample while simultaneously measure its mechanical properties. For instance, several authors combined the imaging capabilities of OCT with elastography techniques to perform optical coherence elastography (OCE) to study the biomechanical elastic properties of embryonic tissue [128–130]. Although the spatial resolution of OCE is promising, the technique is hampered by a lack of quantitative results for the elastic modulus [131]. Furthermore, in 2015, Filas et al. combined Optical Coherence Tomography (OCT) with micro-indentation and numerical analysis to evaluate variations in chicken embryo strain. In this study, a cantilever introduces a small indentation at specific regions, while the OCT system is used to determine the deformation profile near the indentation site from the recorded motions of high-contrast markers injected into the tissue [132]. This method requires extensive sample preparation and does not provide an absolute measure of the applied force – a piece of information that is necessary for the quantification of the local viscoelastic properties.

More recently, two different groups made use of Brillouin spectroscopy to map the mechanical properties of mouse embryos [133] and the zebrafish embryo spinal cord during development and injury [134]. While this technique allows one to gather mechanical maps that resemble the sample structure, the correlations between Brillouin measurements and stiffness is still ambiguous [135,136]. It has been shown, in fact, that water content dominates Brillouin signals, thus providing a measurement of sample compressibility rather than sample stiffness. Moreover, Brillouin scattering is sensitive to gigahertz frequencies, and it does not measure the sample at biologically relevant frequencies [135].

From the discussion above, it can be concluded that, despite the numerous studies in the field, there is at present no tool to systematically analyze the local mechanical properties of embryonic tissue, more particular: an adequate instrumental technique that accurately maps the local viscoelastic response of the embryo at both the micro- and mesoscopic scales.

To solve this impasse, we developed a tool that combines a cantilever-based micro-

indentation setup with a non-invasive OCT imaging system to infer the local viscoelastic properties of embryos while simultaneously monitoring its morphological features. In this paper, we introduce this new approach, discuss its technical features, and present a series of tests that could demonstrate its potential. More specifically, to validate the potential of the approach proposed, we present depth-resolved viscoelasticity+OCT maps of HH11-HH12 chicken embryos along the mesoderm from the rostral somite to the caudal tip of the tail. To prevent tissue growth and tissue degradation during the measurements, the samples were chemically fixed. Specifically, the samples were fixed at two different fixing time in order to assess the effect of short and long fixation on the mechanical properties. To maintain tissue and cellular components in the life-like state, though, the measurements were performed in a growth medium solution at room temperature. Our data demonstrate that the instrument can indeed identify correlations between tissue morphology and tissue viscoelasticity. As a point in the case, we show that the measurements here reported can reveal the presence of three regions with distinctive viscoelastic properties: the tail, the presomitic mesoderm, and the somitic mesoderm. Finally, to demonstrate that the proposed technique is also able to perform live indentation measurements, we report one representative viscoelasticity map of the somitic region of a live embryo.

## 2.2 Materials and Methods

### 2.2.1 Chicken embryo cultures

Fertilized chicken eggs, white leghorns, *Gallus gallus domesticus* (Linnaeus, 1758), were obtained from Drost B.V. (Loosdrecht, The Netherlands), incubated at 37.5 °C in a moist atmosphere, and automatically turned every hour. After incubation for approximately 41h, HH11-HH12 chicken embryos [137] were explanted using filter paper carriers [138] cultured *ex ovo* as modified submerged filter paper sandwiches [139], immobilized in agarose and immersed in the growth medium [140].

Chicken embryos were explanted as submerged filter paper sandwiches [139] and washed in Dulbecco's PBS (Sigma, ref. D8357). On the dorsal side of the embryo, we made a rostrocaudal slit in the vitelline membrane from the heart to the tip of the tail (Figure 2.1 A) to assure a proper immobilization of the embryo on agarose later in the procedure. To facilitate accurate structural observation and sample handling, some chicken embryos were chemically fixed using 4% of formaldehyde buffered solution (Sigma, ref. 1004965000). To select the fixation methods both for observing the morphology and for determining the effect of the fixative, two fixation time points were selected: 2 and 16 hours at 4 °C. To prepare the agarose culture, 60 mm × 15 mm Petri dishes (Sigma, ref. P5481) were equipped with a glass-bottom (30 mm circular cover

glass #1, Thermo Scientific Menzel ref. CBAD00300RA140MNZ#0) to allow the OCT to image from below. A solution of 1.5% w/v low gelling temperature agarose (LGT agarose, Sigma, ref. A9414), was kept at 40°C on the bench. A hill of 500 µl 1.5% w/v agarose (Sigma, ref. A9539) was made on top of the glass bottom (Figure 2.1 D). Then, fresh LGT agarose was pipetted over the agarose hill. The embryo filter paper sandwich was dried horizontally with tissue paper and then placed on the fresh LGT agarose, dorsal side down. Carefully, the filter paper sandwich was moved horizontally, to allow the penetration of the LGT agarose through the previously made slit in the vitelline membrane and to cure towards the ectoderm of the embryo (Figure 2.1 B). Because of the hill of agarose, the embryo pointed upwards, which helped to approach the embryo with the indenter. The edges of the filter paper were covered with agarose to completely immobilize the filter paper. For live tissue, to prevent dehydration of the embryo during the LGT agarose curing, a droplet of the medium was carefully brought on top of the embryo, without touching the curing agarose. After approximately 3 minutes, the culture was placed in the indentation box (Figure 2.1 B), and the growth medium was poured slowly into the Petri dish (Figure 2.1 C). The embryo, both in formaldehyde-fixed and unfixed conditions, was then submerged in 25 ml of the growth medium to reproduce the *in vivo* environment and to minimize the adhesion forces. The growth medium consisted of medium 199 GlutaMax (Invitrogen, ref. 41150-020; 4°C), 10% chicken serum (GIBCO, ref. 16110-082; -20°C), 5% dialyzed fetal bovine serum (FBS) (GIBCO ref. 26400-036; -20°C) and 1% of a 10000 U/ml stock solution of Penicillin/Streptomycin (GIBCO ref. 15140-122; -20°C). The embryo was aligned under the OCT scan head for mechanical characterization.

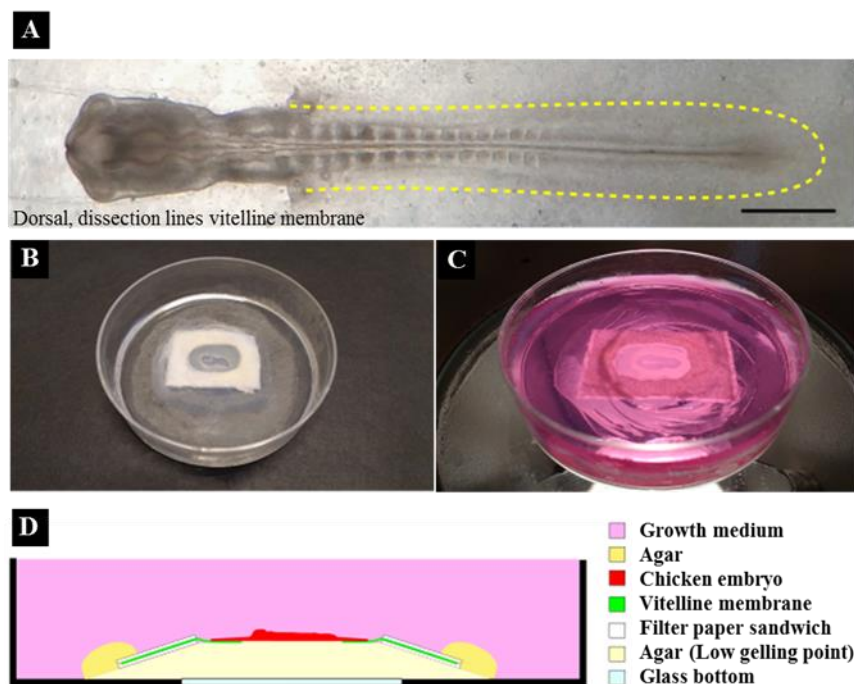


**Figure 2.1 | Agarose-immobilized culture for chicken embryos.**

(A) Dorsal view of an HH11 chicken embryo (4ohpf). The yellow line indicates the dissection sites where the vitelline membrane is opened along the embryo, to allow the immobilization of the sample in agarose. Scale bar 500  $\mu\text{m}$ . (B) The sandwich paper culture chicken embryo was immobilized in agarose by placing the embryo with its dorsal side on low gelling point agarose and covering the filter paper edges with agarose. After the agarose was cured, the embryo was covered with the growth medium. (C) Side view of embryo culture. (D) Scheme showing the agarose immobilization of the chicken embryo. The embryo was embedded in agarose on its dorsal side, while the ventral side is approachable for measurements.

## 2.2.2 Experimental setup

The setup consists of a cantilever-based indentation arm, an OCT imaging system, and a sample holder (Figure 2.2 A-B). The indentation arm comprises of an XYZ micromanipulator (PatchStar, Scientifica, UK), a piezoelectric transducer (PI p-603.5S2, Physik Instrumente), and a ferrule-top cantilever indentation probe connected to an interferometer (OP1550, Optics11, The Netherlands). A single-mode optical fiber is used to readout the bending of the cantilever, as previously described [52,141]. Cantilevers with 0.25 N/m spring constant, calibrated according to [54], and sphere radius of 55  $\mu\text{m}$  were used (Figure 2.2 C) for the experiments performed on the 2 hours fixed and the live embryos. For the 16 hours fixed samples, we used a spring constant of 0.75 N/m and a sphere radius of 70  $\mu\text{m}$ . The radius was chosen to be large enough for indenting deep into

the tissue without any slipping effects and small enough to keep a high spatial resolution between somites. The system is placed on a vibration isolation table (1VIS22-60-4, Standa, Lithuania) and enclosed in a custom-made wooden box with acoustic foam covering inside to minimize external noise. The live indentation experiments were performed at 37.7 °C, while the fixed samples were measured at room temperature.

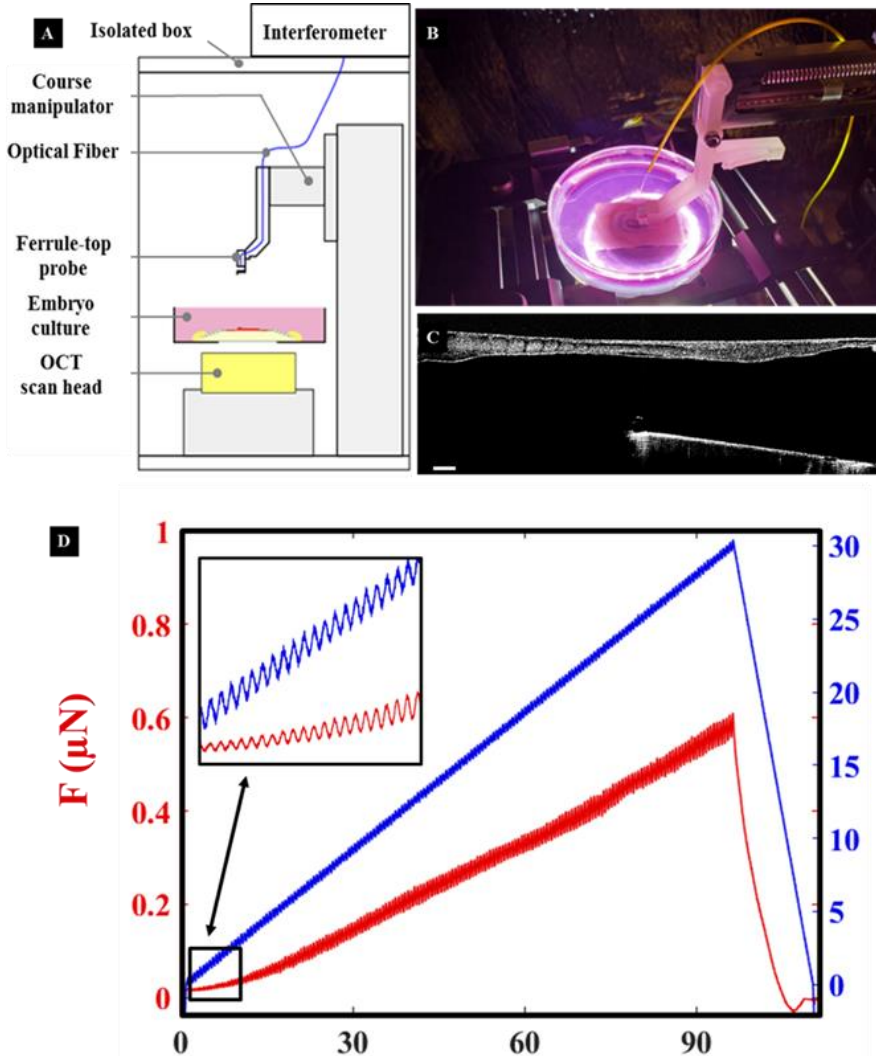


**Figure 2.2 | Ferrule-top cantilever setup with OCT for measuring viscoelastic properties of chicken embryos.**

(A) Scheme of the experimental setup. The setup was placed in a wooden box that isolates it from outside vibrations. The box was heated up to 37.7°C before the experiments were started. In the box, the embryo was visualized by OCT from below, while the mechanical measurements were performed by indentations from above. (B) Chicken embryo culture with a cantilever probe in the



box. (C) Sagittal OCT section of a cantilever with a sphere, hovering the chicken embryo ventrally. Scale bar 100  $\mu\text{m}$ . Note that the image is upside down because the OCT measures from below the sample. (D) A typical depth-controlled indentation oscillatory ramp loading profile. The left y-axis refers to the load; the right y-axis refers to the indentation depth; the x-axis represents time.

2

### 2.2.3 Indentation protocol and data analysis

Indentations were performed in a depth-controlled mode by using a feedback loop [141]. The oscillatory ramp profile (Figure 2.2 D) was selected for the characterization of viscoelastic properties at different depths, as shown by Antonovaite et al. [55]. Strain rate of the ramp was 0.01, maximum depth 25  $\mu\text{m}$ , and amplitude and frequency of oscillations were 0.25  $\mu\text{m}$  and 2.8 Hz, respectively. Load-indentation data were used to extract storage and loss moduli by fitting every 20 oscillations to a cosine function (custom-written code in Matlab). Fits with squared correlation coefficient  $R^2 < 0.5$  were removed from the data set. Storage modulus values at ~10% strain (corresponding to a depth of ~16.3  $\mu\text{m}$ ) were selected for regional comparisons, accomplishing the requirements of  $h < 10\%$  of the sample thickness but not fulfilling the small strain approximation [142]. From these raw data, the storage and loss moduli ( $E'$  and  $E''$ ) were deduced by:

$$\frac{E'(\omega)}{1-\nu^2} = \frac{F_0}{h_0} \cos \varphi \frac{\sqrt{\pi}}{2} \frac{1}{\sqrt{A}} \quad (1)$$

$$\frac{E''(\omega)}{1-\nu^2} = \frac{F_0}{h_0} \sin \varphi \frac{\sqrt{\pi}}{2} \frac{1}{\sqrt{A}} \quad (2)$$

where  $E'$  is the storage modulus,  $E''$  is the loss modulus,  $\omega$  is the frequency,  $F_0$  is the amplitude of the oscillatory-load,  $h_0$  is the amplitude of the oscillatory-indentation,  $\nu$  is Poisson's ratio of compressibility (0.5, assuming incompressibility),  $\varphi$  is the phase shift between the indentation and load oscillations,  $A = \pi a^2$  is the contact area  $a = \sqrt{Rh}$ , where  $R$  is the radius of the sphere and  $h$  – indentation depth [142]. With the oscillatory ramp, we can define the ratio between the loss and storage modulus, known as loss tangent,  $\tan(\varphi)$ , which provides the relation between the viscous and elastic components.

### 2.2.4 Optical Coherence Tomography

To find anatomical locations and follow each indentation experiment, the embryos were scanned with a spectral-domain SD-OCT (Telesto II series, Thorlabs GmbH, Germany). A super-luminescent diode (SLD, D-1300 HP, Superlum, Ireland) with full-width half maxima (FWHM) of 85 nm and central wavelength of 1310 nm was used as a light source. This OCT system can provide real-time imaging with a maximum imaging depth of 3.5 mm, the axial resolution of 5.5  $\mu\text{m}$  in air and 4.2  $\mu\text{m}$  in water, and a transverse resolution of 11.8  $\mu\text{m}$ . The setup was operated in inverted mode as the images are taken from

beneath the glass surface of the Petri dish of the agarose culture. Afterward, the collected OCT data were processed using commercial software (ThorImage OCT 4.3, Thorlabs GmbH). All the scale bars are expressed in liquid optical path length ( $n=1.33$ ) unless otherwise mentioned. For all experiments, a B-scan (transverse) image along the left-right embryo axis was acquired to evaluate the quality and the attachment of the sample. Furthermore, during indentation measurements, OCT cross-sections were captured every 10 seconds to precisely discriminate each location in the regions of interest (Figure 2.3 A - D). Combining the OCT sections and the indentation curves, each indentation was evaluated, and failed measurements were removed according to a predefined scheme.

### 2.2.5 Statistics

Normality of data distribution was tested with Shapiro-Wilk test. In case of normal distribution, statistical differences between test samples were investigated with two-way ANOVA. For non-normally distributed data, a non-parametric Kruskal-Wallis ANOVA test was used to compare data samples. All statistical analyses were performed with Statistics and Machine Learning Toolbox (version 2017a, The Mathworks, Natick, MA, USA).

## 2.3 Results

The indenter is based on ferrule-top technology [52,143], where the deflection of a micro-machined cantilever, equipped with a spherical tip, is used to determine the viscoelastic properties of the embryo via depth-controlled oscillatory ramp indentation (Figure 2.2 A-D) [141,144]. The OCT system images the embryonic structures during the indentation measurements and allows localizing the indentation point and evaluating the quality and the immobilization of the sample. Combining the OCT sections with the indentation curves, one can produce a map that represents the local mechanical properties of the sample.

Performing accurate viscoelasticity maps along the embryo is a procedure that requires time. Thus, to avoid tissue development and tissue degradation during the measurements, we used fixed HH11-HH12 chicken embryos. All embryos ( $n=4$ ) were chemically fixed for 2 or 16 hours and then immobilized on the agarose substrate (Figure 2.2) in order to determine the effect of the fixation methods. In this work, we report the result of two representative embryos with a complete indentation map.

To fully characterize the mechanical properties of the chicken embryos, we performed indentations along the mesoderm from the rostral somites to the caudal tip of the tail (Figure 2.3 A-D). We also indented transversely so that five regions of interest were measured: lateral mesoderm (LM: regions 1 and 5), paraxial mesoderm (PM: regions 2

and 4) and midline (MD: region 3). For further details regarding the investigated areas, we refer the reader to Table 1.

2

Locations	Somitic Mesoderm		Presomitic Mesoderm (PSM)		Tail	
1	Left Lateral Mesoderm	S-LLM	Left Lateral Mesoderm	P-LLM	Left Lateral Mesoderm	/
2	Left Paraxial Mesoderm	S-LPM	Left Paraxial Mesoderm	P-LPM	Left Paraxial Mesoderm	T-LPM
3	Midline	S-MD	Midline	P-MD	Midline	T-MD
4	Right Paraxial Mesoderm	S-RPM	Right Paraxial Mesoderm	P-RPM	Right Paraxial Mesoderm	T-RPM
5	Right Lateral Mesoderm	S-RLM	Right Lateral Mesoderm	P-RLM	Right Lateral Mesoderm	/

**Table 1. | Anatomical regions that were indented.**

Each embryo was indented transversely so that five regions of interest were measured: left and right lateral mesoderm (LLM and RLM for regions 1 and 5), paraxial mesoderm (LPM and RPM: regions 2 and 4) and midline (MD: region 3).

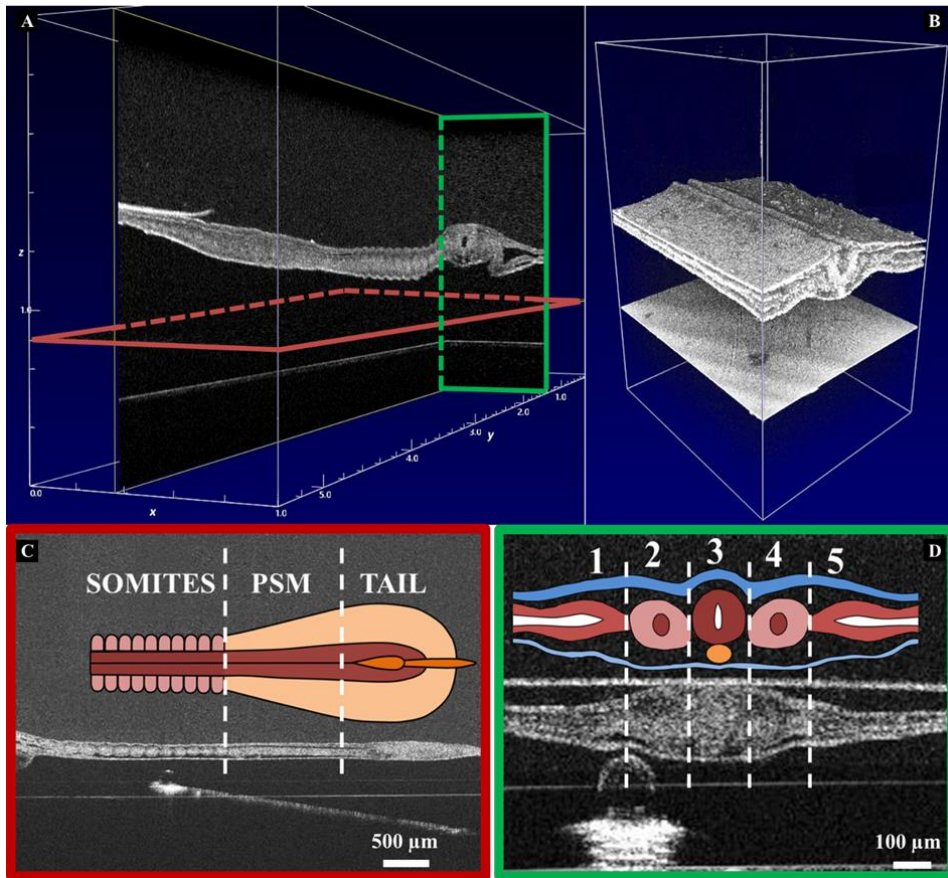


**Figure 2.3 | Morphological features of one of the embryos.**

(A) Sagittal (red) and transverse (green) OCT cross-section and (B) volumetric OCT image showing the three germ layers. (C-D) Sagittal and Transverse OCT image of one of the embryos during indentation tests. Note that all the images are upside down because the OCT measures from below the sample.

Figure 2.4 C and D show high resolution ( $25 \mu\text{m} \times 50 \mu\text{m}$  step size) viscoelasticity maps ( $E'$  = storage modulus;  $E''$  = loss modulus, at 10% strain and 2.8 Hz frequency, with a sphere radius of  $55 \mu\text{m}$ ) of the somitic region of one embryo fixed for 2 hours. The plots seem to confirm that the local mechanical properties of the sample are correlated with somite morphology. From the viscoelasticity maps, one can also distinguish the separation between individual somites – a result that confirms that the indentation method is able to sense structures underneath the endoderm. The scatter plot in Figure 2.4 E shows the distribution of storage modulus ( $E'$ ) averaged over nine somites (S-XI to S-III) for 5 regions of interest: left and right lateral mesoderm, left and right paraxial mesoderm, and midline. This set of data shows that the somites (left and right) are softer

than the midline but stiffer than the lateral mesoderm.

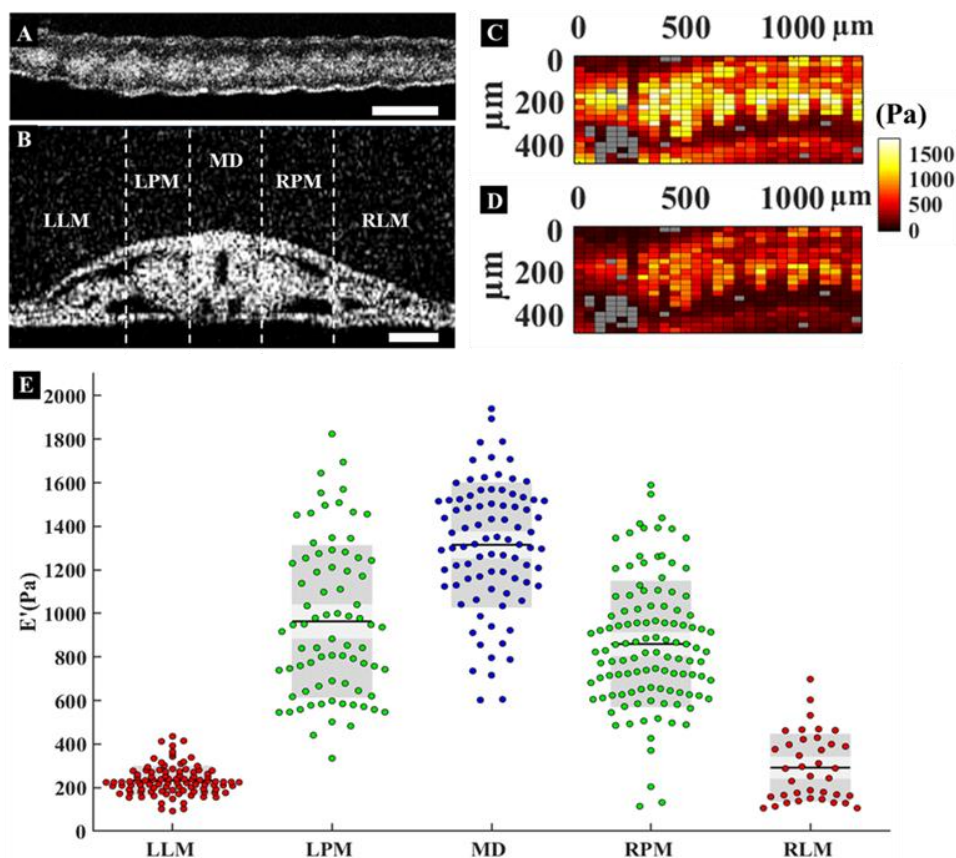


**Figure 2.4 | High-resolution viscoelasticity map.**

(A) Sagittal OCT section along the somitic region of the embryo. Scale bar = 100  $\mu\text{m}$  (B) Transverse OCT image across of the embryo used in this experiment, along with the morphological anatomical regions. Scale bar = 100  $\mu\text{m}$ . (C-D) High resolution ( $25 \times 50 \mu\text{m}$ ) colored map of storage  $E'$  (C) and loss modulus  $E''$  (D) at 10% strain and 2.8 Hz frequency over the embryo somitic mesoderm. (E) Storage ( $E'$ ) modulus across the embryos. Abbreviations of the region of interest from left to right: (LLM) left lateral mesoderm, (LPM) left paraxial mesoderm, (MD) midline, (RPM) right paraxial mesoderm, (RLM) right lateral mesoderm.

The viscoelasticity map of another embryo (sample fixation time of 16 hours) is shown in Figure 2.5 A ( $E'$ ) and 5B ( $E''$ ) at 10% strain and frequency of 2.8 Hz covering an area of  $800 \mu\text{m} \times 4000 \mu\text{m}$ , from somite VII till the caudal tip of the tail, with a spatial resolution of  $50 \mu\text{m} \times 50 \mu\text{m}$  and measured with a sphere radius of  $70 \mu\text{m}$ . Because of the lower resolution and larger indentation sphere used in this second experiment (with respect to the previous one), the mechanical contrast between individual somites is less evident. Yet, this set of data, along with the scatter plot of the storage ( $E'$ ) and loss ( $E''$ ) moduli of the

tested sample reported in Figure 2.6, still provides valuable information. The mechanical maps together with the scatter plots, in fact, clearly display the morphological heterogeneity of the three main anatomical regions from young to old: tail, presomitic mesoderm, and somitic mesoderm. First, the midline is the stiffest structure of the embryonic body, and its stiffness decreases from the somites down to the caudal tip of the tail. The somites are the stiffest material in the paraxial mesoderm, although their difference with the midline does not change significantly while indenting from the somitic region up to the tail. Dynamic indentation reveals that a substantial viscous component is present in the tissue, as also clear from Figures 2.5 B and 2.6 B.

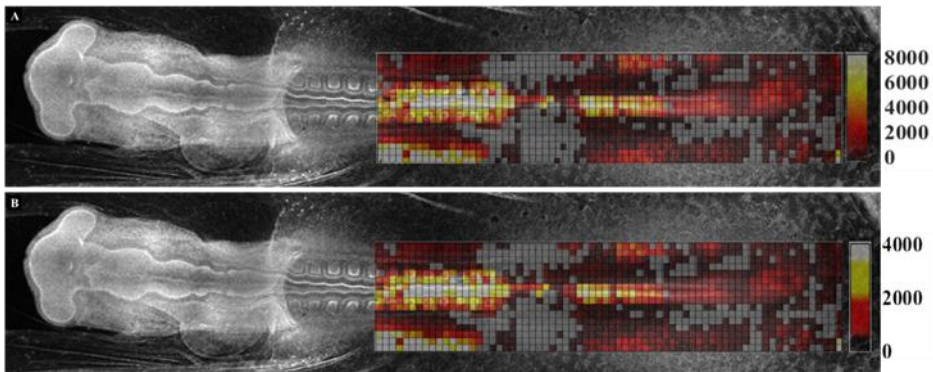


**Figure 2.5 | Viscoelasticity maps of one of the chemically fixed embryos for 16 hours.** Colored map of storage  $E'$  (A) and loss modulus  $E''$  (B) in Pa at 10% strain and 2.8 Hz frequency.

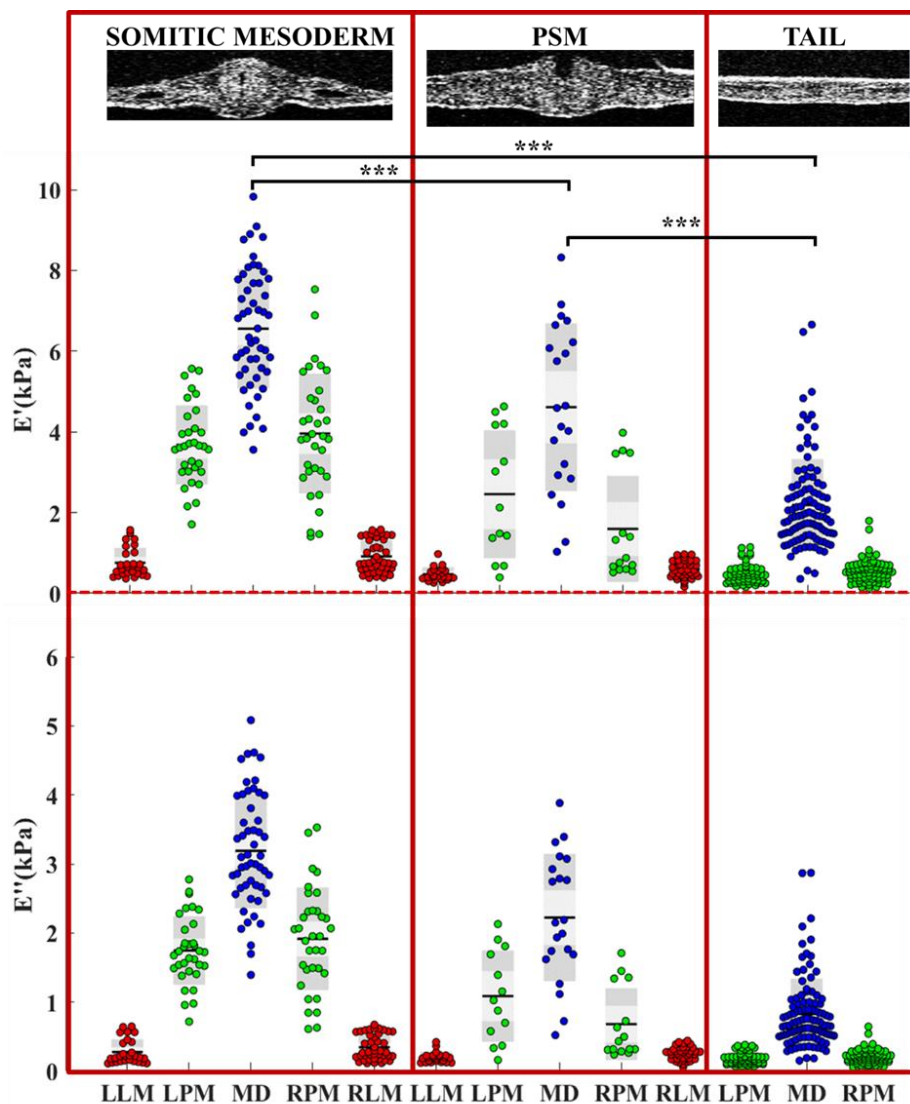


**Figure 2.6 | Storage ( $E'$ ) and loss ( $E''$ ) moduli at 10% strain and 2.8 Hz frequency along the embryos for 16 hours of fixation.**

Transverse OCT sections show the three distinct anatomical regions: Somitic Mesoderm, Presomitic Mesoderm (PSM) and Tail. For each region five locations of interest are measured: (LLM) left lateral mesoderm, (LPM) left paraxial mesoderm, (MD) midline, (RPM) right paraxial mesoderm, (RLM) right lateral mesoderm.

Furthermore, elastic and viscous components change following the same trend. Specifically,  $\tan(\varphi)$  (see Figure 2.7 A), which is the ratio between loss and storage modulus, is higher for the paraxial mesoderm and midline and lower for lateral mesoderm in the somitic and presomitic area. This behavior indicates that stiffer and

larger structures have higher damping capability, and it can also reflect some structural aspects of the tissue. Finally, in the tail, the contribution of elasticity and viscosity is comparable for both the midline and the paraxial mesoderm. While the viscoelasticity results, presented above, were performed at fixed strain and frequency, we also observed that mechanical properties are indentation strain-dependent. Figure 2.7 B, C, and D show storage modulus as a function of the strain for the embryo reported in Figure 2.6 A. Specifically, all regions stiffen with strain, revealing the non-linear viscoelastic properties of fixed chicken embryos, a result that highlights the importance of measuring the mechanical properties of embryonic tissues in depth-controlled mode [144].

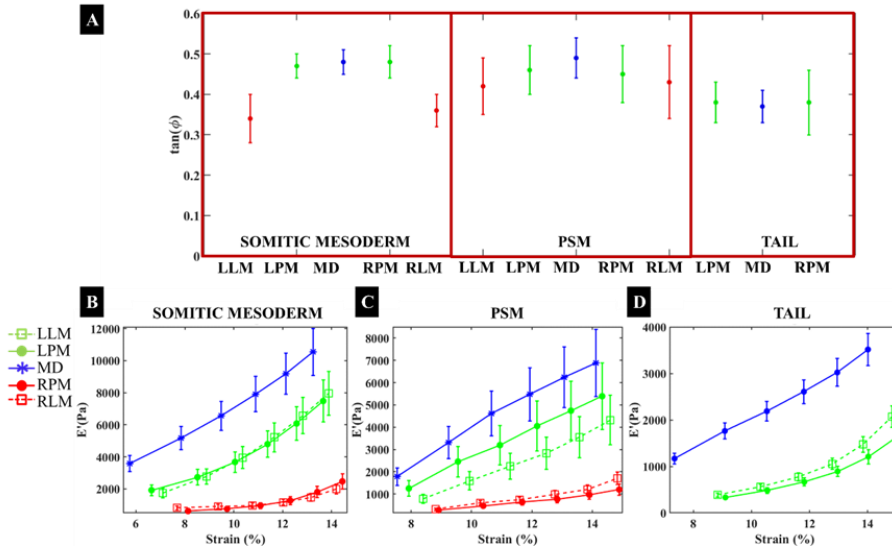


**Figure 2.7 | Non-linear and viscoelastic behavior.**

Loss tangent along the rostrocaudal embryo axis (A). Non-linear viscoelastic properties of chemically fixed embryos obtained with depth-controlled oscillatory ramp indentation.  $E'$  increases over the strain range of 6-14% for the somitic mesoderm (B), PSM (C), and Tail (D). Note that the standard deviation is positively correlated since the data are not independent.

Finally, to validate the capability of the instrument for live tissues characterization, in Figure 2.8, we report one representative high resolution ( $25 \mu\text{m} \times 50 \mu\text{m}$  step size) viscoelasticity maps ( $E'$  = storage modulus;  $E''$  = loss modulus, at 12% strain and 2.8 Hz frequency, with a sphere radius of  $55 \mu\text{m}$ ) of the live embryonic tissue. As for the formaldehyde-fixed embryo, in Figure 2.8 E the distribution of storage modulus ( $E'$ ) averaged over two somites (S-XI to S-X) for 5 regions of interest is shown. This set of data confirms that the somites (left and right) are softer than the midline but stiffer than the lateral mesoderm, even for live embryos.



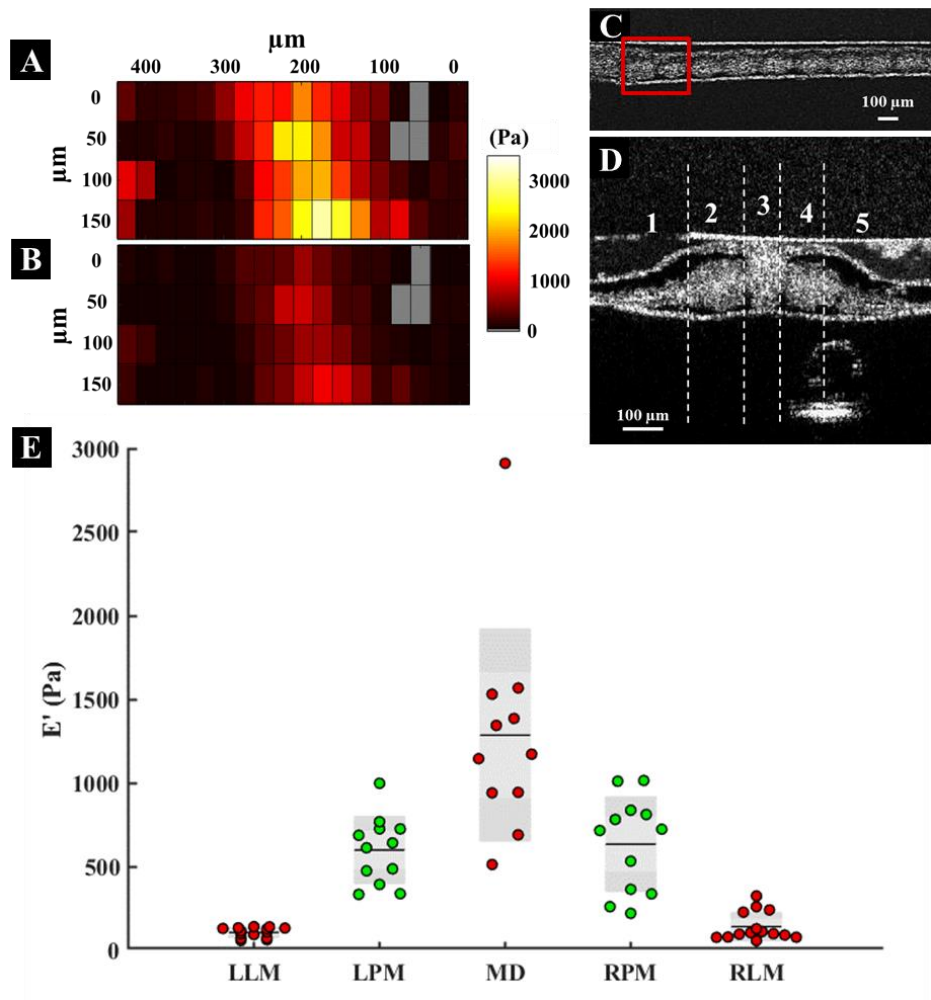


**Figure 2.8 | High-resolution viscoelasticity map of the live embryo.**

(A-B) High resolution (25 x 50  $\mu\text{m}$ ) colored map of storage  $E'$  (A) and loss modulus  $E''$  (B) at 10% strain and 2.8 Hz frequency over the somitic mesoderm. (C) Sagittal OCT section along the somitic region of the embryo used in this experiment. (D) Transverse OCT image across the embryo along with the morphological, anatomical regions. (E) Storage ( $E'$ ) modulus across the embryos. Abbreviations of the region of interest from left to right: (LLM) left lateral mesoderm, (LPM) left paraxial mesoderm, (MD) midline, (RPM) right paraxial mesoderm, (RLM) right lateral mesoderm.

A)	S-RLM	P-LLM	P-RLM
S-LLM	n.s.	***	n.s.
S-RLM		***	***
P-LLM			*

B)	S-RPM	P-LPM	P-RPM
S-LPM	n.s.	**	***
S-RPM		**	***
P-LPM			n.s.

C)	P-MD	T-MD
S-MD	***	***
P-MD		***

**Table 2. Statistical analysis.**

Statistical comparison of A) lateral mesoderm, B) paraxial mesoderm, and C) midline. Yellow color highlights regions with the same structure on opposite sides of the embryo and green highlights regions with different structures, adjacent to each other.

## 2.4 Discussion and conclusion

To understand the role of mechanical cues in embryogenesis, detailed knowledge of the morphological features of the chicken embryo is crucial. In this context, the use of real-time OCT imaging allows for distinguishing the individual embryonic structures such as somites, notochord, and neural tube. One of the main advantages of using the OCT in combination with indentation experiments is related to the possibility to have real-time information in depth, which is essential for the estimation of the sample thickness and proper alignment of the probe onto the tissue. In this regard, the OCT allows us to monitor if the probe is approaching perpendicularly to each of the measured embryonic structures in order to avoid local shear or slipping of the probe along with the tissue. Moreover, one of the critical issues in indentation measurements is to hold the sample during the experiments properly. In this regard, the OCT enables us to accurately visualize the immobilization of the sample on the agar and to avoid measuring the floating tissue rather than the tissue stiffness. The structural heterogeneity, distinctly visible in the OCT cross-section images (Figure 2.3 A-D) results in different regional stiffness (Figure 2.4). Thus, it is interesting to note that some of the mechanical features observed correlate well with the anatomical structure of the chicken embryo, even though the samples were fixed. For example, the midline, the stiffest structure of the embryonic tissues, contains an embryonic cellular rod, the notochord, that gives structural support to the adjacent tissues, thus representing the major skeleton element in the embryonic vertebrae [145]. The somites, the precursors of the vertebrae, cartilage, tendons, and dermis, is softer than the midline but stiffer than the lateral mesoderm,

which mostly forms the circulatory system, body cavity, and pelvis in the adult body [146]. Assuming that the mechanical contrasts between different regions of an embryo are preserved, to a certain extent even after fixation, we may assert that some of the spatial variations in stiffness are related to the physiological roles of each anatomical structure. Continuing on this line of reasoning, then, from the analysis of the indentation maps in Figure 2.5 along with OCT images, one could further speculate that the gradient of stiffness observed along the mesoderm from the rostral somites to the caudal tip of the tail (see Figure 2.5) may be correlated with the maturation of the PSM. The somites are formed in pairs of epithelial spheres beside the neural tube and epithelialize, and this stiffens several hours after separation from the PSM. The PSM itself does not yet have somites and essentially consists of granular mesenchymal cells; however, these also increase in density from caudal to rostral. The stiffness along the body axis could also reflect the maturation of each structure; in fact, at this stage, the cranial end of the embryo is older and stiffer than the caudal end. If this behavior is confirmed *in vivo*, one could argue that the biomechanical processes during somite formation, such as changes in extracellular matrix composition, migration, and contraction of mesodermal cells, could be triggered by this gradient of stiffness along the rostrocaudal axis of the embryo. Reversely, one could say that the mechanical stiffening reflects the maturation of the tissue as cells become contractile and produce extracellular matrix.

By performing depth-controlled frequency-domain indentation tests on embryonic tissues, we have evaluated the viscoelastic nature of the embryonic tissue, as previously observed in the time domain with stress relaxation, creep test, and with non-linear finite element modeling for the heart tube in other experiments [147,148]. Our viscoelasticity maps reveal that the viscous component is not negligible for all the indented regions, thus indicating that it is necessary to mechanically characterize the embryonic tissue by considering both the elastic and viscous contribution.

In addition, we have demonstrated that our technique can also reveal the presence of non-linear mechanical behavior of tissues. Both storage and loss modulus increase with indentation strain, thus proving that fixed chicken embryos are a non-linear material. This highlights that the mechanical properties of chicken embryos strongly depend on the indentation strain at which each measurement is performed. Our findings, reported in Figure 2.8, demonstrate that similar behavior is observed in live embryos, suggesting that, to obtain reliable measurements of the mechanical properties of embryos, it is crucial to rely on a depth-controlled indentation mode.

In this context, one of the main challenges of performing high-resolution viscoelasticity map in living tissue is related to the necessity to keep the tissue stable over the course of the measurements. The maps reported in Figure 2.4 and Figure 2.5 were performed in 18 and 44 hours, respectively. These long time scales do not allow us to map the entire live embryo, considering that the time necessary for one somite to form is 90 minutes and that after 4 hours the apoptosis rate of the embryonic tissue increases significantly.

Hence, while performing the viscoelasticity map *in vivo*, the embryo continues to grow, and the age interval between rostral and caudal structures becomes larger, yielding to an unfair comparison between the rostral somites region and the caudal tip of the same embryo. However, from the live measurements performed in the somitic region and in agreement with other investigators [117,149], we found that the same general contrast of stiffness between the midline, the somites, and the lateral mesoderm is preserved after fixation (see Figure 2.8). Thus, it is interesting to note that some of the mechanical features observed for the formaldehyde-fixed samples are consistent with the live experiments.

The integration of OCT imaging with indentation techniques could be further exploited by introducing mathematical models that provide a more extensive evaluation of different deformation profiles in relation to the local material composition. In this study, we assume that the sample is isotropic, homogeneous, flat, non-adhesive and that the time-dependent properties are due only to the viscoelasticity, by neglecting the poroelasticity. Clearly, the developing embryo is none of this. In this perspective, the combination of OCT imaging with indentation tests could potentially be used to model the mechanical properties of heterogeneous tissue by monitoring the deformation of individual structures, as in Optical Coherence Elastography [150].

Moreover, we would like to stress once more that the goal of this paper is to present a new instrument for the characterization of the mechanical properties of embryos. For simplicity, we deliberately decided to perform most of the measurements on fixed embryos, even though fixation agents can cause cross-links between molecules that, eventually, alter the mechanical properties of the sample surface [151,152]. Yet, our findings suggest that different fixation times result in qualitatively similar morphological and mechanical behavior. For instance, a similar range of stiffness is found between the live embryo and the embryo fixated for 2 h while, from a quantitative perspective, it is fair to stress that, going from 2 hours fixation time, as in Figure 2.4, to 16 hours fixation time, as in Figure 2.5, one observes a four-time increase in material stiffness, in agreement with what observed by others [153–155]. Nevertheless, even if the mechanical response is strongly affected by the treatment on an absolute scale (absolute stiffness values), it seems that the fixed embryo does resemble mechanical behaviors that would fit well within a description of the mechanical properties of a live sample. One could also argue that the presence of the endoderm influences our measurements. It is important to stress that all indentations were not directly performed on the mesoderm but masked by the endoderm since the removal of this thin (7  $\mu\text{m}$ ) layer would have been too invasive. We assumed that the presence of the thin endoderm does not significantly affect the mechanical findings and would have the same effect on the whole embryonic structure.

In conclusion, we have introduced a new tool that can accurately capture variations in stiffness due to different sample structures or treatments, to reliably measure the

viscoelastic and non-linear properties of heterogeneous materials and, simultaneously investigate sample morphology. By reducing the experimentation time, for instance by focusing on specific regions of the embryonic tissue, we have confidence that our approach could well serve as a promising tool for quantitative and exhaustive studies of the live chicken embryos. Moreover, the combination of OCT images and indentation tests could also be used to thoroughly investigate the evolution of tissue mechanical properties during morphogenesis and development *in vivo* and to determine quantitatively mechanical changes in normal and pathological conditions, filling the existing gaps in the field of developmental biology.





## Chapter 3

# In vivo characterization of chick embryo mesoderm by optical coherence tomography assisted microindentation

3

### Abstract

Understanding the mechanical properties of embryos is a crucial prerequisite for the investigation of morphogenesis. In Chapter 2 we presented a new instrument that, via the combination of micro-indentation with Optical Coherence Tomography (OCT), allows us to investigate the mechanical properties of both fixed and live embryos. However, embryos are growing organisms with highly heterogeneous properties in space and time. Therefore, in order to provide the spatial distribution of mechanical properties of chick embryos and the structural changes in real-time, we report here the stiffness measurements on live chicken embryos, from the mesenchymal tailbud to the epithelialized somites. The storage modulus of the mesoderm increases from  $(180 \pm 18)$  Pa in the tail up to  $(720 \pm 120)$  Pa in the somitic region (mean  $\pm$  SEM,  $n=12$ ). The midline has a mean storage modulus of  $(950 \pm 110)$  Pa in the caudal (PSM) presomitic mesoderm (mean  $\pm$  SEM,  $n=12$ ), indicating a stiff rod along the body axis, which thereby mechanically supports the surrounding tissue. The difference in stiffness between midline and presomitic mesoderm decreases as the mesoderm forms somites. This study provides an efficient method for the biomechanical characterization of soft biological tissues in vivo and shows that the mechanical properties strongly relate to different morphological features of the investigated regions.

---

Based on: M Marrese, N Antonovaité, B K A Nelemans, A Ahmadzada, D Iannuzzi, T H Smit. In vivo characterization of chick embryo mesoderm by optical coherence tomography assisted microindentation. The FASEB Journal. July 2020



### 3.1 Introduction

Morphogenesis is a continuous process of cell migration, tissue deformation, and growth. It is a self-organized patterning process orchestrated by the properties of the cells, which are controlled by gene expressions and chemical and physical signaling. While biochemical signals are known to play a fundamental role in the control of tissue morphogenesis [156–159], several *in vitro* and *in vivo* studies [117,132,160,161] have shown the relevance of mechanical cues in the control of cell behavior that is central for the developmental processes. Unraveling the functional role of mechanical forces in morphogenesis is, therefore, a crucial research topic for developmental biologists. Specifically, the processes during somite formation along the rostrocaudal axis of the embryo, such as the changing of extracellular matrix (ECM) composition, the differential migration, and the active cell contraction of epithelial cells of the mesoderm, suggest that there should be differences in mechanical properties along the rostrocaudal axis of the embryo. Mechanical forces and constraints play an important role in embryonic development as they are able to affect the migration and differentiation of single cells [162,163]. Also, tissues and organs are influenced by mechanical forces in their cellular organization and functionalities, as shown in tooth [164,165] and limb development [166,167]. However, the lack of methodologies enabling precise and quantitative measurements of mechanical properties of live tissues has hindered an exhaustive understanding of the role of mechanics in embryonic development. In chapter 2, we proposed an experimental platform that combines micro-indentation and optical coherence tomography to assess mechanical properties in paraformaldehyde-fixed embryos. There, we have demonstrated a relationship between local mechanical properties and tissue morphology for three main embryonic regions of interest: the tail, the presomitic mesoderm, and the somitic mesoderm. While in our previous study, we reported a stiffness map of fixed embryos [53], we now investigate the viscoelastic properties of live chicken embryo mesoderm during somite formation. To that end, HH9-HH11 chicken embryos were cultured in filter paper sandwiches, immobilized in agarose, and indented from the ventral side along the embryo with the ferrule-top indenter, while the structure was locally imaged via optical coherence tomography (OCT). The simultaneous use of these two technologies allows one to perform systematic studies on two interconnected topics: on the one hand, the mechanical properties of the embryos that can be characterized through tissue microindentation; on the other hand, and the change in shape that occurs during morphogenesis. Therefore, we present a local mechanical characterization of live embryos that extends our previous work [53] by highlighting the mechanical heterogeneity and the strong viscoelastic nature of the embryonic tissue *in vivo*. We further demonstrate that, while there are substantial differences in absolute viscoelastic responses between individual embryos, the relative trends among anatomical regions are similar and reasonably related to the maturation of the presomitic mesoderm and midline in the trunk and tail. This study opens new

avenues to explore how mechanics can contribute to shaping embryonic tissues and how it affects cell behavior within developing embryos.

## 3.2 Material and Methods

### 3.2.1 Chicken embryo cultures

The embryo cultures were prepared as described somewhere else [53]. Briefly, fertilized chicken eggs, white leghorns, *Gallus gallus domesticus* [168], were obtained from Drost B.V. (Loosdrecht, The Netherlands), incubated at 37.5 °C in a moist atmosphere, and automatically turned every hour. After incubation for approximately 41h, HH9-HH11 chicken embryos (15) were explanted using filter paper carriers [138] cultured *ex ovo* as modified submerged filter paper sandwiches [170], immobilized in agarose in a 35 mm petri dish, and immersed in the growth medium[171].

To avoid disturbance of the measurements by the beating of the heart that might develop, the heart tube of the ventral side of sandwiched embryos was removed (Figure 3.1 A and B). This does not appear to inhibit further development of the spinal structures in the chick embryo. To prevent dehydration of the live embryo during the LGT agarose curing, a droplet of the medium was carefully brought on top of the embryo, without touching the curing agarose. After approximately 3 minutes, the culture was placed in the indentation box, submerged in 25 ml of the growth medium and anatomically aligned under the OCT to precisely discriminate each indentation location.

The growth medium consisted of medium 199 GlutaMax (Invitrogen, ref. 41150-020), 10% chicken serum (GIBCO, ref. 16110-082), 5% dialyzed fetal bovine serum (FBS) (GIBCO ref. 26400-036) and 1% of a 10000 U/ml stock solution of Penicillin/Streptomycin (GIBCO ref. 15140-122).

### 3.2.2 Experimental setup

The setup consists of a cantilever-based indentation arm, an OCT imaging system, and a sample holder mounted on an anti-vibration table and covered with a custom acoustic isolation box to minimize mechanical noise. The setup was further equipped with a temperature control system to maintain 37 °C, which was monitored at ~2 cm distance from the petri dish with the embryo (Figure 3.1). The indenter is based on a micro-machined cantilever, operating as a force transducer. An extensive description and validation of the experimental setup have been reported in our previous publication[53]. The ferrule top indentation probes used in this work are fabricated in our lab, according to [49,52] and calibrated, according to [54]. Further details about the ferrule-top indenter are provided in supplementary figure 3.5.1. Briefly, for indentation measurements on live

embryos, cantilevers with spring constant in the range of 0.34-1.2 N/m, and spheres radius between 54 and 69  $\mu\text{m}$  were used. Indentations were performed in a depth-controlled mode by using an oscillatory ramp profile at indentation speed of  $\sim 0.5 \mu\text{m/s}$ , maximum indentation depth of 30  $\mu\text{m}$ , and amplitude and frequency of oscillations were 0.25  $\mu\text{m}$  and 2.5 Hz, respectively. Load-indentation data were used to extract storage and loss moduli [50,54,55], where storage modulus corresponds to the elastic component, and loss modulus corresponds to the viscous component of mechanical response.

By contrast, viscosity describes the resistance of the material to flow and generally describes the thickness or the internal friction of a moving fluid. The ratio between loss and storage modulus is a tangent of the phase delay,  $\tan(\varphi)$ , between oscillations in indentation and load.  $\tan(\varphi)$  is also called damping factor, as it describes how much energy is lost during deformation. For our experiment, storage modulus values at an averaged strain of  $8 \pm 1\%$  (corresponding to an indentation depth  $h \sim 10\text{-}12 \mu\text{m}$ ) were selected for regional comparisons, accomplishing the requirements of  $h < 10\%$  of the sample thickness and small strain approximation[172].

To find anatomical locations and follow each indentation experiment, the embryos were scanned with a spectral-domain SD-OCT (Telesto II series, Thorlabs GmbH, Germany) in inverted mode, as reported elsewhere[53].

To perform a full mechanical characterization of the embryonic tissues, we focus on eight positions along the rostrocaudal axis of the mesoderm that show anatomical differences (Figure 3.2 and 3.3). These eight locations were indented by transverse lines of 10 indentations, with a step size of 50  $\mu\text{m}$  (Figure 3.2 and Table 3.1). The indentation lines (500  $\mu\text{m}$  length) were centered to the embryo midline so that on every rostrocaudal position, five regions of interest were measured: lateral mesoderm (regions 1 and 5), paraxial mesoderm (regions 2 and 4) and the midline (region 3) (Figure 3.3 and Table 3.2). A total of 20 embryos were explanted and examined, of which 12 embryos were used for the experiments. Other embryos were either damaged or detached during the measurements. All stiffness values are reported as mean  $\pm$  SEM.

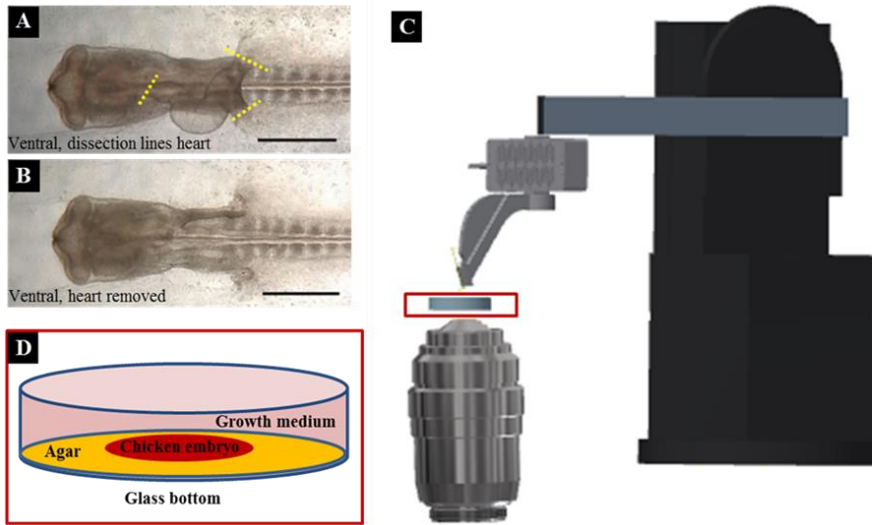


**Figure 3.1 | Schematic view of the setup and the sample preparation.**

(A) Ventral view of an HH11 chicken embryo (40hpf). Yellow lines show the dissection sites to remove the embryonic heart tube, to prevent the beating heart from disturbing the measurements. (B) The same embryo as in (A), after dissection of its heart tube. Scale bar in A and B is 500  $\mu\text{m}$ . (C) A ferrule-top probe is equipped with an optical fiber for interferometric readout of the cantilever and with a spherical tip to indent the sample. The probe is mounted on the Z-piezoelectric actuator, which is solidly attached to an XYZ manipulator. The OCT is employed in inverted mode. (D) The embryo is embedded in agarose on its dorsal side, while the ventral side is approachable for measurements and immersed in the growth medium.

To find anatomical locations and follow each indentation experiment, the embryos were scanned with a spectral-domain SD-OCT (Telesto II series, Thorlabs GmbH, Germany) in inverted mode, as reported elsewhere (15).

To perform a full mechanical characterization of the embryonic tissues, we focus on eight positions along the rostrocaudal axis of the mesoderm that show anatomical differences (Figure 3.2 and 3.3). These eight locations were indented by transverse lines of 10 indentations, with a step size of 50  $\mu\text{m}$  (Figure 3.2). The indentation lines (500  $\mu\text{m}$  length) were centered to the embryo midline so that on every rostrocaudal position, five regions of interest were measured: lateral mesoderm (regions 1 and 5), paraxial mesoderm (regions 2 and 4) and the midline (region 3) (Figure 3.3). A total of 20 embryos were explanted and examined, of which 12 embryos were used for the experiments. Other embryos were either damaged or detached during the measurements. All stiffness values are reported as mean  $\pm$  SEM.

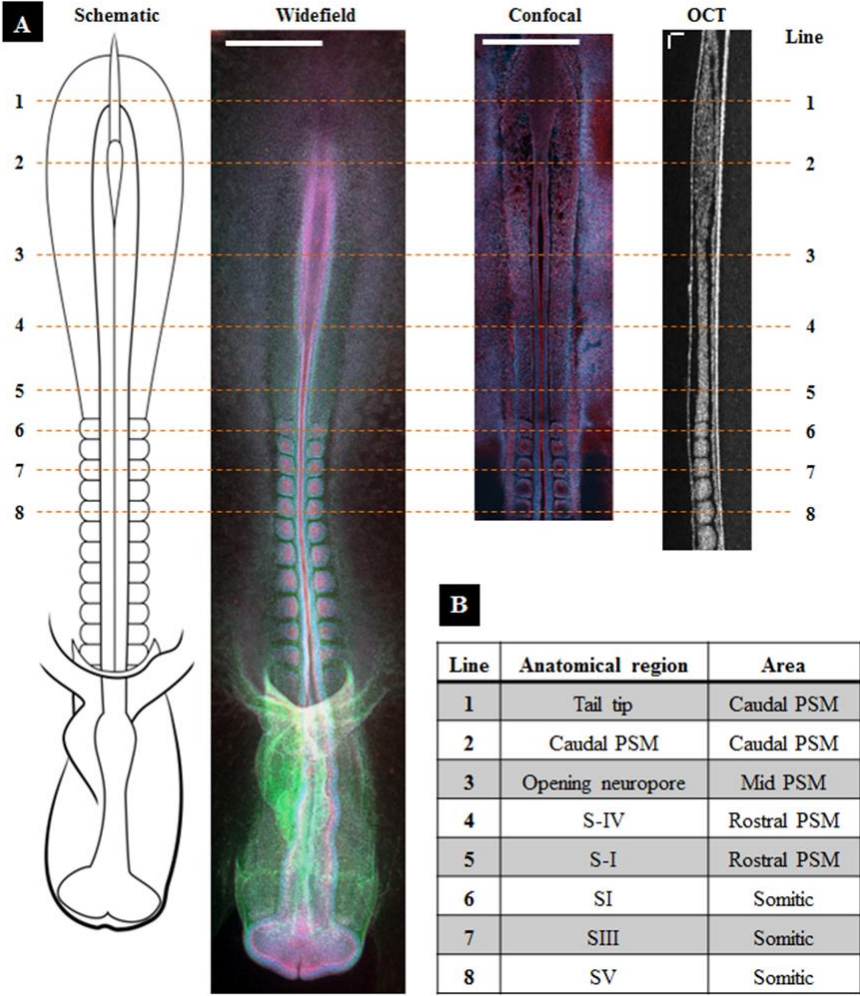
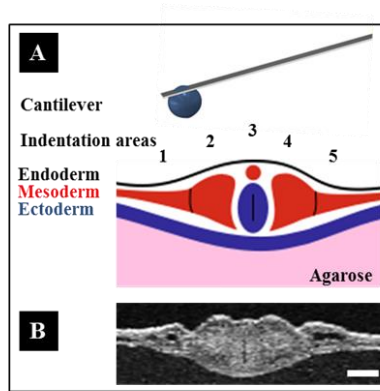


**Figure 3.2 | Sagittal embryo indentation points.**

(A) Embryos were indented with eight transverse lines, at 10 positions with 50  $\mu\text{m}$  steps, across the rostrocaudal axis while visualized by OCT. The lines are shown imposed on a schematic embryo and a widefield immunograph. Next, there are a frontal confocal section (ventral side of the embryo) and the OCT cross-section scan (sagittal - side view) through the mesoderm. Rostral is down, and caudal is up. Immunostainings are red (actin), green (fibronectin), blue (nuclei). The scale bars are 500  $\mu\text{m}$  for the widefield and confocal image and 100  $\mu\text{m}$  for the OCT. The schematic view of the embryo is not to scale. (B) Anatomical regions that were indented, from caudal to rostral.



C	Position	Somatic Mesoderm		Presomitic Mesoderm (PSM)		Tail	
	1	Left Lateral Mesoderm	S-LLM	Left Lateral Mesoderm	P-LLM	Left Lateral Mesoderm	/
	2	Left Paraxial Mesoderm	S-LPM	Left Paraxial Mesoderm	P-LPM	Left Paraxial Mesoderm	T-LPM
	3	Midline	S-MD	Midline	P-MD	Midline	T-MD
	4	Right Paraxial Mesoderm	S-RPM	Right Paraxial Mesoderm	P-RPM	Right Paraxial Mesoderm	T-RPM
	5	Right Lateral Mesoderm	S-RLM	Right Lateral Mesoderm	P-RLM	Right Lateral Mesoderm	/

**Figure 3.3 | Transversal embryo indentation points.**

(A) Schematic view and (B) OCT cross-section of the indentation positions of an HH11 embryo embedded in agarose. The scale bar is 100  $\mu\text{m}$ . (C) Anatomical regions that were indented across the embryo. Abbreviations of the region of interest from left to right: (LLM) left lateral mesoderm, (LPM) left paraxial mesoderm, (MD) midline, (RPM) right paraxial mesoderm, (RLM) right lateral mesoderm.

### 3.3 Results and Discussion

The indenter is based on ferrule-top technology [52,143], where a micro-machined cantilever, operating as a force transducer and equipped with a spherical tip, is used to determine the viscoelastic properties of the embryo via depth-controlled oscillatory ramp indentation profile [53,144]. The OCT system images the embryonic structures during the indentation measurements and allows localization of the indentation points and evaluation of the quality and the immobilization of the sample. The details of the experimental setup (Figure 3.1) and sample preparation are briefly reviewed in the

Method section and fully reported elsewhere [53].

Performing a full indentation map at 50  $\mu\text{m}$  resolution along the embryo with the proposed depth-controlled oscillatory profile is time-consuming. A single indentation takes  $\sim 60$  s while a new somite is formed every 80 minutes; thus, it is not feasible to map the entire embryo at the same developmental stage *in vivo*. Therefore, to preserve the spatial accuracy along the embryo, we limited indentations to eight lines along the rostrocaudal axis of the mesoderm that are anatomically different. For further details regarding the investigated areas, we refer the reader to Figure 2 and 3.

Figure 3.4 shows the averaged storage modulus ( $E'$ ) and loss modulus ( $E''$ ) of 12 *in vivo* HH9-HH11 chicken embryos obtained for eight positions along the rostrocaudal axis of the mesoderm. The measurements were done at an averaged strain of  $\sim 8\%$  and 2.5 Hz oscillation frequency. For each of the eight positions along the embryo, the plot shows the distribution of  $E'$  and  $E''$  for five regions of interest: left and right lateral mesoderm, left and right paraxial mesoderm, and midline. From the data in Figure 4, along with OCT images, one can observe that regions with different morphology have distinct mechanical properties. The stiffness difference between the paraxial mesoderm and the midline is more significant in the PSM and the tail than in the somitic area. In the caudal PSM, the paraxial mesoderm is very soft, while the midline stiffness  $E'$  significantly increases from  $(270 \pm 36)$  to  $(947 \pm 111)$  Pa (Figure 3.4, lines 1 to 3, mean  $\pm$  SEM,  $p=0.0009$ ;  $0.005$ , Wilcoxon rank-sum test; Figure S3.2). At the somitic levels, the midline is still the stiffest structure, but the difference with the stiffness  $E'$  of the somites is negligible (Figure 3.4, lines 6, 7, 8,  $p=1, 0.89, 0.65$  left side and  $p=0.25, 0.27, 0.39$  right side, Wilcoxon rank-sum test).

Somites III to V are slightly stiffer than somite I, but not significantly (Figure 3.4 lines 8 and 7 vs. 6;  $p=0.18, 0.17$  left side, and  $p=0.66, 0.07$  right side, Wilcoxon rank-sum test). Similarly, the paraxial mesoderm increases its storage modulus on average from  $(527 \pm 38)$  Pa in the rostral PSM up to  $(746 \pm 44)$  Pa in the somitic region (Figure 3.4 lines 6, 7, 8 vs. 4 and 5:  $p=0.006$ , Wilcoxon rank-sum test).

Furthermore, Figure 4 shows a significant variation in stiffness  $E'$  in the caudal PSM when compared with the tail for both the midline ( $609 \pm 63$  and  $270 \pm 35$  Pa, respectively,  $p=0.0002$ ) and the paraxial mesoderm ( $558 \pm 44$  and  $181 \pm 14$  Pa,  $p=0.0001$ , respectively, Wilcoxon rank-sum test).

The observed trends can be logically related to the maturation of the chicken embryo (see micrographs in Figure 3.2). The caudal PSM is characterized, in fact, by stem cell-like mesenchymal cells that migrate actively with large intercellular space and lack a mature extracellular matrix (ECM) (Figure 3.2 A, confocal, and OCT section) [173]. Gradually, fibronectin and laminin become more abundant and interconnect rostrally (Figure 3.2 A widefield). This aids in anchoring the PSM cells by providing a substrate on which they can undergo collective migration and mesenchymal-epithelial transition (MET) to form epithelial spheres [173–176]. The PSM cells compact together, adhere to

the ECM and each other, and become more contractile (Figure 3.2A confocal section, compare caudal PSM with rostral PSM), thereby promoting fibronectin assembly. Concurrently, the notochord and neural plate quickly develop a high stiffness (Figure 3.2, lines 8 to 6). This behavior seems to support the idea that the notochord is not only an organizer center for chemical signaling but also acts as an 'embryonic spine' that plays a significant role in the mechanical integrity of the early embryo [145]. Next, the neural plate rostrally folds into the neural tube, and this morphogenetic movement could be due to a stiffer tissue that undergoes neurulation (Figure 3.3, lines 5 and 6). This finding agrees with previous studies on the *Xenopus*, where morphogenetic transformations are preceded by stiffening of the structures [110]. After neurulation, the neural tube keeps developing, but the presence of the lumen in the tube could lead to a softer tissue able to deform more when indented if compared to the compact neural groove (Figure 3.4, lines 4, 5 vs. 6, 7, 8; Figure S3.3).

Dynamic indentation reveals that a viscous component is present in embryonic tissues as well (*with  $E' \sim 3E''$* ); this is illustrated by the values of loss modulus  $E''$  in Figure 3.4. To describe the energy damping potential of the embryo under loading, the averaged damping factor,  $\tan(\varphi)$ , is shown in Figure 3.5 as the ratio between loss and storage modulus ( $E''/E'$ ). The values of  $\tan(\varphi)$  are comparable for the paraxial mesoderm, the midline, and the lateral mesoderm for the somitic area ( $p=0.27-0.97$ ). However, in the tail and PSM, damping capability is higher for midline and lower for paraxial mesoderm ( $p=0.0001, 0.02; p=0.02, 0.09$ , left and right, respectively, Wilcoxon rank-sum test) with the tail having overall highest damping factor ( $\tan(\varphi)=0.30-0.33$  vs.  $\tan(\varphi)=0.26-0.29$ ). Specifically, this finding could be related to the status of development with the epithelial tissues (more mature and with more extracellular matrix) being more elastic and less viscous due to their nature.



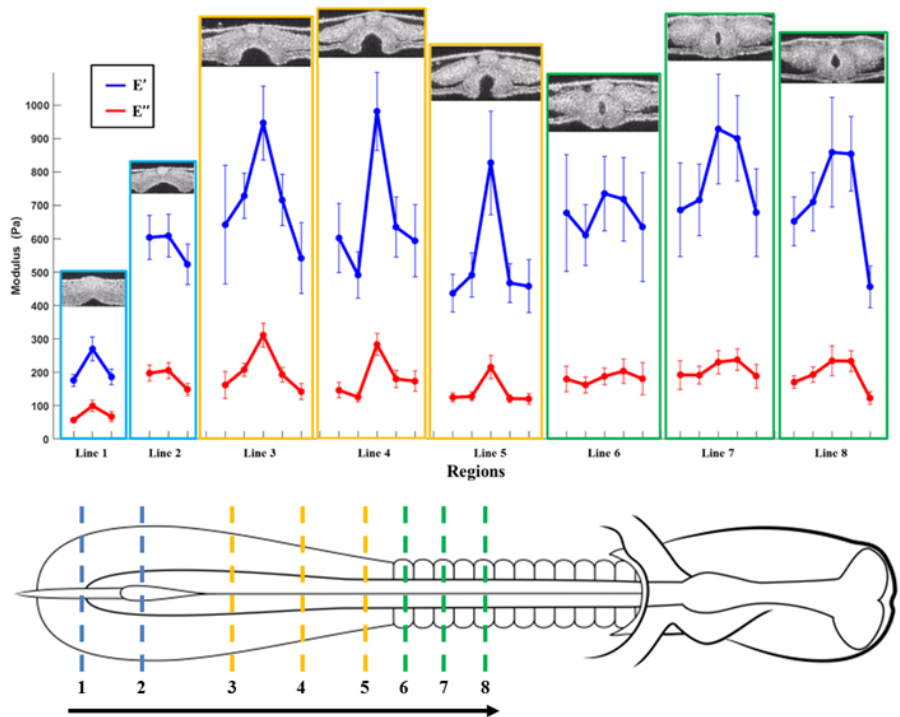


**Figure 3.4 | Averaged storage ( $E'$ , blue) and loss ( $E''$ , red) modulus along the embryo.** Transverse OCT sections show the positions of line 1 (most caudal) to line 8 (most rostral). Data points are averages of 12 embryos, with SEM error bars. Lines 1 and 2 shows three regions of interest: (1) left paraxial mesoderm, (2) midline, (3) left paraxial mesoderm. Whereas for lines 3 to 8, from left to the right, these are: (1) right lateral mesoderm, (2) right paraxial mesoderm, (3) midline, (4) left paraxial mesoderm, (5) left lateral mesoderm. The black arrow indicates the locations of the eight lines from tail to somites. OCT images: top –ventral side and bottom dorsal side.

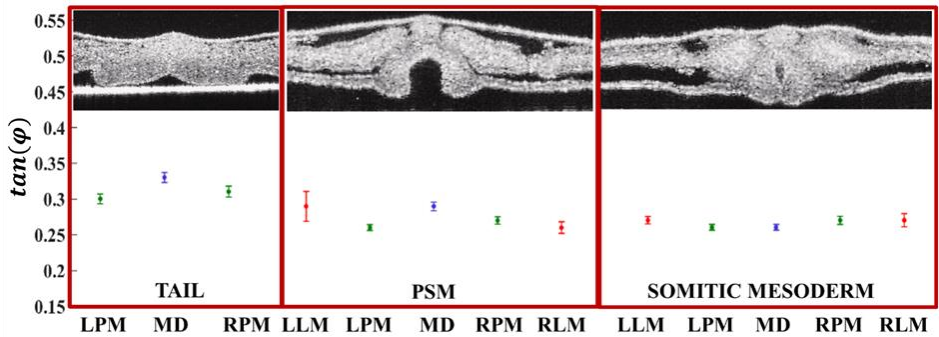


**Figure 3.5 | Averaged damping factor.**

$\tan(\varphi)$  of 12 embryos over lines from the same areas: tail (lines 1 and 2), presomitic mesoderm (lines 3, 4 and 5), and somatic (lines 6, 7, and 8), and with SEM bars. Abbreviations of the region of interest from left to right: (LLM) left lateral mesoderm, (LPM) left paraxial mesoderm, (MD) midline, (RPM) right paraxial mesoderm, (RLM) right lateral mesoderm.

It is worth to mention that averaging the viscoelasticity values from the same rostrocaudal regions over embryos resulted in logical trends of stiffness, that are commensurate with epithelization and matrix formation. Nevertheless, we observed substantial variation in viscoelasticity between single embryos. It appears that the biomechanical properties of the embryonic tissues may vary with the age and the quality of the embryo. As a point in case, differences in the handling of the embryos could have influenced their viability and, thus, their mechanical properties. Furthermore, the indentations are influenced by the accurateness of positioning the probe tip: small variations in positioning the probe along the embryonic structures could have led to local shearing or slipping of the probe along the tissue.

It is interesting to note that some of the mechanical features observed *in vivo* are different from the ones described for the fixed embryo [53]. The mechanical maps reported previously for the formaldehyde-fixed embryo [53] showed an increase of stiffness along the mesoderm from the caudal tip to the rostral somites, possibly related to the effect of the formaldehyde to fix tissue by cross-linking of the biopolymers. This result is not confirmed for the live embryos, where the midline stiffness is already high in the tailbud. This finding shows the effect of formaldehyde fixation on two complex embryonic structures: the notochord and the neural tube. By measuring *in vivo*, our instrument seems to be able to sense how the PSM (Figure 3.4, lines 3 and 4) is characterized by the opening of the neuropore, which has a large cell contraction as it closes to form a tube. Moreover, for the *in vivo* embryo, the low stiffness in the tail region is more evident if compared to the formaldehyde-fixed embryos, possibly due to a lack of structural components such as the neural tube and the notochord. One can argue/state that *in vivo*, we are able to sense mechanical properties caused by active biomechanical processes, such as stiffening by cellular contraction, while the measurements on fixed embryo are strictly linked to tissue morphology. This behavior seems to indicate that chemical fixation has two effects on the live soft tissue: it increases tissue stiffness and reduces the damping properties of the embryonic tissues.

Comparing elasticity of the midline, the paraxial and lateral mesoderm before and after fixation, the average storage and loss moduli were found to be a factor  $\sim 2$  times higher after fixation. In addition, the trends of  $\tan(\varphi)$  differs from the results obtained for the paraformaldehyde-fixed embryos. Furthermore,  $\tan(\varphi)$  is overall lower for the live embryo ( $\sim 1.4$  times). Moreover, it is interesting to mention that while observing the morphological features of the embryonic structure *in vivo* and after 2 hours of fixation via OCT, some regions of the embryo appeared to be structurally different: the

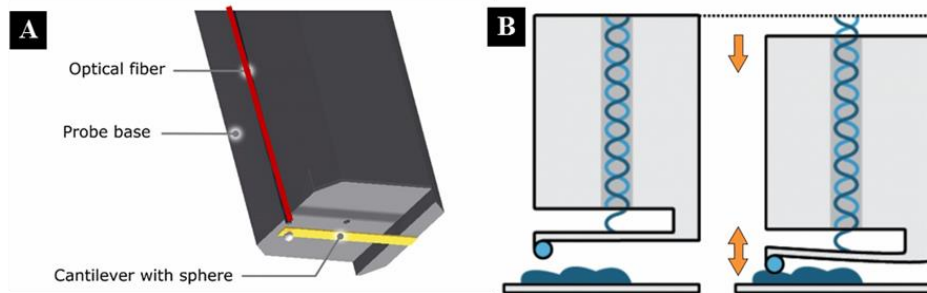
morphology of the embryo seems, in fact, more compact and dense (Figure S.3.3). By taking a closer look at the OCT images in figure S 3.3 for each of the analyzed locations, one can speculate that the tissue after fixation becomes denser and contains less fluid and, thus, the loss modulus increases more than the storage modulus resulting in a higher  $\tan(\varphi)$ . These findings provide key insights into differences between *in vivo* and chemically treated tissue and underline the importance of using *in vivo* tissue to study the biomechanics of embryos.

Specifically, our measurements show that the midline already stiffens near the tail and essentially acts as an embryonic spine. The damping factor is reduced when moving from tail to head, indicating a more elastic behavior for the more mature embryonic structures. Lastly, the method allows for sensitive detection of structurally distinct embryonic areas, both visually and mechanically. We demonstrate that our platform can reliably measure the viscoelastic properties of the tissue with more precision than previous studies [116], and allows one to discriminate between the small embryonic structures like somites and neural tube. Our technique can be further exploited to evaluate how regional viscoelasticity triggers not only cell behavior, but also organogenesis, as already demonstrated by Mammoto et al. for tooth formation [164,165], by Damon [166,167] for limb bud organization, and by Vuong-Brender and coworkers for embryonic elongation [177]. Finally, since mechanical stress can modulate physiological processes at the cellular and tissue level, we expect that this study will support a significant step forward in gaining new insights on the relationship between altered morphogenesis, stiffness, and pathologies during embryonic development.

### 3.4 Conclusion

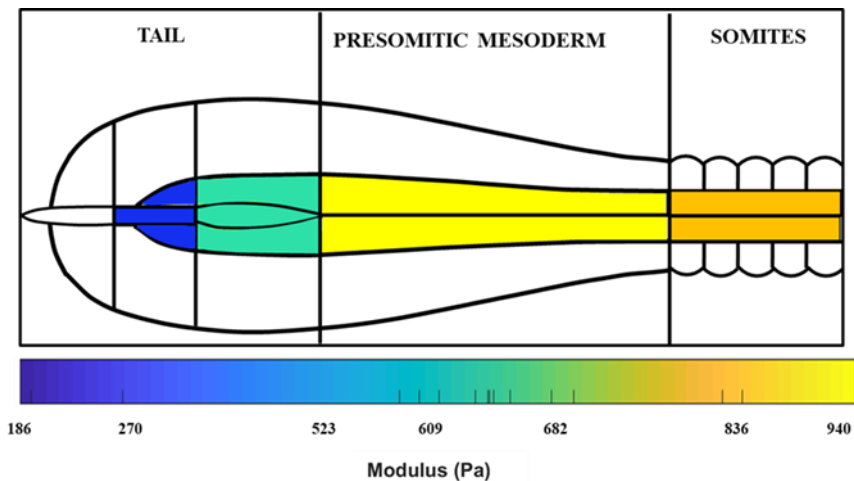
We demonstrate that our platform can reliably measure the viscoelastic properties of the tissue with more precision than previous studies (10), and allows one to discriminate between the small embryonic structures like somites and neural tube. Finally, since mechanical stress can modulate physiological processes at the cellular and tissue level, we expect that this study will support a significant step forward in gaining new insights on the relationship between altered morphogenesis, stiffness, and pathologies during embryonic morphogenesis.

### 3.5 Supplementary figures



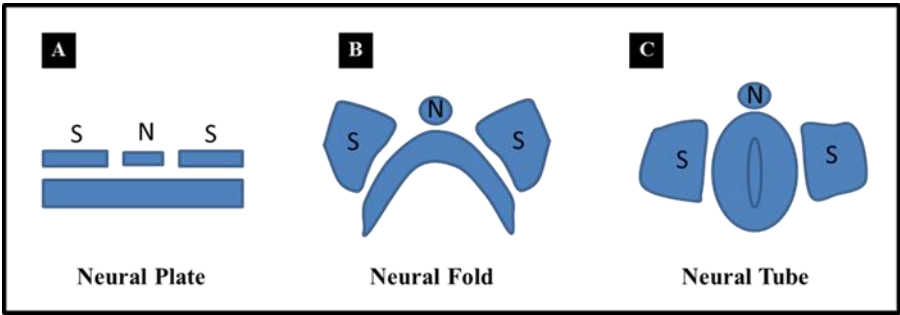
#### Supplementary figure 3.5.1 | Ferrule-top indenter.

Panel A) Schematic illustration of a ferrule-top indenter. The building block of the ferrule is a 3x3x7 mm<sup>3</sup> glass ferrule. A ridge is cut, and an Au-coated cantilever is glued on a borosilicate ferrule. The free end of the cantilever is further equipped with a spherical tip of 60  $\mu\text{m}$  in diameter to probe the tissue. A single-mode optical fiber (in red) is positioned on top of the ferrule to form an interferometric cavity of approximately 200  $\mu\text{m}$  over which cantilever deflection is measured. Panel B) Schematic illustration of the interferometric readout. When the cantilever is brought in contact with the sample, the cantilever deflects, and the light coupled from the optical fiber allows one to measure the bending of the cantilever and to derive the mechanical properties of the tissue.



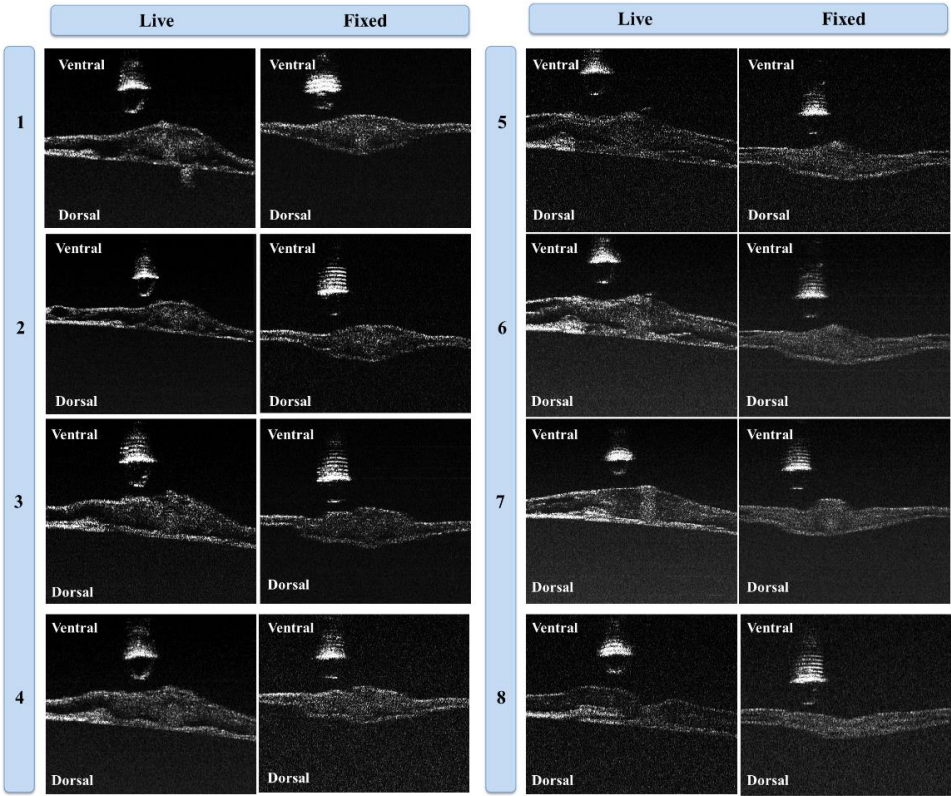
#### Supplementary figure 3.5.2 | Averaged stiffness ( $E'$ ) gradient from tail to somitic region.

An increase of the averaged storage modules is displayed from the tail up to the somites.



**Supplementary figure 3.5.3 | Development of the embryonic spinal cord.**

(A)The neural plate is generated as a columnar epithelium, then it starts to fold into a neural fold (B), and then the fusion of the neural folds forms the neural tube (C). Abbreviations: (S) somite, (N) notochord. Drawing not to scale.



**Supplementary figure 3.5.4 | Transverse OCT images of fix vs. live embryo**

Images of eight indentation lines on the same live and fixed embryo (the embryo has been imaged live, fixed for 2 hours and then imaged again at approximately the same locations).





# Chapter 4

## Ultrathin optical probes for Common Path Optical Coherence Tomography

### Abstract

The potential of Optical Coherence Tomography (OCT) for various diagnostic and therapeutic applications has motivated the interest in miniaturized probe designs. The emphasis has been focused on making ultrathin and flexible probes that could be used in micro-imaging and endoscopy applications. In this research, we investigate and validate a novel method to fabricate ultrathin fiber-top lenses for common-path OCT. We characterize the performance of the probes in terms of design methods, fabrication techniques, sensitivity, and imaging capability. Our probe system consists of a 65-75  $\mu$  m microsphere inserted into an inward concave cone, obtained by chemical etching, at the end of a single-mode fiber. Two types of commercially available microspheres with different refractive indexes are used: polystyrene-divinylbenzene with  $n = 1.59$  and barium titanate glass with  $n = 1.95$ . We demonstrate that, in air, both the microspheres perform comparably well, with an SNR around 60 dB and 3.5 mm of depth of field. However, in liquid environments, the high refractive index of the barium titanate microspheres significantly enhance system sensitivity and penetration depth.

---

Based on: M Marrese et al., 70  $\mu$  m diameter optical probe for common-path optical coherence tomography in air and liquids - Optics Letters 43 (24), 2018



## 4.1 Introduction

Common-Path Optical Coherence Tomography (CP-OCT) [178] is a well-established microscopy technique with potential applications in micro-imaging [179], endoscopy [180–183], needle-based OCT, [82,184,185] and surgical interventions [186–189]. For most of those applications, CP-OCT instruments rely on an optical fiber probe that transmits light into and from the sample via graded-index (GRIN) lenses [190,191], chemically-etched axicons [192–194], or ball-shaped lenses [83,195] (Note: Here, we exclusively consider forward-looking probes. For side-looking probes, we refer the reader to, for instance, [185,196,197]). In this paper, we introduce a new ball-lensed CP-OCT probe based on an etched optical fiber equipped with a  $\approx 65 \mu\text{m}$  diameter barium titanate microsphere, which is mounted on the inward cone left by the etching process on the cleaved end of the fiber. Our approach yields probes that have a smaller outer diameter than any of the GRIN-lensed and ball-lensed CP-OCT systems reported so far in the literature. With respect to axicons, our probes offer a larger depth penetration and higher resolution both in air and in buffer liquid solutions, where the high refractive index of the microsphere guarantees sufficient optical contrast at the lens-liquid interface. These features may eventually enable a broader utilization of CP-OCT imaging in ultrathin cavities or in applications that might require a set of closely spaced probes.

## 4.2 Material and Methods

### 4.2.1 Experimental details

Our ball-lensed optical fiber probes were fabricated according to the following protocol. The cleaved end of a single-mode fiber (SMF) (Corning SMF-28) is etched for 2 hours at room temperature in a buffered solution of hydrofluoric acid (Hydrofluoric acid, 48 wt. % Sigma-Aldrich, Netherlands) diluted in deionized water (40% v/v) (see [198–200]). The etching bath reduces the outer diameter of the fiber and, because of the different etching rate between core and cladding, creates a truncated conical cavity in correspondence of the fiber core (see Figure 1). The etched fiber is then fixed vertically on an x-y-z stage (NanoMax-300, Thorlabs GmbH) in the field of view of an optical microscope (A-zoom2 40X, QIOPTIQ, USA), where the tip of the fiber is briefly brought to contact with a micropipette covered with fresh droplets of two-component epoxy glue (UHU plusEndfest  $n = 1.61$ ). This procedure allows one to consistently deposit a small amount of adhesive in correspondence of the cavity. The tip of the fiber is further brought to contact with a barium titanate microsphere (BTGMS-HI-4.15, Cospheric LLC), which is held in position by means of another micropipette. When the sphere enters into contact with the glue, the capillary forces of the glue automatically drag the sphere into the cavity, resulting in a high degree of reproducibility and self-alignment[198]. Finally, the

fibers are left vertical for 90 minutes to allow the glue to cure.

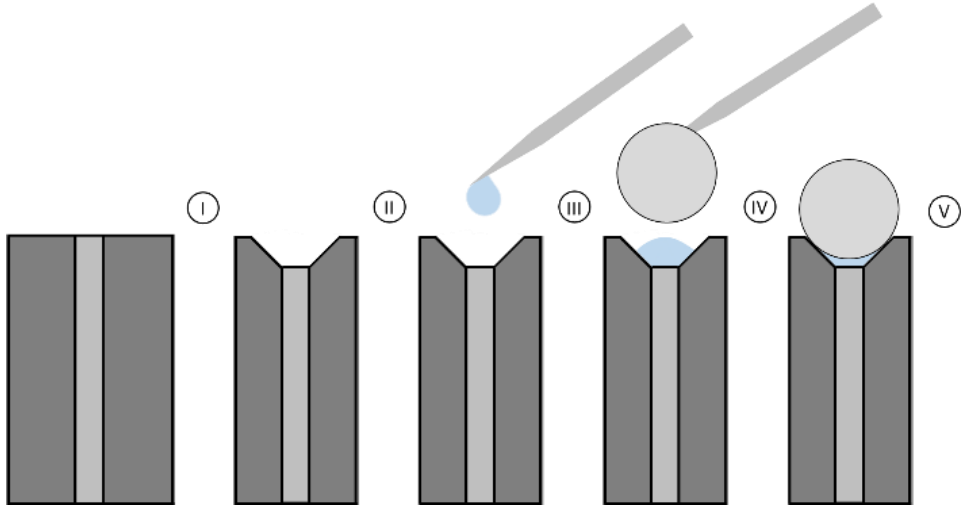


**Figure 4.1 | Illustration of the fabrication steps for the production of the optical probe (not to scale).**

(I) Initial cleaved fiber; (II) Fiber with a truncated conical cavity after the chemical etching treatment; (III) Injection of a two-component epoxy glue by means of a micropipette; (IV) Positioning of the barium titanate microsphere; (V) Final ball-lensed optical fiber probe.

The probes were tested using a commercial spectral-domain OCT system (Telesto II series, Thorlabs GmbH, Germany) in common-path mode. The system relies on a superluminescent diode (SLD, D-1300 HP, Superlum, Ireland) with a full-width half maximum (FWHM) of 85 nm and a central wavelength of 1310 nm. The output from the SLD is coupled into the probe via a broadband circulator (CIRC-3-31-PB, Gould Fiber Optics, USA). The light reflected at the fiber probe interface (i.e., the reference arm) and by the sample (i.e., the sample arm) couples back into the fiber and is sent by the circulator into a spectrum analyzer (Thorlabs 1310, Wasatch Photonics, Inc). The data collected are processed using a custom-designed program (Labview, National Instruments, USA). All OCT datasets presented in this work are shown as acquired, without any filter correction applied. To analyze the performance of our probes, we decided to focus on the following parameters: beam profile, roll-off A-scan test, and imaging capability. The beam profile was measured in air via a scanning slit optical beam profile system (BP209-IR, Thorlabs GmbH, Munich, Germany) with an InGaAs detector and a scanning slit of 25  $\mu\text{m}$ . Measurements were repeated as a function of separation along the direction of the beam propagation  $d_p$ , where  $d_p$  was varied, via a step motor, in steps of 50  $\mu\text{m}$  between  $d_p = 0.2\text{ mm}$  (the minimum value allowed by the scanning slit optical beam profile system) and  $d_p = 5\text{ mm}$ . The peak intensity of the roll-off A-scan

signal was measured in air and a Phosphate Buffered Solution (PBS) by positioning a mirror in front of the probe and varying the fiber-mirror separation  $d_m$ , via a step motor, from  $d_m = 0.1$  mm to  $d_m = 3.5$  mm, in steps of  $50 \mu\text{m}$  in air and  $200 \mu\text{m}$  in PBS. Data were collected without applying any apodization algorithm. To demonstrate the imaging capability of the probe developed, we further carried out 2D cross-sectional OCT scanning microscopy on two samples: a human finger and a mouse brain slice. The first measurement was performed in air, while the second one was performed in PBS.

### 4.3 Results and discussion

The fabrication protocol, tested on 50 probes, yields optical fibers with an outer diameter equal to  $73 \pm 2 \mu\text{m}$  and a  $16 \pm 1 \mu\text{m}$  deep conical cavity, equipped with  $65 \pm 3 \mu\text{m}$  diameter spherical lenses (Figure 4.2). By observing eight randomly selected probes through the optical microscope, we further found that the glue filling between the inner base of the truncated cavity and the microsphere has a length of  $11 \pm 1 \mu\text{m}$ , which does not significantly depend on sphere radius. By using the Fresnel equations to describe the reflection and transmission of the incident light at fiber–glue, glue–lens, and lens–medium boundaries, one can show that, due to the small difference in refractive index between the fiber core and the glue, the reflection from the fiber–glue interface is negligible. Moreover, the reflection from the lens–medium interface is 10 and 3 times stronger than the reflection from the glue–sphere reflection in air and water, respectively.

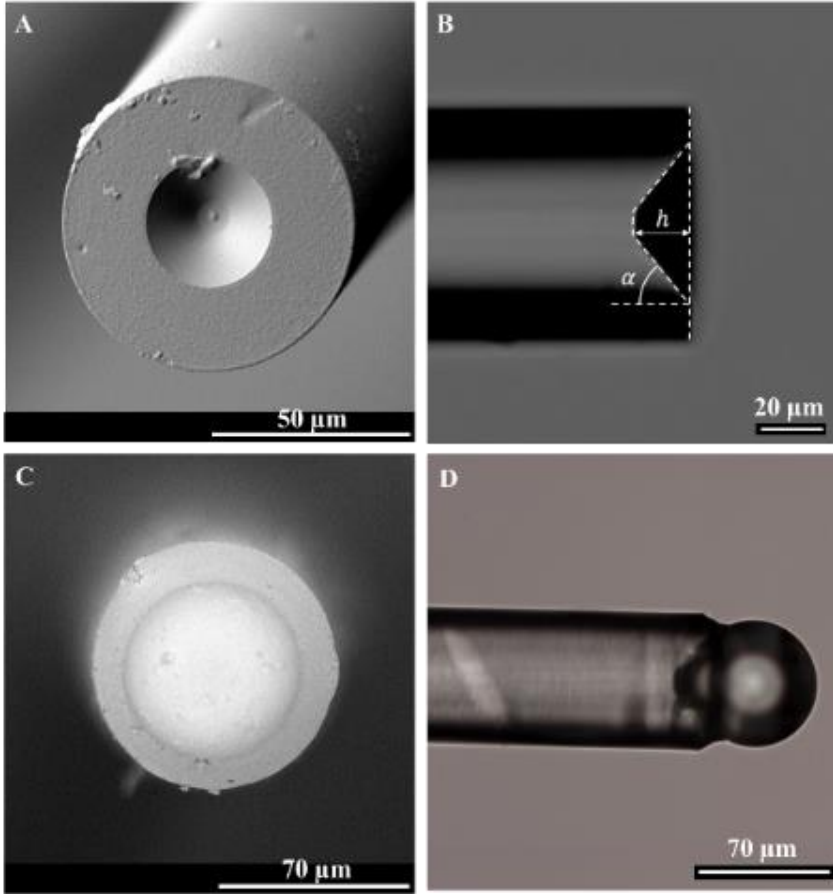


**Figure 4.2 | Scanning electron micrograph and optical microscope view of a concave cone-etched fiber.**

(A and B) and scanning electron micrograph and optical microscope of one of the completed probe fabricated for this paper (C and D).

In Figure 4.3 (first row) we report the profile images obtained for different values of  $d_p$ . The circular shape of those images confirms that the profiles are symmetric. Figure 4.3 (second row) also shows a typical distribution profile obtained with the scanning optical beam setup for  $d_p=0.5$  mm. The measured profile matches well with a Gaussian curve in both directions, suggesting that the microsphere is well aligned with the SMF core.

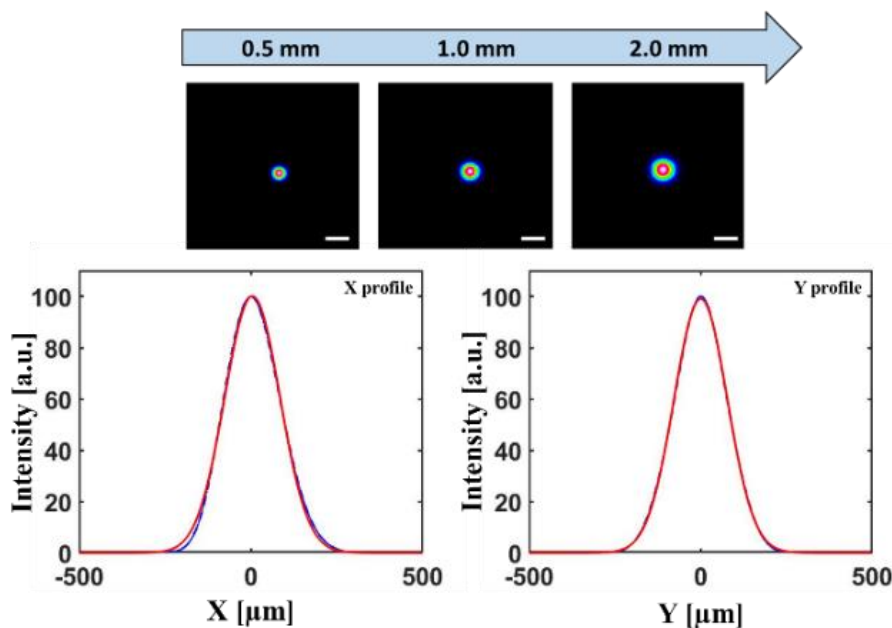


**Figure 4.3 | Beam profile.**

Top images: Measured beam profile images at 0.5 mm, 1.0 mm and 1.5 mm distance from the probe end. The scale bar corresponds to 500  $\mu\text{m}$ . Bottom graphs: Beam intensity distribution (blue) with Gaussian fit (red) in the x- (horizontal) and y- (vertical) axes at 0.5mm distance.

Figure 4.4 finally shows the FWHM of the Gaussian distribution profiles collected in the two orthogonal directions as a function of  $d_p$ . The values obtained from the analysis of the x-axis profile perfectly overlap with those obtained from the analysis of the y-axis profile, as expected for a symmetric beam. From the trend of the FWHM, one can also infer that the focal length of our probes is located at  $d_p < 0.2\text{ mm}$ . Unfortunately, our setup does not allow us to bring the probe any closer to the detector of the scanning optical beam profiler and, therefore, cannot be used to directly measure the lateral resolution of the system.

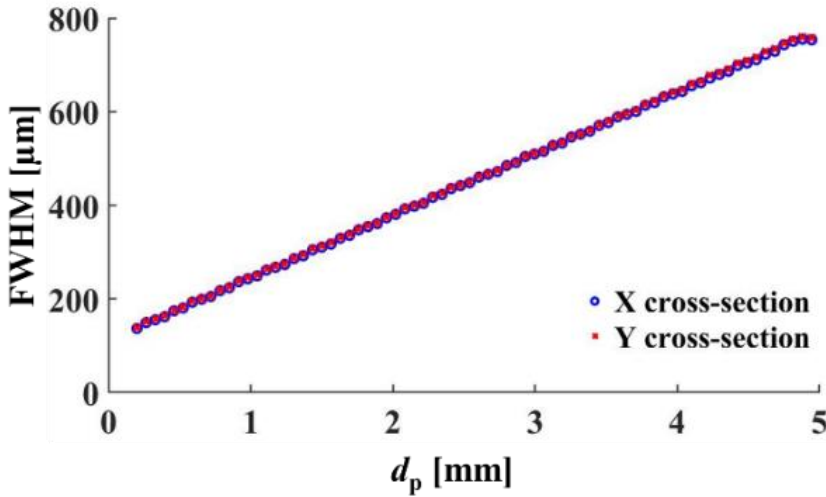


**Figure 4.4 | Full width at half maximum (FWHM).**

Measured FWHM plotted as a function of distance from the optical fiber probe.

Figure 4.5 (A) shows the results obtained with the roll-off experiment in air. As expected for a test performed at  $d_m$  larger than the focal length, the averaged (1000 x) intensity of the A-scan signal monotonically decreases with the increase of  $d_m$ . Increasing  $d_m$  from 0.1 mm to 3 mm, for instance, results in a drop in sensitivity from 83.38 dB to 48.68 dB. The -6 dB roll-off point is measured around 350  $\mu\text{m}$ . The roll-off data were further used to infer the signal-to-noise ratio (SNR) of our system, which was calculated as the ratio between the amplitude of the A-scan peak and the root-mean-square of the background noise measured when no reflections or backscatters were present. Figure 5 (B) shows the value of SNR obtained with this method as a function of  $d_m$ . The graph emphasizes that, at close separations, the SNR values are above 50 dB. An  $\text{SNR} > 30$  dB is still achievable at an axial distance of 3 mm from the fiber tip, demonstrating the capability of our ultrathin probe to perform well even for extended depth of field. Similar results were obtained when the probes were tested in PBS, as illustrated in Figure 4.5 (C and D). In this case, an SNR larger than 35 dB is still achievable for  $d_m < 1.8$  mm. The beam profile and the roll-off experiments, repeated two times with three randomly selected, different probes, show that the variability between each probe is negligible.

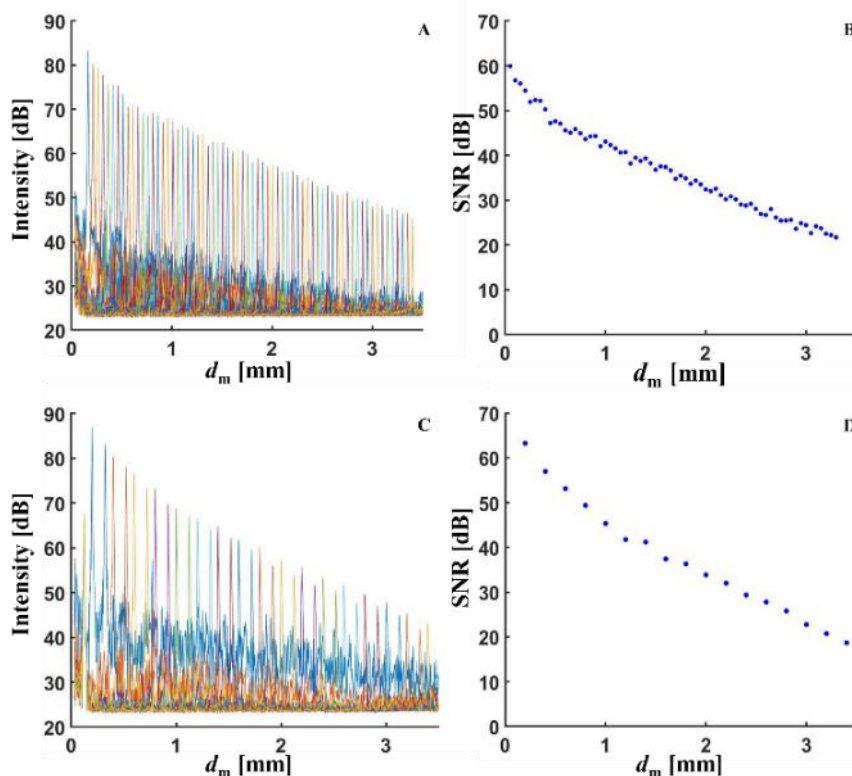


**Figure 4.5 | Roll-off A-scan and SNR performances.**

(A and B) in air and in PBS (C and D) plotted as a function of the distance between the end of the probe and the reflective mirror positioned in front of it.

Figure 4.6 shows in vivo images of a human finger and a mouse brain slice obtained with our system in air and PBS, respectively. The image quality is comparable to that offered by commercial systems, although the penetration depth is limited to approximately 1.5 mm. The results reported above show that, following the protocol described above, it is possible to reproducibly fabricate thin optical fiber probes for CP-OCT imaging. The fabrication procedure is relatively simple and cost effective and guarantees a good alignment between the core of the fiber and the focusing lens, as demonstrated by visual inspection and by the symmetry of the beam profile measured at the exit of the probe. Our roll-off measurements further prove that, in air, the intensity signal and the SNR are only 4 dB and 33 dB worse than the ones reported for larger lenses [201], respectively, and largely better than the ones obtained with axicons[190]. For distances larger than 200  $\mu$  m, our probes have a lower lateral resolution than the previously reported higher NA ones, but have a much smaller diameter (<75  $\mu$ m), which makes them ideal for in vivo imaging deep into the tissue. However, a higher lateral resolution could be obtained by using larger sphere with higher NA and/or with a lower refractive index. Importantly,

thanks to the high refractive index of the lens used ( $n=1.95$ ), the performance of the system does not deteriorated when the probe is immersed in a liquid – a major advantage for applications in life science experiments.

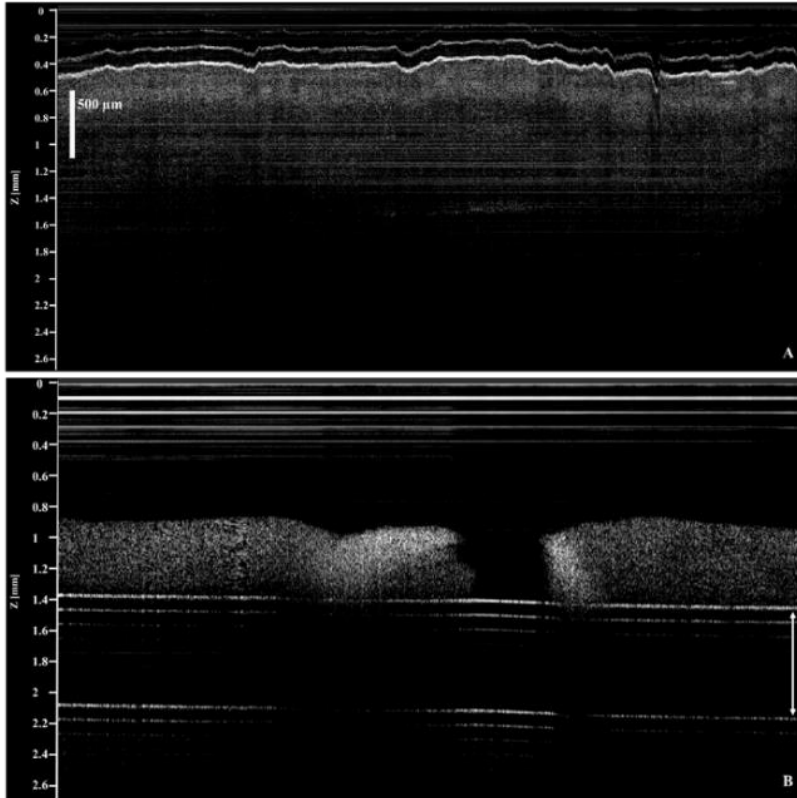


**Figure 4.6 | B-scan OCT images.**

(A) OCT B-scan images of human fingertips in air at a distance of 0.5 mm and (B) of mouse brain in PBS at a distance of 1 mm from the probe. The white arrow in the bottom image indicates the glass substrate. B-scans were obtained by translation of the sample stage.

## 4.4 Conclusion

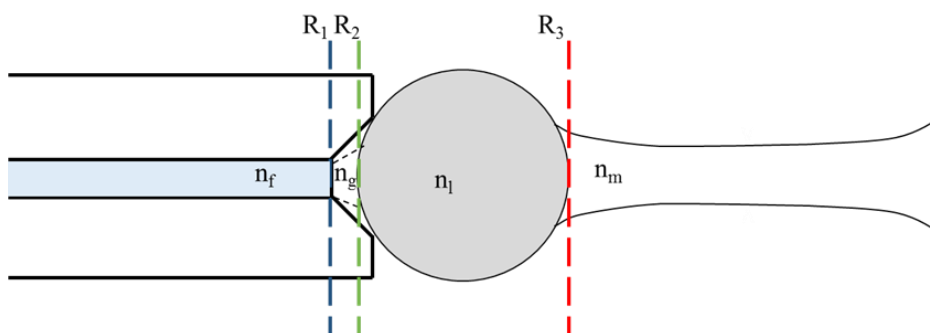
We described a novel approach to fabricate ultrathin microlensed probes for CP-OCT imaging. We showed that our probes allow successful acquisition of OCT images in terms of SNR and penetration depth both in air and liquids. Based on our findings, we believe that by tuning the main parameters of our probe (i.e., microsphere radius, refractive indexes, and concave cone dimensions), it is possible to tailor our probe design to achieve the desired imaging performance for different applications. Our preliminary findings might pave the way for the development of new instruments for in-depth tissue analysis,



with potential applications, among others, in the medical field, where small diameter probes might be integrated into the next generations minimally invasive tools.

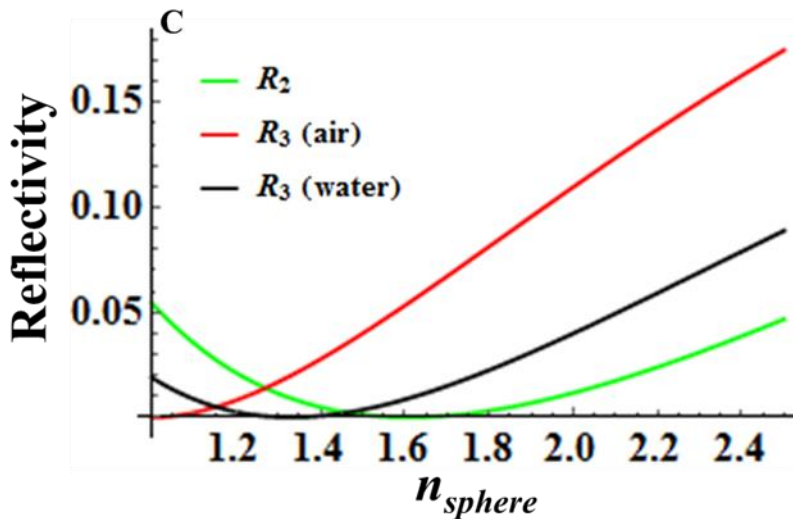
## 4.5 Supplementary material

A theoretical study of the probe has been carried out by employing a simple model based only on Fresnel reflection at the fiber-to-glue ( $R_1$ ) interface, glue-to-sphere ( $R_2$ ) interface, and sphere-to-medium ( $R_3$ ) interface. Considering the following refractive index -  $n_{\text{fiber}}=1.47$  (as indicated in the specs sheet - at 1310 nm Corning Single-Mode Optical Fiber -Product Information-2002),  $n_{\text{glue}}=1.61$  (experimentally measured),  $n_{\text{sphere}}=1.95$  (as indicated in the specs sheet), and  $n_{\text{air}}=1.00$ , one can calculate that, when the probe is in air, the amount of light reflected at the  $R_1$ ,  $R_2$ , and  $R_3$  is 0.2%, 0.9%, and 10% of the incident light, respectively. In water, due to the lower contrast between the refractive index of the sphere and the medium ( $n_{\text{water}}=1.33$ ), the light reflected at the  $R_3$  is reduced to 3.5%. The reference signal is thus dominated by the  $R_3$  interface (figures S.4.5.1 and S.4.5.2) both in air and in liquid environment.



### Supplementary figure 4.5.1 | Schematic view of light propagation.

Overview of the optical model for the incident light at the fiber-to-glue ( $R_1$ ), glue-to-sphere ( $R_2$ ), and sphere-to-medium ( $R_3$ ) boundaries.



**Supplementary figure 4.5.2 | Reflectivity.**

Relative reflection intensities plotted as a function of the lens refractive index.

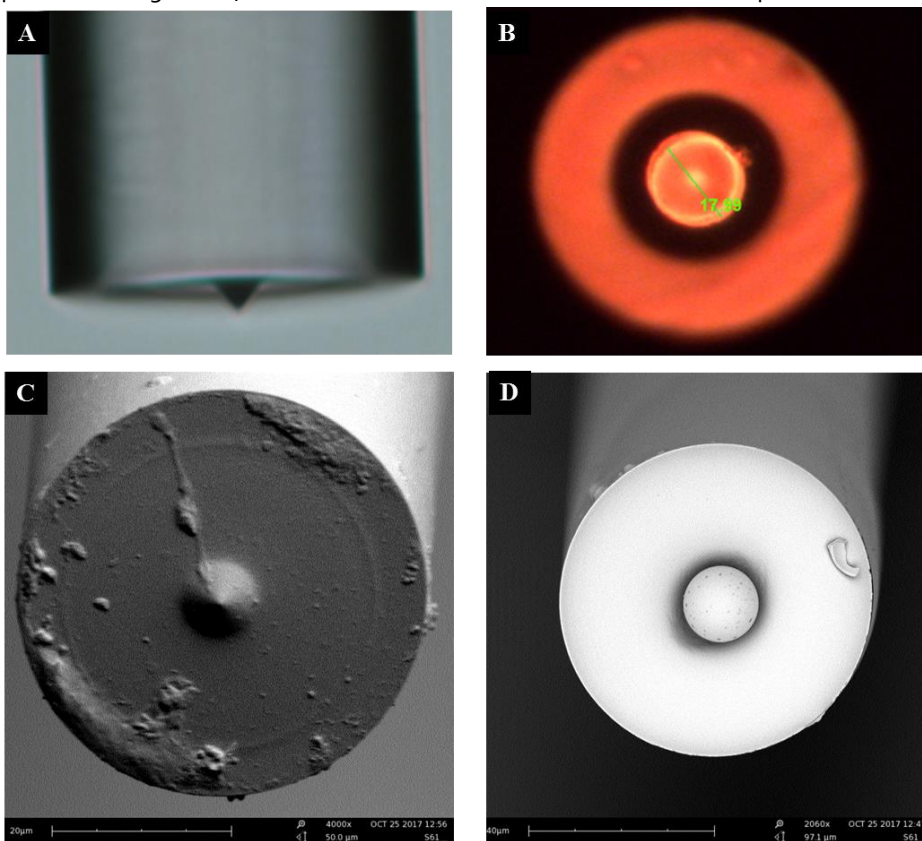
## 4.6 Notes

Chapter 4 describes the fabrication of spherical microlenses attached at the end of a single-mode fiber made of barium titanate. However, in order to evaluate the most efficient lens for our fiber-based Common Path-OCT system, we have evaluated several possibilities. The section below gives an overview of other lens types: axicon microlenses and glass microspheres with different sizes.

### 4.6.1 Axicon vs. 20 $\mu$ m microlenses

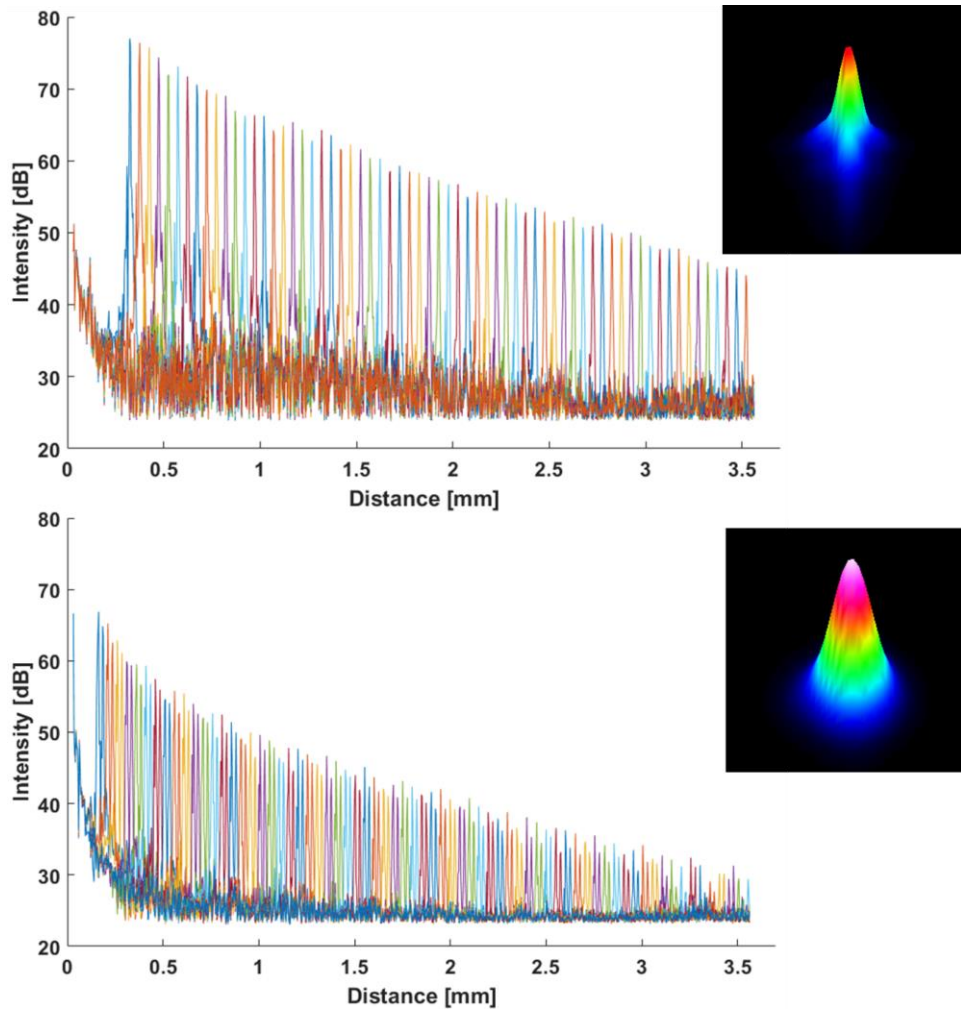
In order to improve our fiber-based Common Path-OCT system, we initially fabricated both axicon and concave cone microlens at the distal end of each optical fiber using a selective chemical etching method. For the axicon microlens, following the procedure described by Pangaribuan et al. [202], a single-mode optical fiber is immersed in a buffered hydrofluoric acid solution with concentration 1:1:7 (HF:H<sub>2</sub>O:NH<sub>4</sub>F) for about 6 hrs. Using this method, a tip size of 8  $\mu$ m was obtained at the distal end of the fiber. The fabrication of the concave cone tips is based on the same selective etched method, and it has already been described in the material and method section of Chapter 4. For this comparison, 20  $\mu$ m glass beads are inserted in the microcavity created at the end of the

optical fiber. Figure S.4.6.1.1 shows the results of both the fabrication procedures.



**Supplementary figure 4.6.1| Optical micrographs of the fabricated probes.**

Optical microscope view (top view) and scanning electron micrograph (bottom view) of an axicon microlens (A and C) and a concave cone-etched fiber (B and D) equipped with a 20 μm microsphere.



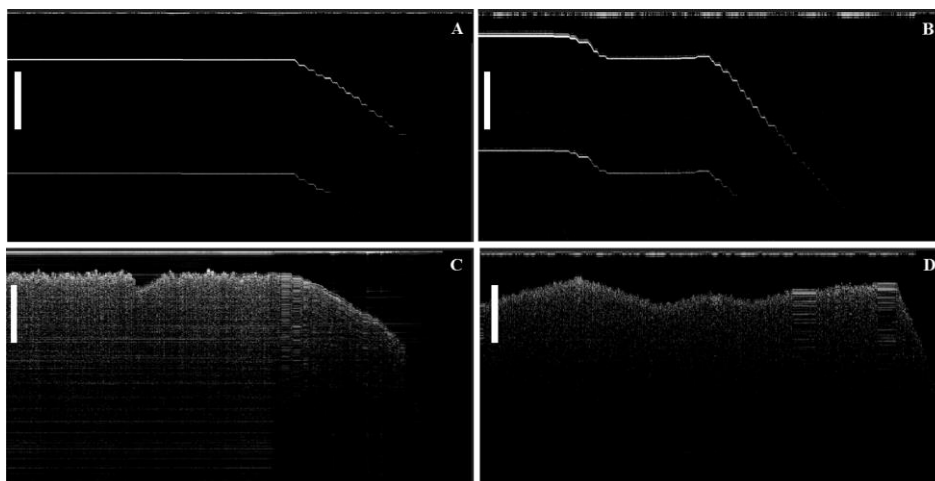
4

**Supplementary figure 4.6.2 | Roll-off A-scan.**

Roll-off A-scan performance in air for the axicon lenses (top row) and the microlenses (bottom row) plotted as a function of the distance between the end of the probe and the reflective mirror positioned in front of it.

For both the lenses type, the sensitivity did not change significantly at depth from 0 to 1 mm. However, from 1 to 3.5 mm, the descending slope is different for the two probes: the axicon probe has, indeed, the best performance with an intensity of ~50 dB compared to the ~30 dB of the microsphere lense, at 3.5 mm.

To validate the imaging capabilities of the etched probes we performed experiments using a 1310nm spectral-domain OCT on a glass microscope slide and IR card.



#### Supplementary figure 4.6.3 | OCT B-scan images.

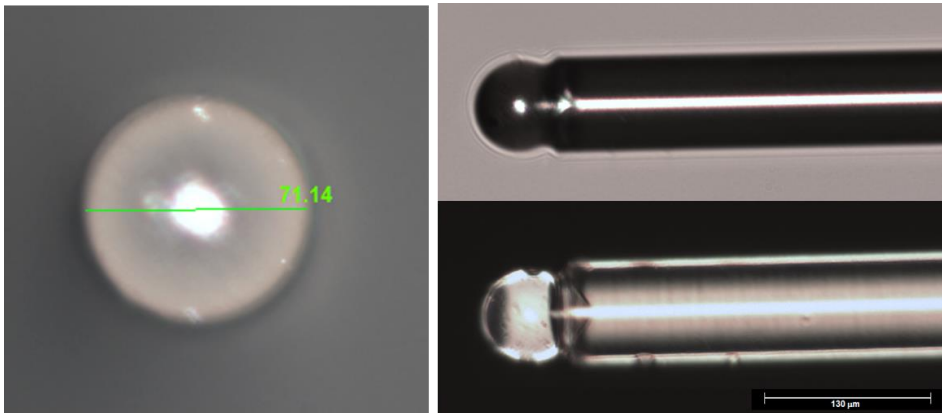
(Top view) In-air B-scans of a 1 mm thick microscope glass slide obtained with an axicon (A) and microlens (B) probe; (Bottom view) In-air B-scans of liquid crystal coated IR card obtained with an axicon (C) and microlens (D) probe.

Those results showed that the CP-OCT system, coupled to the axicon-tip fiber probe, could achieve an imaging depth of over 1 mm with a sufficient sensitivity, which is better than what one could obtain with the microsphere-tip fiber probe.

#### **4.6.2 75 $\mu\text{m}$ polystyrene microspheres**

Besides the barium titanate microsphere lenses reported in Chapter 4, an additional type of commercially available microspheres with different refractive index and radius has been tested: polystyrene-divinylbenzene with  $n = 1.59$  and  $r = (68.2 \pm 3.0) \mu\text{m}$ .

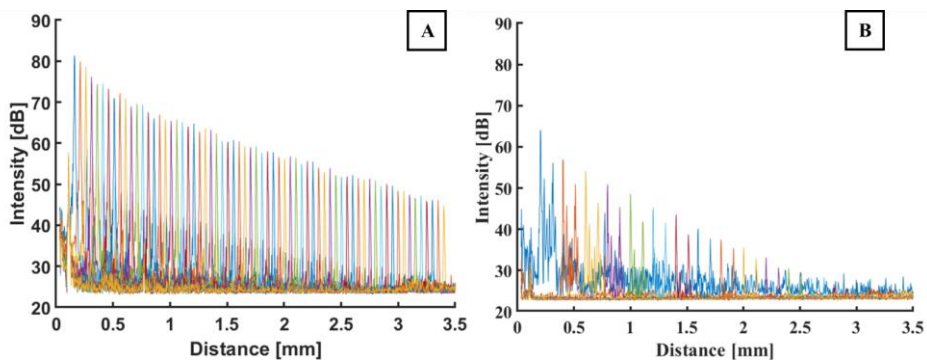
The probe fabrication, the performance, and its characterization methods have already been described in the material and method section of chapter 4. Therefore, in this section, we focus on the results achieved with this lens type.



4

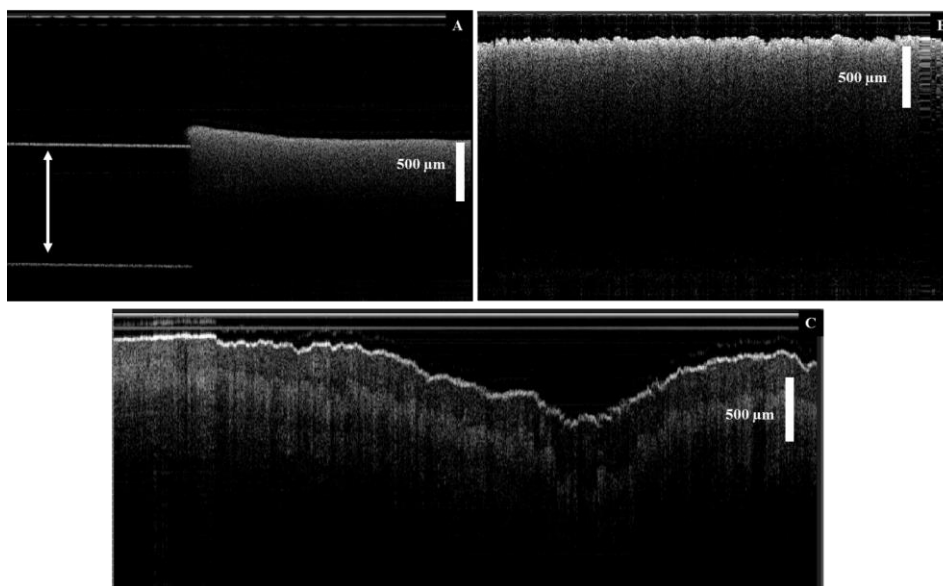
**Supplementary figure 4.6.4 | Optical microscope micrographs.**

Microscope images of the concave cone-etched fiber equipped with a  $\sim 70\ \mu\text{m}$  microsphere. Left: top view of the fabricated probe; Right: side view of two probes.



**Supplementary figure 4.6.5 | Roll-off A-scan.**

Roll-off A-scan performance in air (A) and in liquid (B) for the microlenses (bottom row) plotted as a function of the distance between the end of the probe and the reflective mirror positioned in front of it.



#### **Supplementary figure 4.6.6 | OCT B-scan images.**

In-air B-scans of a glass slide, partly covered with paper (A), and a liquid crystal coated card, photosensitive to infrared light (B); OCT B-scan images of human fingertips obtain in air at a distance of 0.5 mm from the probe (C). The B-scans were obtained by translation of the sample stage.

The performance of the polymer lens with  $n=1.55$  in air is comparable to the barium titanate lens showed in chapter 4 (figure 4.6.5 A). However, the lens performance in liquid is too low to obtain a high-quality OCT image, as shown in figure 4.6.5 B.

Moreover, figure 4.6.6 demonstrates that, when using this lens for OCT imaging in air, the global morphological features that one can discriminate are similar to those identified by a commercial system. However, in liquid environment, the sensitivity of this probe decreases significantly, as shown by the Roll-off A scan test in figure 4.6.2.2 (graph A vs. B).

### **4.6.3 Conclusion**

The axicon-tip fiber probe for the CP-OCT system could achieve an imaging depth up to 1 mm with a sensitivity that is superior to the 20  $\mu\text{m}$  microsphere-tip fiber probe. However, by using a different microlens size ( $d \sim 70 \mu\text{m}$ ), one can successfully acquire OCT images in air with a good SNR and penetration depth. Moreover, the higher refractive index ( $n = 1.95$ ) of the barium titanate microspheres (described in chapter 4) yield the highest sensitivity in both air and liquid environments if compared to the polystyrene-divinylbenzene ( $n = 1.59$ ), being sufficient to image biological samples even when the probe is at more than 1 mm distance.

## **Acknowledgments**

The authors acknowledge Fabio Feroldi, Martin Slaman, and Johannes F. de Boer for their input and technical support.





# Chapter 5 |

## Indentation probe with optical fiber array for Optical Coherence Tomography

### Abstract

We present a new optomechanical probe for mechanical testing of soft matter. The probe consists of a micromachined cantilever equipped with an indenting sphere, and an array of 16 single-mode optical fibers, which are connected to an Optical Coherence Tomography (OCT) system that allows sub-surface analysis of the sample during the indentation stroke. To test our device and its capability, we performed indentation on a PDMS-based phantom. Our findings demonstrate that Common Path (CP)-OCT via lensed optical fibers can be successfully combined with a microindentation sensor to visualize the phantom's deformation profile at different indentation depths and locations in real-time.

## 5.1 Introduction

The human body is continuously subjected to a variety of external forces while performing a multitude of activities. Therefore, the investigation of mechanical properties is crucial in several research fields and at all length scales, from cellular up to tissue and organ scale [203,204].

The local mechanical properties of soft biological materials are typically assessed via nano and micro-indentation by means of Atomic Force Microscopy (AFM) [205–209]. Here, a nanometer-size tip is mounted on the free-hanging end of a cantilever to indent the sample with a small force. By measuring the deflection of the cantilever, one can then obtain the elasticity of the sample at nano and microscale.

To contribute to this field, in 2010, our group proposed a new approach to precisely and locally map the tissue's viscoelastic properties at microscale by means of ferrule-top technology. The technique relies on a ferrule-top probe, which is obtained by assembling a rather macroscopic (compared to AFM) cantilever on a millimeter-sized glass ferrule. The cantilever is equipped with a sphere at its free-hanging end, which is brought in contact with the surface of a sample to allow the user to apply a mechanical stimulus. An optical fiber is then used to measure the deflection of the cantilever, providing the information needed to assess the mechanical properties of the sample, as in AFM nano-indentation [49,53,55,141,210]. Ferrule-top cantilevers are in general easier to use than AFM's, especially when the sample has to be kept in a liquid environment during the measurement (as is often the case with biological samples), and it has already been used by several research groups to assess the mechanical properties of biomaterials, tissues, and cells (see, for example, [211–224] and references therein).

Although indentation techniques can accurately probe the local mechanical properties of biological tissue, they suffer from one main limitation: the lack of optical imaging capabilities. AFM-like indentation sensors can, in fact, only provide data on the bulk mechanical response of the sample, without the possibility to discriminate subsurface deformations due to the application of the external load. A visualization of the inner structures of the sample would provide additional information for a better interpretation of the mechanical properties of the indented material.

Triggered by this series of considerations, in 2013 we demonstrated that the ferrule-top probes used for indentation can be modified to hold an additional optical fiber that, when connected to an Optical Coherence Tomography system, enables one to visualize how the subsurface layers of a sample deform under the application of an external load [225]. In this design, a hollow tube was used as an indenting tip to allow the light for OCT imaging to pass through the probe and reach the sample at the point of indentation. This configuration posed severe limitations on the quantitative analysis of the mechanical data since there are no analytical models for such an indenter shape. To overcome those limitations, a few years later, this approach was further improved [226] by using a half-ball lens indenter tip to probe the material. The half-ball lens indenter was also used as a

focusing element for the detection of the OCT signal.

Both of these designs incorporate only a single OCT-fiber, which acquires a one-dimensional OCT depth profile of the sample at the indenter contact point. However, to visualize the deformation of the sample during the indentation stroke, one needs to transversally scan the region of interest and reconstruct a cross-sectional image of the tissue around the indentation site. To this end, in this paper, we propose a new experimental sensor that combines an array of multi-OCT fibers with micro-indentation capability. The instrument is based on a miniaturized cantilever probe that compresses the sample with a small force and simultaneously collects OCT depth profiles around the indentation point. The integration of micro-indentation and OCT allows one to investigate, in principle, the mechanical properties of any material while acquiring 2D-profiles that show the tissue deformation during a single indentation stroke in real-time.

## 5.2 Material and Methods

### 5.2.1 Ferrule-Top sensor: design and fabrication

The building block of the sensor is a 5 mm × 5 mm × 10 mm 3D-printed ferrule, which has a 300  $\mu$ m ridge, 1 hole in the center, and 16 micro-grooves on the front side of the rectangular ferrule (pitch  $\approx$  300  $\mu$ m), as illustrated in figure 5.1. A half gold-coated borosilicate cantilever (300  $\mu$ m × 30  $\mu$ m) is glued on the ridge of the ferrule as in a standard ferrule-top configuration [49,51]. The free-hanging end of the cantilever is equipped with a spherical tip (diameter of 400  $\mu$ m) to probe the material. Next, a single-mode optical fiber (corning SMF128) is cleaved and mounted in the central hole of the 3D-printed ferrule, pointing at the reflective part of the cantilever, and is used to interferometrically read out the deflection of the cantilever during an indentation experiment (Figure 5.2). The 16 v-grooves are used to mount 16 single-mode etched optical fibers, each equipped with a  $\approx$  65  $\mu$ m diameter barium titanate sphere [227] (Figure 5.3).

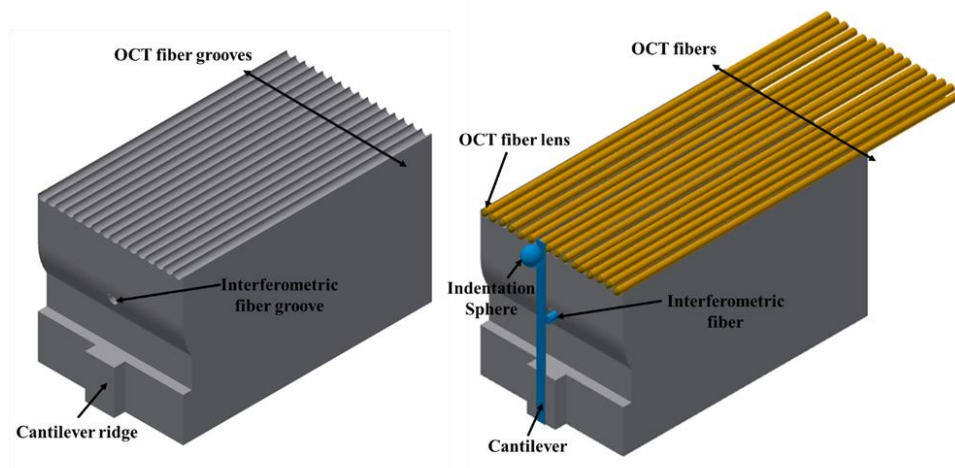


**Figure 5.1 | 3D printed ferrule-top probe.**

(Left) 5 mm × 5 mm × 10 mm 3D printed ferrule. The ridge to mount the cantilever, the interferometric groove, and the 16 OCT fiber grooves are depicted; (Right) front and side view of the ferrule.

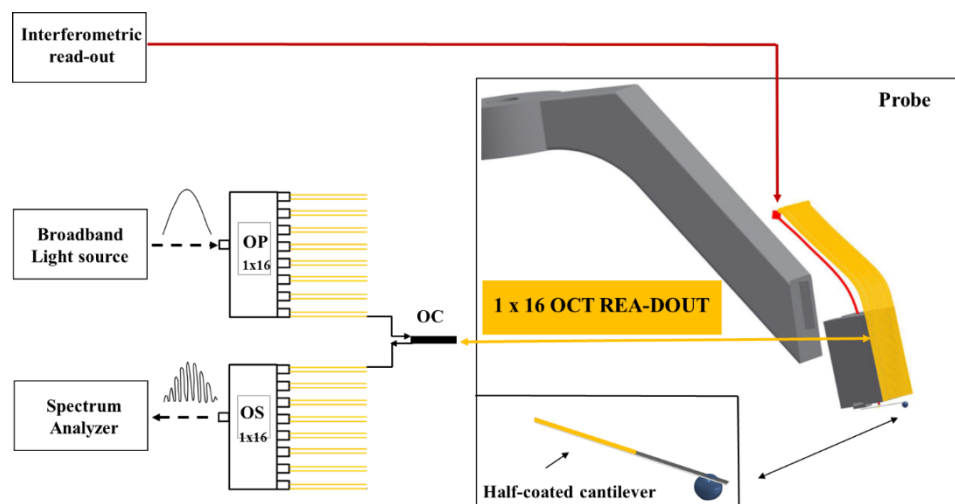


**Figure 5.2 | Schematic view of the OMNE setup.**

The OCT fibers (in yellow) are connected to a broadband-source optical coherence tomography readout via a 1x16 optical switch. The back-reflected light from the sample is coupled back to the detector of the OCT system via an optical coupler. The central optical fiber (in red), connected to an interferometer, allows one to measure the deflection of the cantilever and, therefore, to quantify the mechanical load applied to the sample during indentation. A magnified view of the half-coated cantilever equipped with a spherical tip employed to probe the sample is shown in the

bottom-right insert.

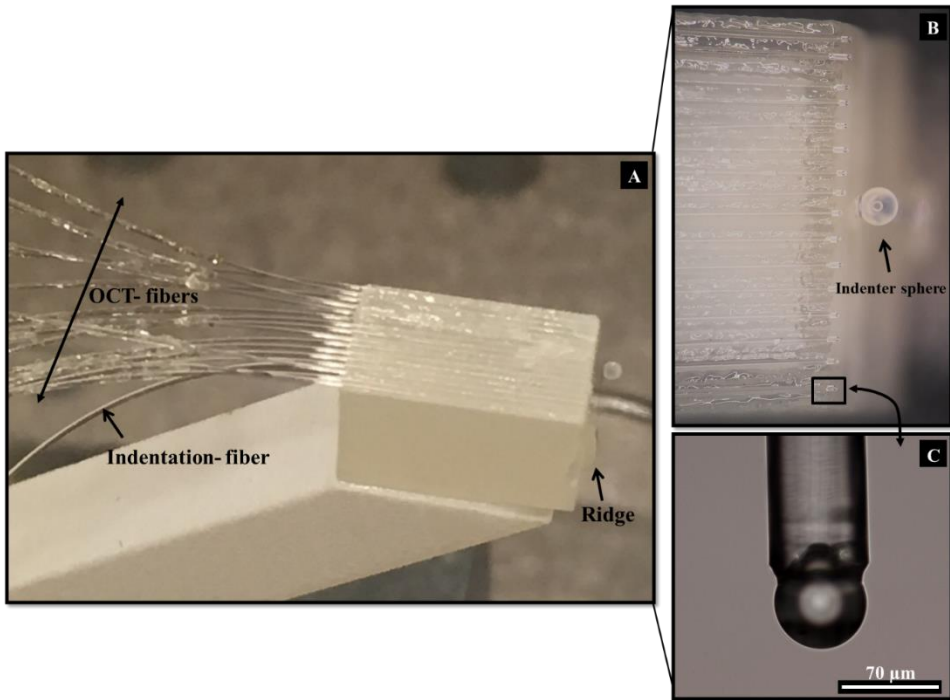


**Figure 5.3 | Ferrule-Top sensor.**

A) Ferrule-top sensor combining micro indentation and OCT: 1x16 OCT fibers glued on the top-facet of the 3D ferrule further mounted on a rigid 3D-printed arm; B) A magnified optical microscope view of the sensor hosting the OCT fibers. C) magnified view of one of the OCT fiber equipped with a spherical lens tip.

### 5.2.2 Experimental Setup

The optical fiber mounted in the central groove and aligned with the reflective part of the cantilever is connected to a commercial interferometer (OP1550, Optics11) to measure, via Fabry–Perot interferometry, the deflection of the cantilever. The 16 OCT fibers are connected to a spectral-domain OCT system (Telesto II series, Thorlabs GmbH, Germany) implemented in Common Path- OCT mode (CP-OCT). The layout of the system is shown in Figure 2. Briefly, the output of a superluminescent diode (SLD, D-1300 HP, Superlum, Ireland -with a full-width half-maximum of 85 nm and a central wavelength of 1300 nm) is fed to a liquid crystal 1x16 optical switch (CrystaLatch™ 1x16 Fiberoptic Switch, Agiltron, USA) that can reach a nominal switching time of 50 μs. Each fiber of our common path sensor is attached to one of the outputs of the optical switch. The signal collected from each of the fibers is connected to a broadband circulator (CIRC-

3-31-PB, Gould Fiber Optics, USA), whose exit is further sent to a 1x16 optical splitter. The output of the optical splitter is then connected to a spectrometer (THORLABS 1310, Wasatch Photonics, Inc.), which consists of an InGaAs line-scan camera (GL-2048-L, Sensors Unlimited, Inc., USA) with 2048 pixels. The raw data are collected and processed using a custom-designed LabVIEW (National Instruments, USA) interface.

Finally, the sensor is mounted on a piezoelectric stage operating in closed-loop mode, which is then used to drive the indentation stroke. Further details of sensor design and the experimental setup that combines optical coherence tomography with depth-sensing microindentation are reported as supplementary material.

### 5.2.3 OCT calibration procedure

Before each experiment, two types of calibration are performed: background subtraction and axial offset alignment. The background image is obtained when no scattering material is present in front of the sensor and is then subtracted from all subsequent scans. As far as the axial offset alignment calibration is concerned, one should consider that the facets of the OCT fibers are not perfectly aligned. This misalignment introduces relative axial shifts in the recorded A-scans. To overcome this issue, the probe is mounted in front of a flat surface, which allows us to measure the phase delay due to the misalignment. The misalignment is then compensated for during the actual indentation measurements. Both calibration procedures are directly implemented in Labview; therefore, no further post-processing of OCT data is performed. After the OCT calibration, the actual mechanical measurement starts. As the tip is pushed into the sample, the deflection of the cantilever, the indentation depth (obtained subtracting the measured deflection on the cantilever from the vertical motion of the piezoelectric stage to which the probe is anchored), and the 16 OCT depth profiles are simultaneously acquired.

### 5.2.4 Sample preparation

To test our approach, we used the sensor described above to indent and simultaneously image a PDMS-based phantom. The sample consists of a ~300  $\mu\text{m}$  thin membrane, made of Sylgard 184 polydimethylsiloxane (PDMS, 18:1 elastomer to curing agent ratio, Dow Corning) poured on a plastic ring. To improve the scattering properties of the material, the phantom was prepared with the addition of  $\text{TiO}_2$  particles suspended in OH-terminated silicone oil, following the fabrication steps indicated in Bartolini et al. (29).

## 5.3 Results

The indenter is based on ferrule-top technology[49,51,141], where a micro-machined

cantilever is used to indent the phantom. The OCT fibers detect the sample structure during the indentation stroke, allowing one to visualize how the subsurface layers of the indented material respond to the external load.

Before going into the details, we believe it is important to clarify that the goal of this paper is to test the working principle of the probe and not to validate its performance in identifying specific mechanical properties of the material. The latter would require an experimental effort that goes beyond the resources currently available. It is, however, fair to remind the reader that the use of ferrule-top technology for material characterization has already been discussed in numerous other papers [53–55,100,141,228].

Following the production protocol described in the method section, we produced several OMNE sensors. It is worth stressing that the lensed fibers proved to be prone to breaking during the fabrication phase; furthermore, the (manual) gluing process is rather complex and often leads to non-fully functioning probes. This is a severe limitation of this probe. As a matter of fact, the best probe we were able to fabricate could only count 11 working OCT fibers out of the 16 expected. For a more systematic use of this probe, it is therefore mandatory to find more suitable (possibly automated) assembly techniques.

Figure 5.4 shows the results of the two calibration steps: background subtraction and axial offset alignment. The latter was obtained by juxtaposing the probe and a ~1mm thick microscope glass.



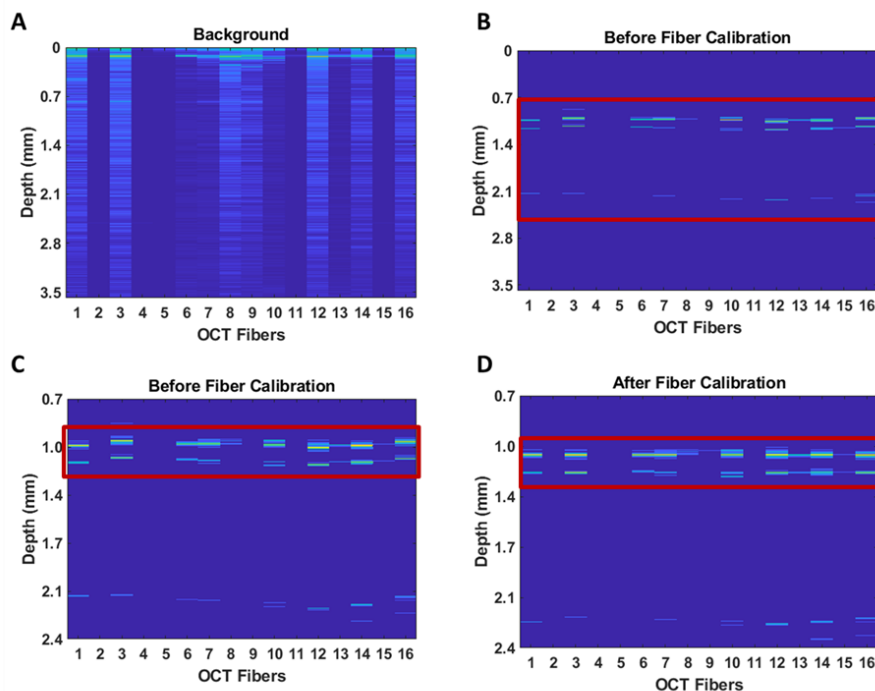


**Figure 5.4 | Probe calibrations.**

Top view: Background OCT scan (A) and OCT image of a flat microscope glass slide (B) before axial shift calibration. Bottom view: Zoom-in image of (C) the microscope glass slide before calibration and (D) B-scan of the same microscope glass slide after axial shift calibration. The probe is held at  $\sim 1$  mm from the glass slide.

As expected, the data acquired before the calibration, reported in figures 5.4B and 5.4C, result in a non-flat surface due to the misalignment of the OCT fibers in the Z-direction. On the contrary, in figure 5.4D, the corrected A scan shows that the top and bottom surface of the glass microscope slide are well-aligned. The commercial OCT system used in this study allows one to obtain A-scans (depth profile) up to 3.5 mm; therefore, to appreciate the misalignment due to the probe fabrication, it is necessary to enlarge the images (figure 4B vs. 4C -same B-scan but different y-scale).

In figure 5.5, we further show two typical offset-corrected A-scans obtained in this configuration. Each of the A-scans presents 3 or 4 peaks, depending on the sensitivity of the OCT fiber, and all peaks are well aligned. Specifically, peaks 1 and 2 represent the sphere-to-front surface of the microscope slide interface, as first (fiber-to-lens) and second reflections (lens-to-air), respectively. In contrast, peaks 3 and 4 are the sphere-to-rear surface of the glass slide interface, as first and second reflection.

The distances between the small peaks (peak 1 vs. peak 2) are  $\sim 125 \mu\text{m}$  for fiber 12 and

~ 118  $\mu\text{m}$  for fiber 14. However, the scale bar refers to the image depth that one would observe in vacuum ( $n = 1.00$ ); therefore, to obtain the correct geometrical distances, one has to consider the effect of the refractive index of the material's light travel through. Considering that the fiber lens is made of barium titanate with a refractive index of  $n=1.95$ , the peak-to-peak geometrical distances ( $d_g$  - peak 1 vs. peak 2 and peak 3 vs. peak 4) correspond indeed to the dimension of the lens (~ 65  $\mu\text{m}$  in diameter). The effect of the two reference surfaces (front and rear lens facet) adds two additional peaks in the OCT scans. Those kinds of reflections are unavoidable in these types of sensors, as they arise from the reflections due to the several interfaces the light has to encounter before reaching the sample. The  $d_g$  for peak 1 to peak 3 and peak 2 to peak 4 has been measured to be ~ 1 mm. Those distances correspond to the microscope glass slide (typically 1 mm thick). This set of data, together with the graphs showed in figure 3, also demonstrates that the lens has a penetration depth of at least ~2.5 mm.

To demonstrate the working principle of the probe, we performed a series of indentation experiments on a PDMS-based phantom while recording the OCT signal collected by the OCT fibers. Figure 5.6 shows the result obtained at 3 different depths, namely, 30  $\mu\text{m}$ , 40  $\mu\text{m}$ , and 60  $\mu\text{m}$ . The experiment demonstrates that the OCT data can reveal different deformation profiles under different indentation conditions. Specifically, in figure 5.6 A, one can notice that three interfaces are detected: surface 1 is the (fiber-to-) lens - front material interface; surface 2 is the lens (-to-air) - front material interface; whereas surface 3 represents the (fiber-to-) lens-rear material interface. In order to appreciate the deformation due to the indenter (micrometer deformation) due to increasing the indentation depth, in figure 6 (B-D), only the first surface of the PDMS sample (surface 1 and 2) is displayed for each indentation depth. The latter represents the reflection that originated from the focusing elements' top and bottom surface with the first PDMS layer. The distances measured for this set of data are ~  $d_g = 65 \mu\text{m}$  (surface 1 vs. surface 2 –red arrow in figure 5.6 A) and  $d_g = 320 \mu\text{m}$  (surface 1 vs. surface 2 –red arrow in figure 5.6 A). Similarly, the distance between the two surfaces detected in figure 5.6 (B-D) by the sensor has been measured to be ~  $d_g = 65 \mu\text{m}$  for all the investigated indentation depth.

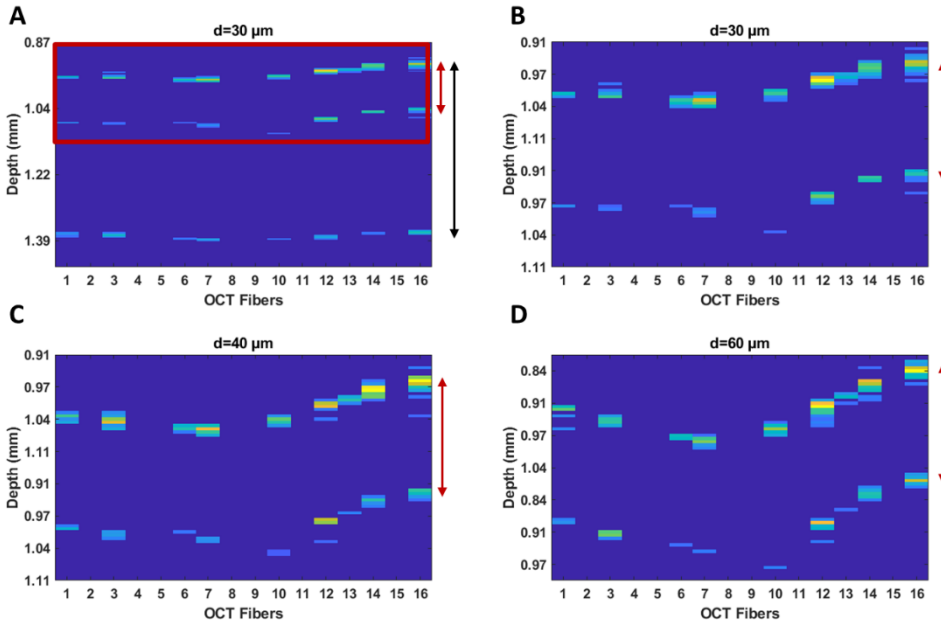


**Figure 5.6 | OCT B-scans.**

B-scan images acquired during indentation at different depths on a thin PDMS sample. The red arrow indicates the front surface of the sample as detected from the top and bottom surface of the focusing element, whereas the black arrow in figure 6A indicates the thickness of the samples. Y-axis depth:  $\sim 600 \mu\text{m}$  (A) and  $\sim 250 \mu\text{m}$  for (B), (C), and (D).

To further test the ability of the sensor to distinguish different types of deformations due to the indentation stroke, we performed two indentation experiments in two different locations of the PDMS-based phantom. The first location was selected close to the rim of the ring over which the PDMS membrane is suspended (figure 5.7 A), while for the second indentation, the probe was positioned some  $100 \mu\text{m}$  from the ring edge (figure 5.7 B). Our findings clearly show that both the indentation profiles are slightly asymmetrical since the probe is not positioned perfectly in the center of the sample with respect to the ring. Moreover, the effect of the rigid substrate that lies around the membrane appears more evident in figure 5.7 A, than 5.7 B, as one would expect due to the indentation location. The  $d_{op}$  between peak 1 and peak 2 (red arrow) is  $\sim 126.8 \mu\text{m}$  as for figures 5.5 and 5.6 and corresponds to the lens dimension ( $\sim d_g = 65 \mu\text{m}$ ). On the contrary, the distance between peaks 1 and 3 (black arrow) is, on average,  $\sim 305 \mu\text{m}$  for both the figures and represents the PDMS membrane's thickness as measured with a commercial OCT system (data not shown here).

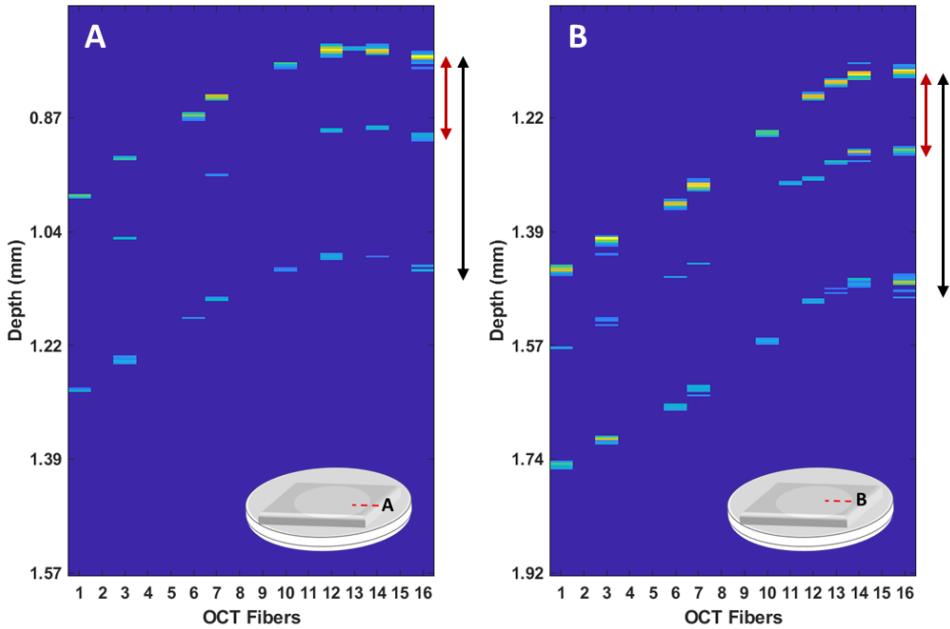


**Figure 5.7 | OCT B-scan during indentation on a thin PDMS sample.**

A) the probe is position on the edge of the membrane; B) the probe is moved far away from the edge. The red arrow indicates the front surface of the sample as detected from the top and bottom surface of the focusing element (peak 1 vs. peak2). The black arrow indicates the thickness of the PDMS samples (peak 1 vs. peak3).

## 5.4 Discussion and conclusion

Our work demonstrates that the general concept of a fiber-array optomechanical sensor able to simultaneously indent and collect depth information of a phantom has the potential of assessing the morphological properties of materials while performing mechanical characterization. Our findings prove that CP-OCT systems based on lensed optical fibers can be successfully combined with a microindentation sensor.

However, it is fair to mention that the sensor still has several limitations. The assembling of the 16 OCT fibers on the 3D-printed ferrule is tedious work, since the alignment, the mounting, and the gluing is performed manually and under an optical microscope. Furthermore, the printing resolution of the grooves, created to precisely mount the OCT fibers, is smooth; therefore, the alignment in the z-axis is suboptimal. Thus, more often than not, the OCT fibers are not pointing straight toward the sample, and the back coupling of the light from the sample back to the OCT fibers is usually weak, with significant deterioration of the OCT signal to the point that, for some fibers, the losses are so high that no A-scan can be collected.

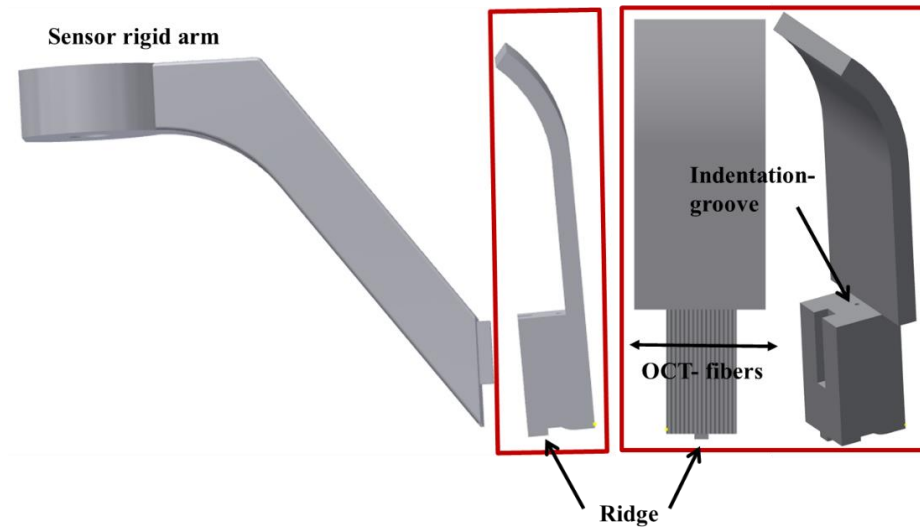
Although we recognize that several improvements in the fabrication steps need to be

implemented, it is also important to highlight some strengths of the method. To the best of our knowledge, this is the first fiber array sensor able to collect depth profile and indentation simultaneously, without limitations on the sample thickness or preparation. The use of a high refractive index lens allows the imaging fiber array to be held far from the sample due to the depth-of-field offered by the barium titanate lenses. This feature leaves sufficient space for the cantilever to bend and probe the material without touching the OCT fiber lenses. Moreover, the integration of OCT imaging with indentation techniques could be further exploited by introducing ad hoc mathematical models able to extrapolate multiple information from single OCT depth profiles; one could think of providing a more extensive evaluation of deformation profiles in relation to the local material composition or to apply specific OCT algorithm for a more accurate extrapolation of peak profiles or other information hidden in the sample. Thus, the combination of OCT with micro indentation opens new ways to explore a whole range of information (e.g., sample topography, multi-layered structures, thickness, and mechanics) that are neglected while choosing either microindentation or optical imaging separately.

## **Acknowledgments**

We thank Luca Bartolini, Fabio Feroldi, Martin Slaman, and Johannes F. de Boer for their input and technical support.

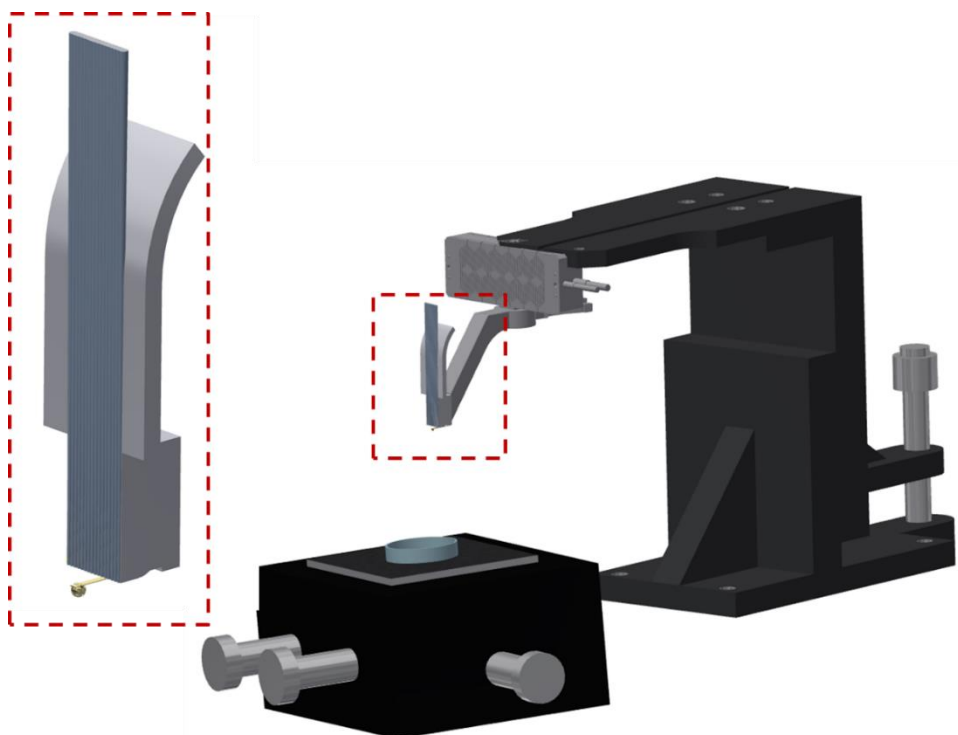
## 5.5 Supplementary figures



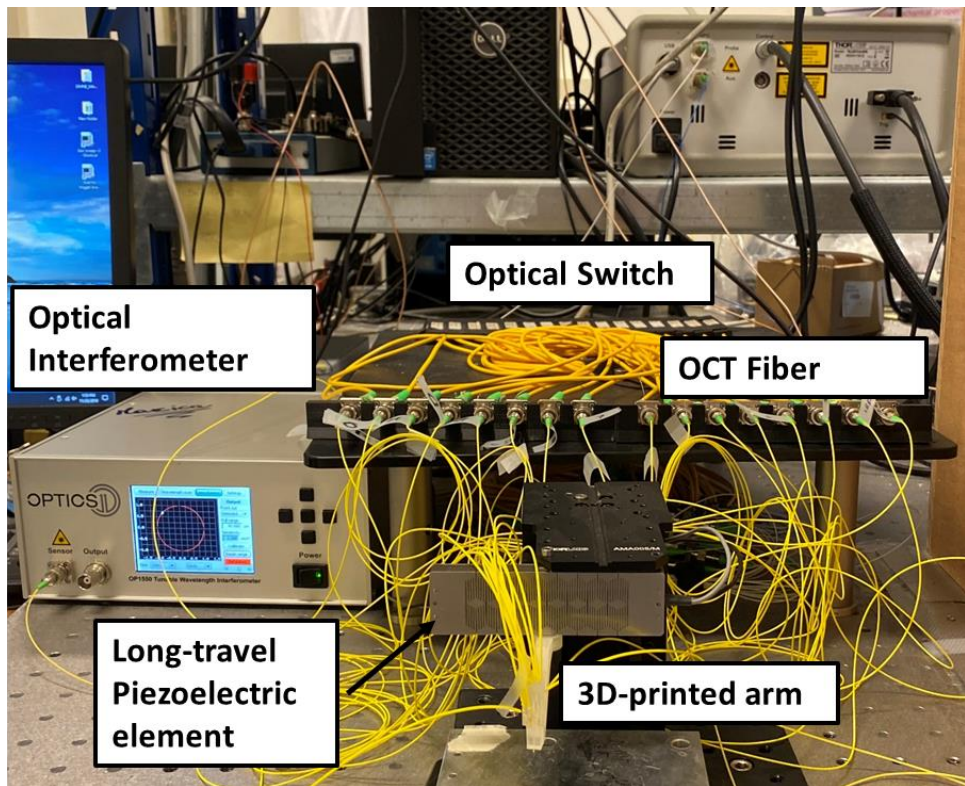
### Supplementary figure 5.5.1 | 3D-printed ferrule-top probe assembly.

The 3D-printed ferrule is mechanically embedded on a rigid arm used to mount the sensor on the Z-piezoelectric actuator.

5

**Supplementary figure 5.5.2 | Sketches of the setup.**

A ferrule-top probe is equipped with an optical fiber for interferometric readout of the cantilever and with a spherical tip to indent the sample. The 16- OCT fibers are mounted on the top facet of the 3D printed ferrule (left). The sensor is then mounted on the Z-piezoelectric actuator, which is solidly attached to an XYZ manipulator (right).



5

**Supplementary figure 5.5.3 | Image of the setup.**

OCT imaging is obtained from the 16-fibers connected to the Optical switch while the sensor hovers above the sample. Indentation measurements make use of the interferometric readout and are driven by the piezoelectric element.





## Chapter 6 |

# Investigating the effects of mechanical stimulation on retinal ganglion cell spontaneous spiking activity

### Abstract

Mechanical forces are increasingly recognized as major regulators of several physiological processes at both the molecular and cellular level; therefore, a deep understanding of the sensing of these forces and their conversion into electrical signals are essential for studying the mechanosensitive properties of soft biological tissues. To contribute to this field, we present a dual-purpose device able to mechanically stimulate retinal tissue and to record the spiking activity of retinal ganglion cells (RGCs). This new instrument relies on combining ferrule-top micro-indentation, which provides local measurements of viscoelasticity, with high-density multi-electrode array (HD-MEAs) to simultaneously record the spontaneous activity of the retina. In this paper, we introduce this instrument, describe its technical characteristics, and present a proof-of-concept experiment that shows how RGC spiking activity of explanted mice retinas respond to mechanical micro-stimulations of their photoreceptor layer. The data suggest that, under specific conditions of indentation, the retina perceive the mechanical stimulation as modulation of the visual input, besides the longer time-scale of activation, and the increase in spiking activity is not only localized under the indentation probe, but it propagates across the retinal tissue.

---

Based on: M Marrese<sup>†</sup>, D Lonardoni<sup>†</sup>, F Boi<sup>†</sup>, H van Hoorn, A MAccione, S Zordan, D Iannuzzi, L Berdondini. Investigating the Effects of Mechanical Stimulation on Retinal Ganglion Cell Spontaneous Spiking Activity. *Frontiers in Neuroscience*. (2019)

<sup>†</sup> These authors contributed equally

## 6.1 Introduction

Eukaryotic cells are constantly subjected to biomechanical interactions with the extracellular environment. Mechanical forces play a fundamental role in many different aspects of a cell birth, life, and death. Starting from stem cells, external forces and environmental mechanical constraints are vital in order to trigger the differentiation process and to define the cell fate both in embryonic development [229–231] and in adulthood [232] with the unprecedented possibilities to design biomechanical therapies for in vivo tissue regeneration. Not only single cells but also entire organs, such as heart [233–235] and lungs [236], are strongly affected by mechanical forces that can change their cellular organization, structure, functionalities, and electrophysiological signaling. Furthermore, also biomechanical forces exerted on cells in the brain have important, yet partially understood effects on the physiological development and functional behavior of brain circuits [237]. Neurons and glial cells are embodied in brain circuits, and intrinsically experience physical cues due to their surrounding physical world, which include, among others, electrochemical gradients and mechanical stresses [238,239]. At the cellular level, mechanotransduction can influence several cellular processes in the brain, including differentiation, survival, proliferation, and migration, thus contributing to its physiological or pathophysiological development [240]. The role of cellular mechanotransduction has also been associated with cellular and sub-cellular injuries that may ultimately lead to the diffusion of pathological damage in traumatic brain injury [241]. Additionally, biomechanical forces are involved in cerebral cortical folding as well as in folding abnormalities in neurodevelopmental brain disorders.

Unraveling the functional role of biomechanical forces in brain circuits is, therefore, a crucial research topic in neuroscience. However, the investigation of contact forces (e.g., shear, compression, or tension) in modulating brain circuit's physiological functions requires technology advances. In this direction, here, we propose an experimental platform to probe the electrophysiological effects of controlled contact forces in brain circuits with an unprecedented resolution. This technique offers a unique opportunity to investigate the effects of mechanical stimulation on the electrophysiological activity of neuronal tissue, such as cell culture networks, brain slices, and retina samples, at the single-cell resolution and over a wide portion of biological tissue. To demonstrate the probing performances of this technique, here we investigated contact force effects on the electrophysiological responses to visual stimuli in explanted mice retinas.

The retina is the light-sensitive tissue devoted to convert and pre-process variations of light intensity into spike trains that are decoded by downstream areas of the brain to generate visual perception. While the light-sensitive properties of the retina are widely studied because they represent the principal and fundamental characteristic of the tissue, its mechanical and mechanosensitive properties are currently under-investigated. The retina, however, is constantly subjected to mechanical stresses induced by intraocular pressure, suction forces pulling the outer retinal surface [242], and inertial

forces applied by the vitreous body upon physical shocks, traumatic events, or rapid eye/head movements [243]. Mechanical forces, as tension, hydrostatic pressure, shear, stretch, compression, and torsion provide cells with essential cues about the surrounding physical world and ultimately impact cell viability. Specifically, in the context of the retina, pathologies such as axial myopia and glaucoma may arise from prolonged mechanical stress [244,245].

Interestingly, to cope with and transduce a mechanical signal, several populations of mouse retinal cells, as Müller cells, Retinal Ganglion Cells (RGCs) and photoreceptors are equipped with mechanoreceptors [246] — a mechanically gated family of ion channels activated by signal pressure or tractional forces. Defective or impaired activity of these channels has functional implications on retina physiology by affecting reception and integration of synaptic signals [247], involving Müller cells K<sup>+</sup> clearance [248]. The presence of such receptors suggests that the retina might collect sensory information not limited to the visual scene but also reflecting the current state of the tissue [249]. Indeed, elevated intraocular pressure regulates retinal ganglion cells excitability [250]. Furthermore, mechanical stimulation of Müller cells — the major astrocytic population in the retina — induces waves of calcium [251] that modulate the RGCs spiking response to white/black flash cycles in mouse retinas [252] and are known to be sensitive to mechanical stretches [253]. In addition, in a pivotal study, Grusser et al. [254] reported the induction of phosphenes (i.e., the perception of variations in light intensity when no visual stimulation occurs) upon application of physical pressure through stretching cat eyeballs. Specifically, after a latency of 0.2-4.0 sec, the mechanical stimulation activated ON RGCs and inhibited OFF RGCs during the stimulation time-window and determined transient responses in a subpopulation of ON RGCs upon pressure release.

Similarly, the exploitation of retinal mechanosensitive properties has been recently proposed as a new technological approach for prosthetic purposes [255]. Indeed, it was shown that mechanical stimuli induced by pulses of a physiological solution injected within the internal layer of rat retina could elicit localized RGCs responses, with amplitude and latencies comparable to those observed with direct light stimulation, even in retinas with degenerated photoreceptors. Finally, in micro electroretinograms (microERGs) experiments, the application of extra weight onto the retina to improve the coupling between retinal ganglion cells and electrodes affected the response to full-field flashes, although not significantly [256].

To disentangle the mechanosensitive features that might influence visual information encoding in the retinal circuit, in our experiments we mechanically stimulated the retina with micrometer precision from the side of the photoreceptor layer and simultaneously recorded the spiking activity of thousands of RGCs at the pan-retinal scale. To do so, we combined a depth-controlled force transducer with a high-density multi-electrode array (HD-MEAs) in order to record extracellular RGCs spiking activity while photoreceptors were mechanically stimulated. The electrophysiological acquisition system provides sub-

millisecond recordings from a 64x64 grid of 42 $\mu$ m-spaced electrodes covering an area of 2.67mmx2.67mm, which is comparable to the extension of a mouse retina.

Simultaneous use of these two technologies allows one to perform systematic studies on two interconnected topics: on the one hand, the mechanical properties of the retina can be characterized through tissue microindentation; on the other hand, our approach can reveal how a localized mechanical stimulation on the photoreceptor layer may trigger or affect the spontaneous spiking activity of retinal ganglion cells, i.e., the output neurons of the retina. We present here, for the first time, a depth-controlled mechanical characterization of the retinal tissue that confirms and extends the work of Franze et al. [257] by highlighting the viscoelastic nature of the sample. We further demonstrate that, under specific indentation conditions, mechanical stimulation can induce a response in a subset of RGCs, suggesting that the retina integrates the effects of biomechanical forces when encoding visual inputs.

## 6.2 Material and Methods

### 6.2.1 Ethics Statement

All the experiments were performed in accordance with the guidelines established by the European Community Council (Directive 2010/63/EU of 22 September 2010). All procedures involving experimental animals were approved by the institutional IIT Ethic Committee and by the Italian Ministry of Health and Animal Care (Authorization number 110/2014-PR, December 19, 2014).

### 6.2.2 Experimental Setup

The setup consists of an indentation arm, a chip-based electrophysiological platform, and a sample holder (see figure 6.1). The indentation arm includes an XYZ micromanipulator (PatchStar, Scientifica, UK), a Z-piezoelectric actuator (PI p-603.5S2, Physik Instrumente), and a ferrule-top indentation probe connected to an interferometer (OP1550, Optics11, The Netherlands). The indenter is based on a micro-machined cantilever spring, operating as a force transducer. An extensive description of the probe fabrication and the indentation setup can be found elsewhere [51,258]. A custom-written LabVIEW software (National Instruments) is used to process signals and to control the devices through a data acquisition card (PCIe-6361, National Instruments). Retina samples are submerged in the perfusion chamber and fixed on a high-density multi-electrode array (HD-MEAs). The system is placed on a vibration isolation table to minimize external noise. All the experiments are performed at room temperature, using indentation depth-control mode [259].

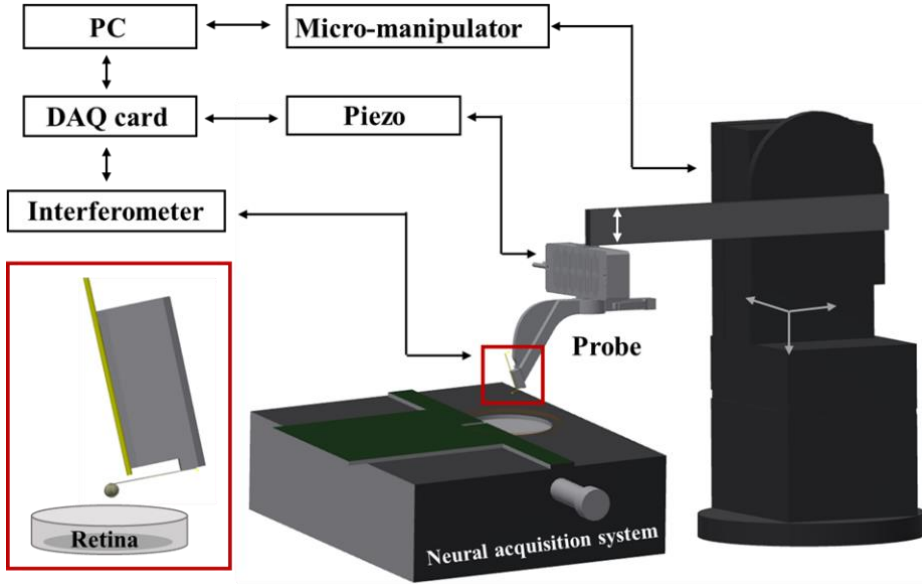


**Figure 6.1 | Schematic view of the setup**

A ferrule-top probe is equipped with an optical fiber for interferometric readout of the cantilever and with a spherical tip to indent the sample. The probe is mounted on the Z-piezoelectric actuator, which is solidly attached to an XYZ manipulator. Retina samples are submerged in the perfusion chamber and fixed on HD-MEAs based on a high-impedance CMOS chip.

### 6.2.3 Indentation protocol for mechanical characterization

To probe the viscoelasticity of retina samples, depth-controlled frequency sweep measurements have been performed at small oscillation amplitude and different frequencies. Typically, dynamic indentations (maps) consisted of a loading part up to 15 or 20  $\mu\text{m}$  with 2  $\mu\text{m/s}$  indentation speed, followed by a 10 s stress relaxation period and a series of small sinusoidal oscillations of 0.3  $\mu\text{m}$  at three different frequencies: 0.1, 1 and 10 Hz. For indentation maps, we selected cantilevers with  $\sim 0.45\text{ N/m}$  spring constant, calibrated according to [260], and a bead radius of 57 and 73  $\mu\text{m}$ , measured via an optical microscope. Indentations were performed in an arbitrary region of the retina in parallel lines, with a distance between two adjacent locations of 50  $\mu\text{m}$ , which assured that the deformed areas do not overlap. The apparent storage and loss moduli were calculated as:

$$K' = \frac{E'}{1-\nu^2} = \frac{F_0}{h_0} \cos(\varphi) \frac{\sqrt{\pi}}{2} \frac{1}{\sqrt{A}} \quad (1)$$

$$K'' = \frac{E''}{1-\nu^2} = \frac{F_0}{h_0} \sin(\varphi) \frac{\sqrt{\pi}}{2} \frac{1}{\sqrt{A}} \quad (2)$$

where  $E'$  and  $E''$  are the storage and the loss modulus, respectively,  $F_0$  is the amplitude of the oscillatory load,  $h_0$  is the amplitude of the oscillatory-indentation,  $\nu$  is the

Poisson's ratio of compressibility (assumed to be equal to 0.5, which corresponds to an incompressible material),  $\varphi$  is the phase lag between the recorded indentation and load oscillations, and  $A = \pi a^2$  is the contact area between the sphere and the sample. The contact radius is estimated as  $a = \sqrt{Rh}$  where  $R$  is the radius of the sphere and  $h$  is the indentation depth. For the final data analysis, three maps of two retinæ were used. Normality of data distribution was tested with the Shapiro-Wilk test. Since the majority of the dataset were non-normally distributed, the non-parametric Kruskal-Wallis ANOVA test was used to compare data samples. All statistical analyses were performed with Statistics and Machine Learning Toolbox (version 2018a, The Mathworks, Natick, MA, USA).

## 6

#### 6.2.4 Retina electrophysiology

Twelve hours dark-adapted male mice (6 weeks old C57BL/6) were barely anesthetized with CO<sub>2</sub> and subsequently killed by cervical dislocation. As described in (Hilgen et al., 2017a; Maccione et al., 2014), after eyeballs enucleation, the retina was extracted by accurately removing all the surrounding tissues such as the cornea, crystalline, sclera and vitreous. Once isolated, the retina was faced down onto a pre-conditioned HD-MEAs (its reservoir was filled with Neurobasal for 2 hours at 37°) putting the retinal ganglion layer in contact with the surface of the electrodes and leaving the photoreceptor layer exposed to the indentation probe. A perfusion line, supplied by a peristaltic pump (~1 ml/min), ensured a constant flow of a media composed by AMES's medium (Sigma - Merck KGaA, Darmstadt, Germany) with 1.9g/L of sodium bicarbonate equilibrated with carboxigen (95% O<sub>2</sub> and 5% CO<sub>2</sub>). Recordings of retinal ganglion cells extracellular activities were acquired through the BioCam4096 platform with 4096 Arena chips (3Brain AG, Wädenswil, Switzerland), which consist of a 64x64 grid of square microelectrodes (21  $\mu$  m x 21  $\mu$  m, pitch 42  $\mu$  m) covering an area of 2.67 mm x 2.67 mm (HD-MEAs). The raw extracellular traces, sampled at 7.1 kHz/electrodes, were digitized at 12-bit resolution and stored for off-line analysis upon application of a low-pass filter (3.5 kHz) using Brainwave software. Spikes in extracellular traces were detected and sorted exploiting the redundant information of spatially adjacent electrodes [96]. Only single units exhibiting at least 0.1 spike/sec were considered for subsequent analysis. Upon application of this filtering procedure, the resulting dataset consists of multiple hundreds of single units per single retina.

#### 6.2.5 Experimental protocol for electrophysiological characterization

To correlate the effects induced by the mechanical stimulation of the photoreceptor layer with the spiking activity of retinal ganglion cells acquired with HD-MEAs, two pieces of information were essential: the time-window of mechanical stimulation and an

estimation of the indentation position with respect to the electrode grid. To identify the stimulation time-window, we used a Raspberry Pi device (Raspberry Pi Foundation) that, through custom python algorithms, memorizes the timing of the triggers generated by the indenter at the beginning and the end of the stimulation phase relative to the starting point of the HD-MEAs recording. Next, this information was incorporated into the spike-trains allowing an a-posteriori alignment of the indentation time-interval within the recorded spiking activity. To navigate the indentation probe onto the electrode matrix and estimate the indentation position, we shined a far-red light onto the retina for less than 5s. This procedure triggers light-induced signal saturation in all the electrodes of the HD-MEAs except for those located in the region shadowed by the indentation probe (see figure 6.2 A). Upon selecting through visual inspection, the time-frame at which the difference between non-saturating and saturating electrodes was maximally noticeable, we manually detected the contour of the indentation probe. Next, we estimated the indentation position as the electrode corresponding to the center of the indentation sphere located on the indentation probe.

To obtain a direct readout of electrical signaling upon mechanical deformation, we used large spheres ( $\sim 250\ \mu\text{m}$  beads), and we probed specific local regions of the retina at different amplitudes and indentation depths. Each sample was probed through three controlled indentation protocols, described in figure 6.2, that differed in the dynamic of the indentation over time. Specifically, once the probe reached the desired depth, we tested the retinal mechanical and electrophysiological response to a steady and continuous displacement (figure 6.2 B) and small (figure 6.2 C,  $h_o = 1\ \mu\text{m}$ ) or mild (figure 6.2 D,  $h_o = 3\ \mu\text{m}$ ) oscillations amplitude at 0.1 Hz. As summarized in figure 2B-D, these protocols were performed at depths ranging from 10 to 60  $\mu\text{m}$  for each experimental session and were interleaved with a minimum of two minutes of basal recording to avoid the application of prolonged stresses to the retinal tissue. Prior to indentation protocols, the spontaneous activity of the retinal ganglion cells was recorded for five minutes to obtain a baseline reference of retinal activity and, after that, the response of RGCs has been visually stimulated with a sequence of black and white flashes (see ON-OFF classification section) to probe their preferential response. Next, the indentation probe approaches the tissue, and its position was estimated.

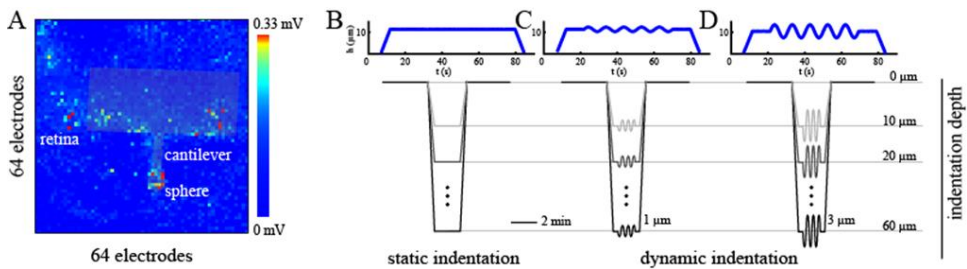




### Figure 6.2 | Schematic view of the setup

The contour of the indentation probe was detected by looking at non-saturating channels upon far-red light stimulation. (B), (C), and (D): Mechanical stimulation profile as a function of time for static indentation (no frequency sweep, B), small oscillation amplitude ( $h_0 = 1 \mu\text{m}$ , C), and mild oscillation amplitude ( $h_0 = 3 \mu\text{m}$ , D) types of stimuli. Exemplary mechanical profiles are plotted in blue for an indentation depth of  $10 \mu\text{m}$ . Mechanical indentations were then performed at progressively deeper levels ranging from  $10$  to  $60 \mu\text{m}$  from the contact point.

## 6.2.6 Data Analysis

Before each indentation phase, we recorded 120s of basal spiking activity, which we used to determine the reference firing regime of RGCs before mechanical stimulation. For both basal and indentation phases, the mean firing rate of each single RGCs was computed by quantifying the number of spikes occurring in a 2s time-interval sliding over the recording period with steps of 100ms. Next, the mean firing rate was normalized through z-scoring to ensure a comparison over standardized firing rates. The correlation matrix between the normalized firing rate was then computed for both the basal and indentation phases.

## 6.2.7 Clustering of similar spiking activity

To highlight the modulatory effects exerted by mechanical indentation onto retinal ganglion cells spiking activities, we clustered the firing rate of single RGCs according to their variations over time. A standard dendrogram clustering procedure was applied to the normalized firing rate (computed every 10ms over a 2s sliding window) of the indentation phase using the absolute value of Pearson correlation as similarity metric [261]. We then selected an optimal number of clusters within the range 4 to 60 through maximization of the silhouette score [262]. Next, we reordered the correlation matrix of the basal phase according to the clustering obtained during the indentation phase to prove that the clustered RGCs were not correlated during the basal time-window and thus that correlations in RGCs spiking activity arise from mechanical stimulation.

## 6.2.8 Classification of ON\_OFF RGC cell types

To assess whether subpopulations of retinal ganglion cells are most sensitive to the effects of mechanical stimulation, we first had to identify functional RGC cell types based on their preferential responses to visual stimuli. To do so, at the beginning of the experiment, we presented to the retina a sequence of alternating white/black full-field flashes ( $0.0$ - $0.2 \text{ cd/m}^2$ ) that allow characterizing the RGCs spiking response properties. To distinguish between ON, OFF and ON-OFF RGCs we computed the Bias Index (BI) as  $(A_w - A_b) / (A_w + A_b)$ , where  $A_w$  and  $A_b$  are the amplitudes of the peak response, with respect to the basal level of activity, to the white and black flashes, respectively [263]. RGCs were

marked ON if  $BI > 0.3$ , OFF if  $BI < -0.3$ , and ON-OFF otherwise. Cells whose peak firing rate was one standard deviation below the mean basal firing rate were assigned to the non-classified cluster (NC).

### 6.2.9 Decision Tree Classifier

To disentangle crucial physical and electrophysiological predictors that can determine the modulation of spontaneous spiking activity upon mechanical stimulation, we applied a Decision Tree Classifier [264] on all trials. This machine learning model learns how to classify binary outcomes as successful and unsuccessful indentations by building a tree of if-then-else relations among the predictors provided. In our scenario, the predictors are: the contact area of the indentation probe, the strain, the pressure, the depth of the indentation, the local density of RGCs below the indentation point ( $d_5$ , number of cells within five electrode distance), and the local firing rate of RGCs point below the indentation point in basal condition ( $r_5$ , average over cells within five electrode distance). Once the decision tree classifier is trained, the importance of each feature is computed as the normalized Gini importance. To ensure unbiased results, we obtained averaged values by repeating the procedure 1000 times with different initial conditions.

6

## 6.3 Results

The primary purpose of this study was to design a new experimental setup able to combine a high-density multi-electrode array with ferrule top indentation to provide insights about electromechanical coupling in retina tissue.

### 6.3.1 Characterization of Mechanical Properties of the retina tissue

To confirm that ferrule-top depth-controlled dynamic indentation is capable of capturing the viscoelastic nature of the retina even when combined with HD-MEAs, we performed three indentation maps on two different samples. In figure 6.3, we report the dynamic response of the retina, in terms of apparent storage and loss moduli over the frequency range of 0.1-10 Hz. The frequency sweep data show a stiffening of the tissue with increasing indentation frequency for both the apparent loss and storage moduli. For instance, the averaged storage modulus, pooled from all the indented locations, increases from 0.7 kPa at 0.1 Hz to 1.7 kPa at 10 Hz.

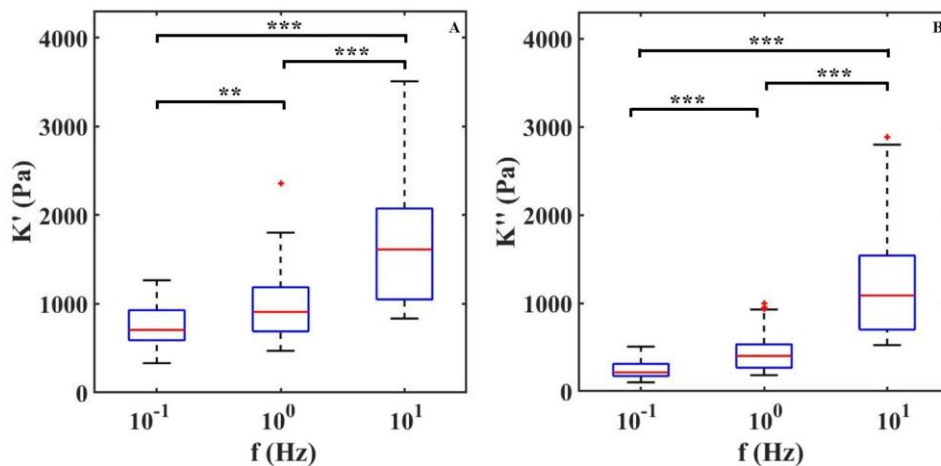


**Figure 6.3 | Mechanical properties of the retina.**

Apparent storage ( $K'$ ) and loss ( $K''$ ) moduli plotted as a function of indentation frequency. Each column contains data of two retinæ and around 30 measurements per frequency. The outliers are plotted individually using the '+' symbol (red).

With the dynamic indentation, one can define the ratio between the loss and storage modulus, known as loss tangent,  $\tan(\Phi)$ , which provides the relation between viscous and elastic components.

$$\tan(\Phi) = \frac{E''}{E'} \quad (3)$$

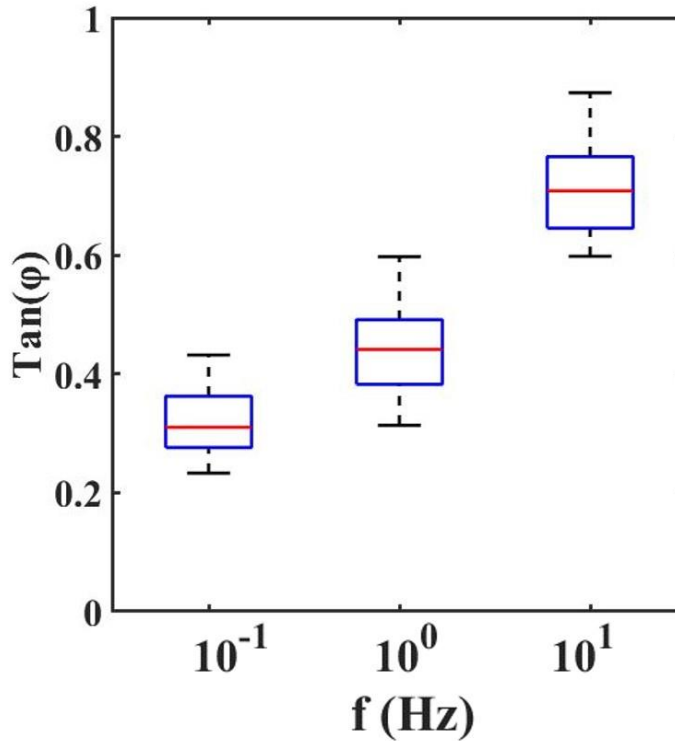


**Figure 6.4 | Loss tangent values**

Loss Tangent: the tangent of the phase angle between load and indentation as a function of frequencies.

### 6.3.2 Mechanical indentation affects the spontaneous activity of retinal ganglion cells

After the characterization of the mechanical properties of the retinal tissue, we investigated the electrophysiological response, signaled through the spiking activity of retinal ganglion cells (RGCs), to mechanical stimulation. The overall goal of this section is to validate the potentials of combining sub-micrometer-accurate indentation to HD-MEAs to investigate the effects of mechanical stimulation in neuronal tissue. As stressed above, we simultaneously recorded the spiking activity of hundreds of RGCs with an HD-MEAs system while locally indenting the photoreceptor layer (see figure 6.5) to examine the RGCs firing rate spatio-temporal distribution. Next, after identifying the responding RGCs, we checked whether the transduction of mechanical cues was a prerogative of a specific subtype of RGCs, namely ON, OFF, or ON-OFF cells.

### 6.3.3 HD-MEAS recordings

The HD-MEAs can sample the bioelectrical activity of hundreds of RGCs over a large

portion of tissue. Upon application of a localized mechanical stroke with the spherical tip of the indentation probe, we focused our attention on possible firing-rate modulations evoked at the pan-retinal scale. Although kept in a dark condition, RGCs are always active, and their spiking activity does not exhibit particular spatio-temporal structures. However, depending on the firing patterns elicited in response to an alternating sequence of black and white flashes that visually stimulate the photoreceptor layer, ON, OFF, and ON-OFF RGCs can be distinguished. RGCs not ascribable to any of the mentioned types were grouped in a fourth class (NC).

We conducted experiments on seven retinæ by indenting the photoreceptor layer at four depth (10-20-30-60  $\mu\text{m}$ ) and in three retinæ we were able to detect mechanically induced responses in the spiking activity of >100 RGCs over >300 RGCs considered for each retina, see table 6.1.

6

<i>Retina ID</i>	<i>Amplitude (<math>\mu\text{m}</math>)</i>	<i>Depth (<math>\mu\text{m}</math>)</i>	<i>Frequency (Hz)</i>	<i>Max Load (<math>\mu\text{N}</math>)</i>	<i># of RGCs activated</i>	<i>Total RGCs</i>
R1	/	30	/	5	154	346
	1	30	0.1	1.5	145	346
R2	/	20	/	0.3	102	425
R3	/	60	/	34	129	308

**Table 6.1 | Summary of mechanical protocols that determined a variation in the firing rate in retinal ganglion cells.**

All the tested mechanical stimulation conditions with an indication of successful/unsuccessful induced responses are included in Figure 6.8.

Mechanical stimulation evokes in a subset of RGCs a plethora of different responses, as shown in figure 5. Heterogeneous responses include, but are not limited to, an increase in firing rate at the onset (figure 6.5 A), at the offset (figure 6.5 B), or both (figure 6.5 C) of the stimulation time-interval. Moreover, we observed a drop in the firing rate at onset (figure 6.5 D) or offset (figure 6.5 E). Finally, while we recorded a few RGCs with rebounding activities (figure 6.5 F), a large fraction of RGCs was insensitive to the mechanical stimulation (figure 6.5 G).

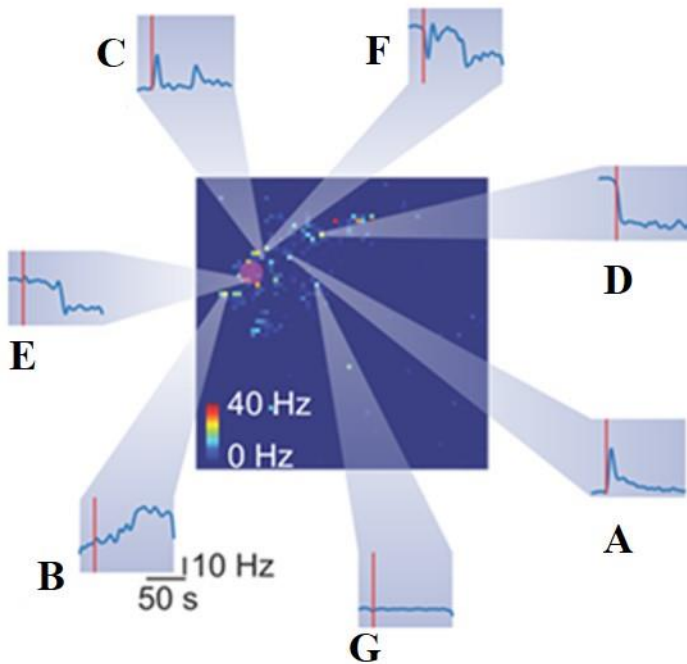


**Figure 6.5 | Heterogeneous spiking activity response of retinal ganglion cells to mechanical stimulation**

The big square represents the retina spiking activity collected from the HD-MEAs. Each pixel color code the mean firing rate of the RGC recorded from a specific electrode. The red rounded shaded area highlight the indentation area. Each inset (from A to G) reports the temporal spiking dynamics of different RGCs in response to the same mechanical stimulation (red vertical line represents the stimulation time).

#### 6.3.4 Mechanical stimulation determine correlated spiking activity

To elucidate and describe the effects of a localized mechanical stimulation at the pan-retinal scale, we clustered together RGCs whose spiking activity was correlated or anti-correlated during the indentation time-window (figure 6.6 A). Interestingly, this approach reveals the presence of correlated RGCs clusters during the indentation time-window that exhibit the following features. First, their arrangement is not preserved in the basal recording, i.e., the time interval preceding the stimulation onset, where the within-cluster correlation sharply drops (figure 6.6 B). Second, the clusters of correlated RGCs are well-segregated in space and located in the surrounding of the indentation spot up to a millimeter distance (figure 6.6 C). Third, as shown in the raster plot of figure 6.6 D, mechanically evoked responses resemble the ones obtained with visual stimulation despite their significantly longer time-scale of activation (tenths of seconds instead of tenths milliseconds, respectively). Fourth, the RGCs spiking activity within the clusters

detected is mainly characterized by a prolonged increase in their firing rate lasting a few seconds (see figure 6.6 E). Nevertheless, inhibition was observed in a very few RGCs, as we will discuss more in details in the next paragraph. Similarly to the ON-OFF classification obtained in response to visual stimuli, we could distinguish between RGCs that activated only to pressure onset (reddish clusters), at pressure release (greenish clusters) or to both (blueish clusters). Fifth, these response delays are consistent with the relative position of RGCs from the indentation spot (in figure 6C colored dots represents and highlights the RGCs that showed a response modulated by the mechanical indentation vice-versa the white dots). These features were observed in the three retinas who effectively responded to the mechanical stimulation, (see figure S 6.1) whereas the spiking activity of the remaining retinas during the mechanical stimulation time interval remained indistinguishable from their basal. Despite these unsuccessful trials (see later for dedicated discussion), our results still indicate that the retina can convey information about the physical world within the RGCs spike trains and that mechanical stimulation can perturb the spiking activity over extended regions of the retina.

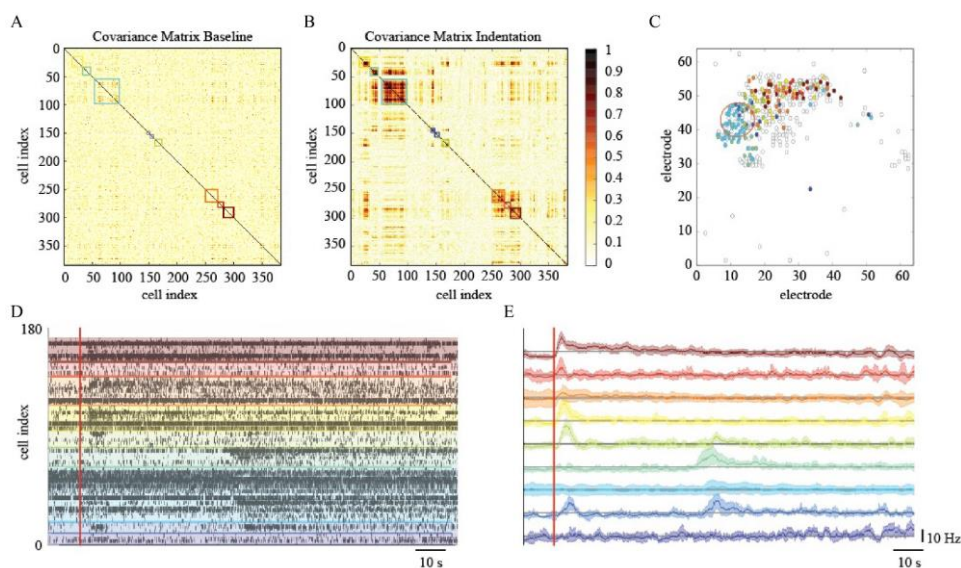


**Figure 6.6 | Effects of localized mechanical stimulation onto retinal ganglion cells (RGCs) spontaneous spiking activity**

(A) Reordered correlation matrix revealing clusters of correlated RGCs during the indentation time interval (color-coded blocks). (B) Correlation matrix of the basal activity reordered according to the clustering in (A) reveals a different arrangement of correlations. (C) Position of RGCs modulated (colored dot) or not (white dot) by the mechanical stimulation. (D) Raster plot of the RGCs spiking activity within each cluster (separated by colored lines) during the indentation time interval (red vertical line, onset). (E) Z-scored RGCs firing rate during indentation (solid line, mean; shaded area, s.e.m.). Color codes for cluster membership in all panels.

### 6.3.5 Processing of mechanical vs. visual sensory inputs

Although the time-scales of mechanically evoked responses are not comparable to visual ones, we tested whether the functional subpopulation of RGCs, namely ON-/OFF- or ON-OFF-type, were equally modulated. We functionally classified the RGCs within the relevant clusters detected by quantifying the bias index of the spiking response to white and black full-field visual stimuli (see methods). Interestingly, in our experimental conditions of scotopic luminance, the OFF-RGCs response dominates over ON-RGCs response in amplitude while non-classified units (NC) were barely sensitive to visual stimuli with a minor, non-significant, preference to white flashes (NC-type). To assess whether a subpopulation would be primarily involved in conveying mechanical information, we computed the average composition of ON, OFF, ON-OFF and NC-type RGCs in the clusters associated ('responsive to stimuli') or not ('unresponsive to stimuli') to any mechanically evoked response (figure 6.7 A). While the cell-type distribution in 'unresponsive to stimuli' clusters was fairly similar across the retinae, the 'responsive to stimuli' clusters consist of at least 15% more ON-RGCs than the 'unresponsive to stimuli' counterparts. Thus, the different cell-type distribution indicates a fundamental contribution of the ON information pathway compared to the others considered in our analysis. Given that our clustering metric is sensitive to both correlated and anti-correlated activities, we investigated whether by further dividing the 'responsive to stimuli' clusters according to the ON-OFF classification of RGCs we could reveal additional response features to the mechanical stimuli. This was performed by comparing the firing rate during mechanical (figure 6.7 B) stimulation.

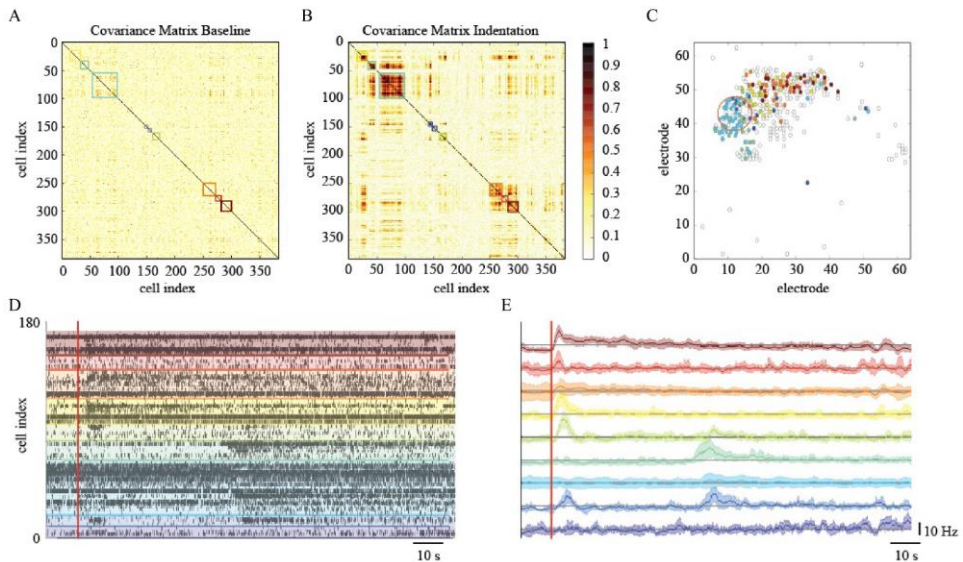


**Figure 6.7 | ON-OFF classification of mechanically evoked spiking activities.**



(A) Distribution of ON, ON-OFF, OFF and NC RGCs in clusters associated ('responsive to stimuli') or not ('unresponsive to stimuli') to mechanically evoked responses. (B) The top four clusters of figure 6.6 E were further decomposed according to cell type.

To investigate what are the most crucial parameters that can give rise to a modulation of the spontaneous activity of RGCs upon mechanical stimulation we organized our data with a machine learning approach. Figure 6.8 A shows a pairwise scatter matrix of the electrophysiological and physical parameters (predictors) involved in the indentation experiments that shows for each condition whether the mechanical stimulation gave rise to a modulation in the firing activity of RGCs comparable to the illustrative example of figure 6.8A (successful, red dot) or the mechanical stimulation did not affect the retinal baseline firing (unsuccessful, blue dots). Based on these observations, we trained a decision tree to learn a set of if-then-else rules arranged in a tree-like fashion that splits the parameter space into successful and unsuccessful regions, given the values of predictors. After training, we can interpret what are the rules that the model has learned to identify successful and unsuccessful trials by looking at the structure of the tree. Indeed, by computing how often a predictor is used in the tree to split the data and how much the predictor decreases the impurity (i.e. the fraction of successful and unsuccessful trials before and after the split) we can estimate how important such a feature is. As shown in figure 6.8B, according to the decision tree model, the local density of RGCs ( $d_5$ ), the pressure applied (pressure), and the local firing rate ( $r_5$ ) are the ones that most effectively provide information on whether or not a given indentation can induce modulations in the spontaneous firing rate of RGCs.

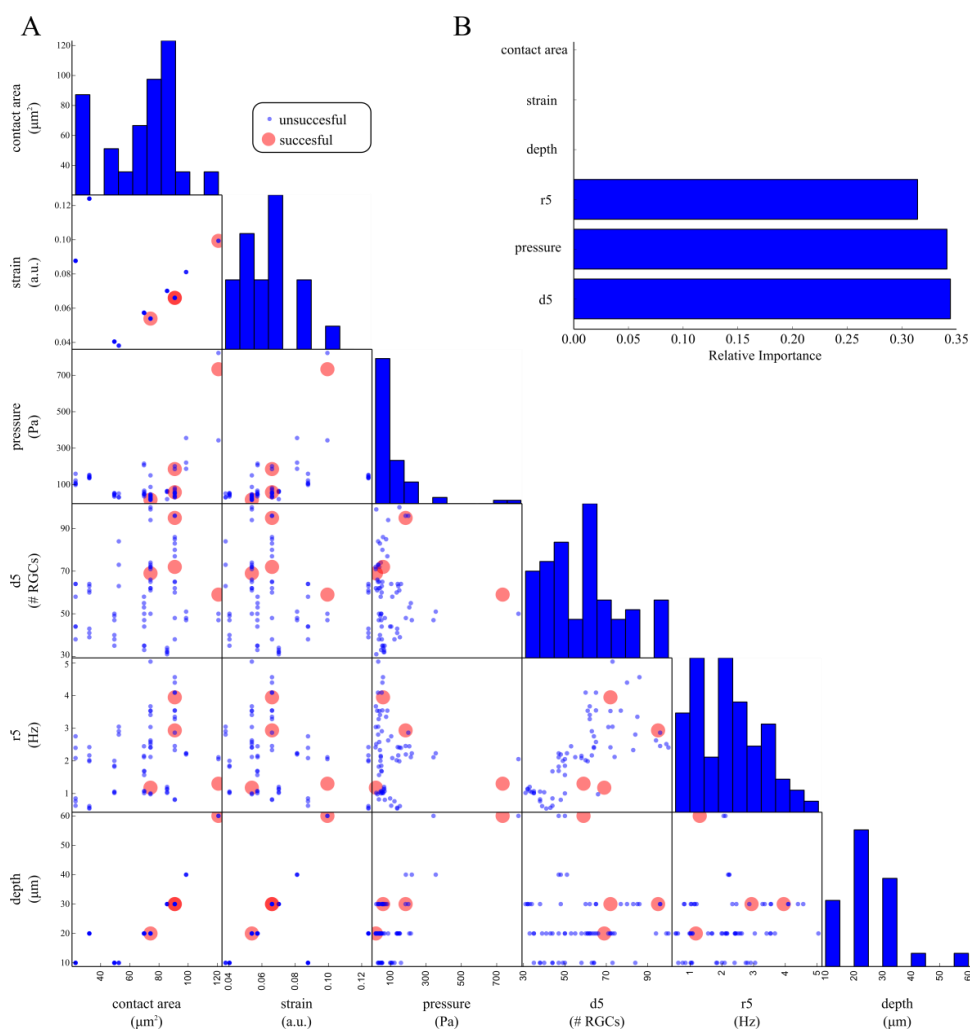


**Figure 6.8 | Determinants underlying the physiological response upon indentation.**

(A) Off-diagonal: pair-wise scatter plots of physical (contact area, strain, pressure, depth) and electrophysiological (d5: average RGC density within five electrodes, r5: average RGC firing rate within five electrodes) predictors of an electrophysiological response to mechanical stimulation. Each scatter plot depicts whether a mechanical indentation induced modulation in the RGC firing rate (successful trial, red dots) or not (unsuccessful trial, blue dots) as a function of a pair of predictors. Diagonal: histogram of the distribution of each predictor. (B) Relative importance of physical and electrophysiological features in a decision tree model trained to predict successful and unsuccessful trials based on the data in (A). The trained model suggests that local density (d5), pressure, and local firing rate (r5) are the most effective predictors used by the decision tree model to split the successful from the unsuccessful trials.

## 6.4 Discussion

In this work, we developed an experimental platform combining a depth-controlled force transducer with a planar high-density multi-electrode array (HD-MEAs) device. This platform allows probing contact force effects on the activity of brain circuits determined by large-scale neuronal activity recordings. To demonstrate this technology, we investigated the effects of mechanical stimuli on the electrophysiological response to visual stimuli of explanted mice retinæ. We simultaneously recorded the activity of many retinal ganglion cells (RGCs), and we investigated the effects on the light responses of three RGC subtypes, namely ON, OFF and ON-OFF RGCs.

By performing the first depth-controlled frequency-domain indentation tests on mouse retinæ ever reported in the literature, we could observe that, in the 0.1-10 Hz range, both apparent storage and loss moduli increase with indentation frequency — a viscoelastic behavior that was previously observed as a stress relaxation and in bulk rheology experiments [265,266]. A direct comparison with other viscoelastic measurements is unfortunately not possible, because the latter have been either performed on a different kind of samples (human or pig retina) or at nano-scale (single cells, or cell monolayers), which give rise to very different results. Quantitatively, it is interesting to note that, in terms of apparent storage modulus at low frequencies, our findings are in good agreement with Franze et al. [257] even if the measurements are performed under different indentation protocols. Moreover, figure 6.3 shows that both  $K'$  and  $K''$  increase with increasing frequency of deformation in a manner consistent with numerous previous studies on biological tissues [267–270].

However, the high value of  $\tan(\Phi)$ , suggests that it is crucial to mechanically characterize the retina by considering both the elastic and viscous contribution. Even if the viscosity is not negligible, the predominance of the elastic behavior of the retina compared to its viscous one is confirmed. From the values reported in Figure 6.4, it is possible to observe slight variations in local viscoelasticity; however, our findings, obtained by scanning the surface of the sample with 50  $\mu\text{m}$  spatial resolution are not sufficient to evaluate the local heterogeneity of the tissues. Therefore, in the future, to accurately investigate the relationship between the inner retinal morphological structure and its mechanical heterogeneity, one should perform high-resolution viscoelasticity maps.

Through the combination of HD-MEAs system with micro-indentation, we studied the modulation of RGCs spiking activity of explanted mice retinas in response to mechanical micro-stimulations of their photoreceptor layer. Our preliminary findings suggest that it is possible to determine a correlation between the mechanical stimulation of the retina and its electrical signaling. Specifically, we observe an increased firing rate during the indentation time-interval mostly imputable to ON-RGC. In agreement with Rountree et al. [255], we found that the mechanical stimulation of explanted retinas elicits spatially localized retinal responses similar to light-evoked one, under specific mechanical

condition - indentation depth  $> 20 \mu\text{m}$  and indentation strain  $\epsilon > 0.05$  [172]. However, Rountree et al. reported that the mean pressure able to mechanically stimulate the retina is 0.69 kPa, whilst in our depth controlled experiments we found that the minimum pressure to mechanically stimulate the retina is of only 0.02 kPa, possibly meaning that the indentation depth and the sphere radius are the most crucial parameters that can give rise to a light-evoked response. Our experimental data show that the retinal circuit can convey information on mechanical stimuli by modulating RGCs activity, and thus the same retinal circuit's output of encoded visual stimuli. Recordings of mechanically induced RGCs response show a longer delay from stimuli (tens of seconds) compared to delays of light-evoked visual responses (milliseconds). This response latency could be due to the slow indentation profiles used in our measurements or to the fact that mechanical stroke is focused on the photoreceptor layer and the stress propagates in a certain time scale until the ganglion cell layers. In this context, in the future, it would be interesting to tweak the indentation profile (e.g., indentation speed and oscillation amplitude and frequency) in order to modulate and to accurately study the propagation of the mechanically evoked response in the tissue.

Given that our results indicate that mechanical stimuli are likely encoded in RGCs activity, another intriguing possibility, instead, is that RGCs convey to downstream areas multiple sensory information [249], and in particular intraocular pressure [271]. In this scenario, different messages might be conveyed through the same pathway by using distinct time-scales as information carriers.

Interestingly, we also observed that the mechanically evoked responses are spatially distributed in the surrounding of the indentation location and not only under the stimulated point, possibly indicating a slow horizontal propagation of the mechanically evoked bioelectrical perturbation across the retinal tissue. This result can be consistent with the propagation of calcium waves in Muller's cells triggered by pressure signals [272]. Such calcium waves, indeed, can impact retinal ganglion cell spiking activity by modulating their response to visual stimulation [273]. In addition, the modulation of basal firing rate we observed in this work is consistent with the time-scale of Muller's cells calcium waves [253,272].

However, the biological origin of the modulation in firing rate observed in this work is not limited to activation of Muller's cells but may be attributed to other mechanisms acting together, as direct modulation of photoreceptors and horizontal cells [244].

Ultimately, our findings could possibly cast a shadow on the effects of using weights (e.g. metal anchors) usually employed in electrophysiological experiments on explanted retinas. Indeed, in the light of what was demonstrated in this work, we cannot exclude the presence of distortion in the retinal signal induced by the constant pressure produced by external weight commonly used during recording sessions for keeping the tissue attached to the multi-electrode array surface. Some possible side-effects have been already reported in literature [274] and need to be further investigated in order to

disentangle whether these differences are related to an electrode-tissue coupling issue (i.e. collected signals vary depending on the anchor weight because the distance between the electrodes and the RGCs is different) or if the constant force applied on top of the retina interferes with the visual processing pathway consequently modifying the RGCs output.

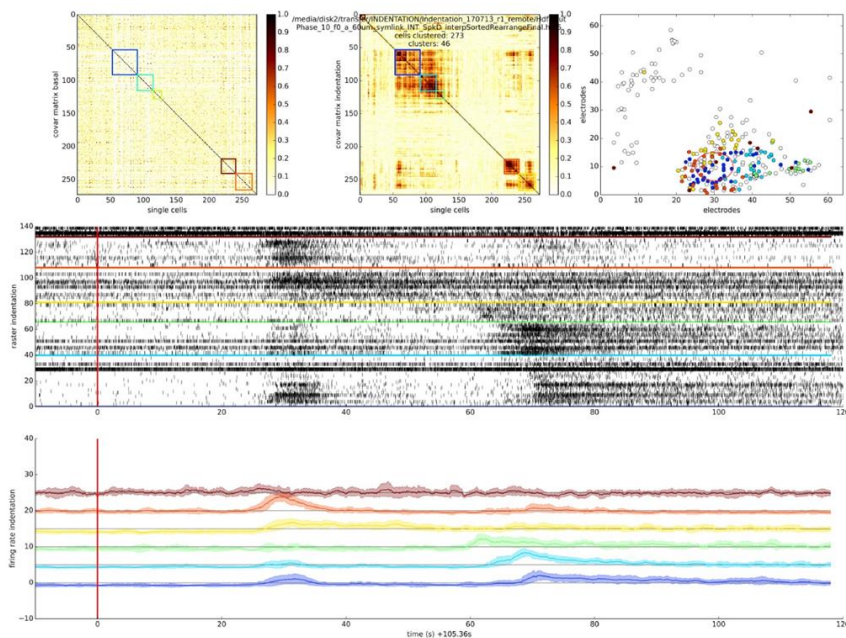
Moreover, it is worth mentioning that several factors could explain the unsuccessful induced responses. First of all, our intent was mainly to explore whether the retina could respond to mild mechanical stimuli to avoid second-order effects mainly due to retinal damage. As a consequence, we decided to deliver shallow mechanical stimuli, and we expected to observe more unsuccessful than successful trials. A second major source of inter-trial variability is the location of the indentation. Specifically, we targeted areas of the retina in which the coupling with the MEA was optimal. However, such a heuristic criterion may lead to the stimulation of retina patches that are, per se, functionally, and structurally different locally. Moreover, we were not able to precisely identify in which region of the sample we were indenting (center vs. periphery, medial vs. lateral, frontal vs. nasal). Of course, the electrophysiological response of the retina can differ between those regions, and it will be of utmost interest, to investigate in the future if, for example, the unsuccessful cases are related to the different regions of the retina. Third, one of the main challenges of performing these experiments on live tissue is related to the necessity to keep the tissue stable and alive over the course of the measurements. The entire stimulation protocol takes around 20 minutes per location. Therefore those time scales do not allow us to map the entire retina in vivo and long-timescale could compromise the vitality of the tissue inducing inter and intraretinal variability. Another factor of variability between the retinae could be related to the preparation of the biological sample itself and the immobilization of the sample on the multi-electrode array surface. The adhesion of the retina onto the multi-electrode array surface is extremely important in order to avoid stimulating the floating tissue rather than probing the tissue stiffness.

In conclusion, we have introduced a new technique that allows the analysis of the electrical signals cascade occurring through neuronal networks under controlled mechanical stimulation and that is able to reliably measure the viscoelastic properties of soft biological samples. In the future, the combination of HD-MEA system with micro-indentation could offer a unique opportunity to investigate the effects of mechanical stimulation on the electrophysiological activity of neuronal tissue also at single-cell resolution and over a wide portion of biological tissue such as stem cells [229–232] heart [233–235], lungs [236], muscle [275,276] and skin [277]. Finally, since mechanical stress can modulate physiological processes at the molecular and cellular level, we expect that this tool will support a significant step forward in gaining new insights on the relationship between altered mechanosensitive signaling, stiffness, and pathologies.

## Acknowledgments

We thank the anonymous reviewer for helping us in improving the manuscript by raising concerns on some of the results that lead to bug fixes in the code of image generation. MM acknowledges E. Paardekam for his technical support and N. Antonovaite for fruitful discussions. DL and FB acknowledge M. Nanni and G. Pruzzo for their technical support and the European project RENVISION (FP7-ICT-2011-g) grant agreement no. 600847 for developing the CMOS platform for acute retinal recordings.

## 6.5 Supplementary figures



**Supplementary figure 6.5.1 | Effects of localized mechanical stimulation onto retinal ganglion cells (RGCs) spontaneous spiking activity.**

(A) Reordered correlation matrix revealing clusters of correlated RGCs during the indentation time interval (color-coded blocks). (B) Correlation matrix of the basal activity reordered according to the clustering in (A) reveals a different arrangement of correlations. (C) Position of RGCs modulated (colored dot) or not (white dot) by the mechanical stimulation. (D) Raster plot of the RGCs spiking activity within each cluster (separated by colored lines) during the indentation time interval (red vertical line, onset). (E) Z-scored RGCs firing rate during indentation (solid line, mean; shaded area, s.e.m.). Color codes for cluster membership in all panels.



# Chapter 7 |

## Summary and Conclusion

### **Abstract**

Biophysics has the crucial task of unraveling the mechanisms governing the biological processes in living organisms, combining the fields of Biology, Engineering, and Physics. Understanding the properties of biologic tissue is a complex task; therefore, biophysicists need to approach the problem by looking at different length scales, and by observing life from different perspectives. As a point in case, adding optical and electrical information, to tissue mechanical properties, could provide a significant step forward for a better understanding of the tissue-structure interaction. In this thesis, an effort was made to combine micro-indentation with optical imaging and electrophysiology to open new avenues in the field of Biophysics.



The summary below provides a concise overview of the major finding presented.

In **Chapter 1** I have given a general introduction to the topic of the thesis. I introduce the field of tissue mechanics, and I overviewed the state of the art of mechanical microindentation technique with particular remark to ferrule top technology. I also gave a brief overview of the Optical Coherence Tomography and its common-path modality. I finally review the field of electrophysiology, emphasizing the use of High-Density Micro Electrode Array for neuronal tissues.

**Chapter 2** introduce the combination of OCT images and microindentation tests as a new tool able to perform 3D scanning of the sample with high resolution while simultaneously mapping the viscoelastic properties of tissues locally. I applied the technique to fixed embryos, to show its capabilities: (1) local measurement of viscoelasticity, (2) 3D cross-sectional imaging in real-time, and (3) the ability to identify correlations between tissue morphology and tissue viscoelasticity. Three powerful features that make this new tool suitable for a wide variety of biological samples and therefore, of great interest in several fields such as biology, biomaterial science, and tissue engineering. Moreover, I describe the ability of this method to accurately capture variations in stiffness due to different sample structures or treatment, to reliably measure the viscoelastic and non-linear properties of heterogeneous materials, and simultaneously investigate sample morphology.

After the introduction of the depth-resolved viscoelasticity +OCT method, I described in **Chapter 3** an application for in vivo biological tissue. Here, live tissue is analyzed and scanned in real-time. The chapter provides insight into unanswered questions of crucial importance for the field of biological development. As a point in case, I showed how viscoelasticity is related to the maturation of the chicken embryo. The findings indicate that the notochord and neural plate quickly develop a high stiffness, supporting the idea that the notochord is not only an organizer for chemical signaling but also acts as an 'embryonic spine' that secures the mechanical integrity of the early embryo. Furthermore, by performing depth-controlled dynamic indentation, we demonstrate that the non-linear mechanical behavior of the embryonic tissue differs based on the development of the epithelial tissues: more mature and more extracellular matrix tissue is more elastic and less viscous. Even if I showed that it is possible to use OCT in combination with microindentation for in vivo tissue application, this technology has the main limitation related to the fact that the sample needs to be accessible from both sides.

Depth-resolved viscoelasticity +OCT method permits high experimental throughput on many soft and thin samples. However, due to the experimental design, it would be impossible to apply this technique to a thick specimen. Therefore, to overcome those limitations, I described in **Chapter 4** in detail how to fabricate a micrometer lens attached at its distal end to acquire an OCT scan. The capability of the micrometer lens has been demonstrated in air and in liquid environment and on a mouse brain thin slice as well as

on human finger. Here, I have thus taken a major step forward in the fabrication of ultrathin optical probes for in vivo imaging. Our approach enables the development of new OCT systems for minimally invasive applications and may be used in numerous other imaging technique where small diameter optical probes might be required.

In **Chapter 5** I used the OCT optical fiber lens design of chapter 4 to implement a new optomechanical probe that allows one to compress a sample with an indentation stroke and simultaneously observe how the subsurface layers deform under an external load. In this chapter, I describe the fabrication steps of an optical fiber array sensor for OCT imaging combined with an indentation probe. This approach paves the way for the development of new hybrid tools for material analysis that could enable researchers to explore the field of material analysis and tissue engineering by simultaneously recording two pieces of information that would be neglected by choosing between either in depth-imaging or indentation. While the manufacturing processes are challenging, the sensor has several capabilities and advantages in comparison to other techniques. Therefore, further investigation of the self-assembly process and improvement of data processing should be explored.

In **Chapter 6**, I propose an experimental platform combining micro-indentation capabilities with high-density multi-electrode array (HD-MEAs) recordings. This allows one to precisely monitor over a wide portion of biological tissue the functional effects that controlled mechanical stimuli induce on the electrophysiological activity of single neurons in neuronal tissue. Specifically, in this chapter (1) I report, for the first time, a depth-controlled mechanical characterization of the retinal tissue that highlights the viscoelastic nature of the sample; (2) I found that under specific configurations of mechanical stimulation, the spiking activity of retinal ganglion cell responses to light stimuli exhibited mechanical stimuli dependent modulations. These modulations were mostly spatially located in the neighborhood of the sites where the mechanical stimuli were delivered, and they are characterized by a time scale in the order of tenths of seconds. The two main advantages of this technique are the ability to explore the interplay between mechanical forces and electrical signaling in neuronal tissues and the possibility of identifying new insights on the relationship between altered mechanosensitive signaling, stiffness, and pathologies.

In conclusion, this thesis contributes to the field of Biophysics with the establishment of a novel method to explore the mechanical properties of tissues that combine micro indentation with Optical coherence tomography (**Chapter 2** and **3**). After providing details on how to fabricate a micrometer lens on top of an optical fiber to perform OCT imaging (**Chapter 4**), I demonstrated the feasibility of designing a new and complex fiber array OCT sensor combined with an indentation probe, by performing measurements on tissue mimic phantom (**Chapter 5**). Finally, I showed a new application of micro-indentation in combination with high-density multi-electrode array (HD-MEAs) recordings (**Chapter 6**). With this work, I provide the scientific community new avenues

to explore how mechanics interact with the structural properties of biological tissues and how it can modulate physiological processes both at the cellular and tissue level. Finally, I believe that this thesis strongly demonstrates the importance of approaching scientific questions from different perspectives by means of hybrid tools built from multidisciplinary research fields. The combination of traditional engineering knowledge (mechanical, chemical, and electrical engineering), together with biology, material science, physics, and medicine are all intertwined not only because a variety of technology is need for understanding nature at different length scale but also because knowing, making and interpret the result become one single convergent goal. Further advances in the method could, in the future, even result in pre-clinical diagnostics tools.





## References

- [1] K.H. Vining, D.J. Mooney, Mechanical forces direct stem cell behaviour in development and regeneration, *Nat. Rev. Mol. Cell Biol.* 18 (2017) 728–742. doi:10.1038/nrm.2017.108.
- [2] D. Ambrosi, M. Ben Amar, C.J. Cyron, A. DeSimone, A. Goriely, J.D. Humphrey, E. Kuhl, Growth and remodelling of living tissues: Perspectives, challenges and opportunities, *J. R. Soc. Interface.* 16 (2019). doi:10.1098/rsif.2019.0233.
- [3] Introductory biomechanics cells organisms | Bioengineering | Cambridge University Press, (n.d.). <https://www.cambridge.org/nl/academic/subjects/life-sciences/bioengineering/introductory-biomechanics-cells-organisms?format=HB&isbn=9780521841122> (accessed August 16, 2020).
- [4] T.W. Lu, C.F. Chang, Biomechanics of human movement and its clinical applications, *Kaohsiung J. Med. Sci.* 28 (2012) S13–S25. doi:10.1016/j.kjms.2011.08.004.
- [5] M. Marrese, V. Guarino, L. Ambrosio, Microscopic Approach for Testing Mechanical Properties of Hard Tissues, in: *Ref. Modul. Mater. Sci. Mater. Eng.*, Elsevier, 2016. doi:10.1016/b978-0-12-803581-8.02260-8.
- [6] V.M. Weaver, Cell and tissue mechanics: The new cell biology frontier, *Mol. Biol. Cell.* 28 (2017) 1815–1818. doi:10.1091/mbc.E17-05-0320.
- [7] E. Moeendarbary, A.R. Harris, Cell mechanics: principles, practices, and prospects, *Wiley Interdiscip. Rev. Syst. Biol. Med.* 6 (2014) 371–388. doi:10.1002/wsbm.1275.
- [8] N.D. Evans, E. Gentleman, The role of material structure and mechanical properties in cell-matrix interactions, *J. Mater. Chem. B.* 2 (2014) 2345–2356. doi:10.1039/c3tb21604g.
- [9] A. Kumar, J.K. Placone, A.J. Engler, Understanding the extracellular forces that determine cell fate and maintenance, *Dev.* 144 (2017) 4261–4270. doi:10.1242/dev.158469.
- [10] M. Urbanczyk, S.L. Layland, K. Schenke-Layland, The role of extracellular matrix in biomechanics and its impact on bioengineering of cells and 3D tissues, *Matrix Biol.* 85–86 (2020) 1–14. doi:10.1016/j.matbio.2019.11.005.
- [11] G. Bao, R.D. Kamm, W. Thomas, W. Hwang, D.A. Fletcher, A.J. Grodzinsky, C. Zhu, M.R.K. Mofrad, Molecular biomechanics: The molecular basis of how forces regulate cellular function, *Cell. Mol. Bioeng.* 3 (2010) 91–105. doi:10.1007/s12195-010-0109-z.
- [12] L.M. Riou, A. Broisat, C. Ghezzi, G. Finet, G. Rioufol, A.M. Gharib, R.I. Pettigrew, J. Ohayon, Effects of mechanical properties and atherosclerotic artery size on biomechanical plaque disruption - Mouse vs. human, *J. Biomech.* 47 (2014) 765–772. doi:10.1016/j.jbiomech.2014.01.020.
- [13] F. Guilak, Biomechanical factors in osteoarthritis, *Best Pract. Res. Clin. Rheumatol.* 25 (2011) 815–823. doi:10.1016/j.berh.2011.11.013.
- [14] G. Osterhoff, E.F. Morgan, S.J. Shefelbine, L. Karim, L.M. McNamara, P. Augat, Bone mechanical properties and changes with osteoporosis, *Injury.* 47 (2016) S11–S20. doi:10.1016/S0020-1383(16)47003-8.

- [15] J.M. Northcott, I.S. Dean, J.K. Mouw, V.M. Weaver, Feeling stress: The mechanics of cancer progression and aggression, *Front. Cell Dev. Biol.* 6 (2018) 17. doi:10.3389/fcell.2018.00017.
- [16] M. CT, The fundamental role of mechanical properties in the progression of cancer disease and inflammation, *Rep. Prog. Phys.* 77 (2014). doi:10.1088/0034-4885/77/7/076602.
- [17] J.C. Downs, M.D. Roberts, C.F. Burgoyne, Mechanical environment of the optic nerve head in glaucoma., *Optom. Vis. Sci.* 85 (2008) 425–35. doi:10.1097/OPX.0b013e31817841cb.
- [18] B. Coudrillier, J.K. Pijanka, J.L. Jefferys, A. Goel, H.A. Quigley, C. Boote, T.D. Nguyen, Glaucoma-related changes in the mechanical properties and collagen micro-architecture of the human sclera, *PLoS One.* 10 (2015). doi:10.1371/journal.pone.0131396.
- [19] B. Coudrillier, J. Tian, S. Alexander, K.M. Myers, H.A. Quigley, T.D. Nguyen, Biomechanics of the human posterior sclera: Age- and glaucoma-related changes measured using inflation testing, *Investig. Ophthalmol. Vis. Sci.* 53 (2012) 1714–1728. doi:10.1167/iovs.11-8009.
- [20] L. Wullkopf, A.K. V. West, N. Leijnse, T.R. Cox, C.D. Madsen, L.B. Oddershede, J.T. Erler, Cancer cells' ability to mechanically adjust to extracellular matrix stiffness correlates with their invasive potential, *Mol. Biol. Cell.* 29 (2018) 2378–2385. doi:10.1091/mbc.E18-05-0319.
- [21] C. Walker, E. Mojares, A. Del Río Hernández, Role of extracellular matrix in development and cancer progression, *Int. J. Mol. Sci.* 19 (2018). doi:10.3390/ijms19103028.
- [22] M.R. VanLandingham, Review of instrumented indentation, *J. Res. Natl. Inst. Stand. Technol.* 108 (2003) 249–265. doi:10.6028/jres.108.024.
- [23] E. Broitman, Indentation Hardness Measurements at Macro-, Micro-, and Nanoscale: A Critical Overview, *Tribol. Lett.* 65 (2017) 1–18. doi:10.1007/s11249-016-0805-5.
- [24] E. Rettler, S. Hoeppener, B.W. Sigusch, U.S. Schubert, Mapping the mechanical properties of biomaterials on different length scales: Depth-sensing indentation and AFM based nanoindentation, *J. Mater. Chem. B.* 1 (2013) 2789–2806. doi:10.1039/c3tb20120a.
- [25] D.M. Ebenstein, L.A. Pruitt, Nanoindentation of biological materials, *Nano Today.* 1 (2006) 26–33. doi:10.1016/S1748-0132(06)70077-9.
- [26] H. Hertz, On the contact of rigid elastic solids and on hardness, chapter 6: Assorted papers by H. Hertz, (1882).
- [27] H. Hertz, On the contact of solids — on the contact of rigid elastic solids and on hardness, *Misc. Pap.* (1896).
- [28] H. Hertz, On the contact of elastic solids, *Z. Reine Angew. Math.* (1881). <https://ci.nii.ac.jp/naid/10015562849/> (accessed August 9, 2020).
- [29] H. Ladjal, J.L. Hanus, A. Pillarisetti, C. Keefer, A. Ferreira, J.P. Desai, Atomic force microscopy-based single-cell indentation: Experimentation and finite element simulation, in: 2009 IEEE/RSJ Int. Conf. Intell. Robot. Syst. IROS 2009, 2009: pp. 1326–1332. doi:10.1109/IROS.2009.5354351.
- [30] S.R. Cohen, E. Kalfon-Cohen, Dynamic nanoindentation by instrumented

- nanindentation and force microscopy: A comparative review, Beilstein J. Nanotechnol. 4 (2013) 815–833. doi:10.3762/bjnano.4.93.
- [31] M.F. Doerner, W.D. Nix, A method for interpreting the data from depth-sensing indentation instruments, J. Mater. Res. 1 (1986) 601–609. doi:10.1557/JMR.1986.0601.
- [32] W.C. Oliver, G.M. Pharr, An improved technique for determining hardness and elastic modulus using load and displacement sensing indentation experiments, J. Mater. Res. 7 (1992) 1564–1583. doi:10.1557/jmr.1992.1564.
- [33] I.N. Sneddon, The relation between load and penetration in the axisymmetric boussinesq problem for a punch of arbitrary profile, Int. J. Eng. Sci. 3 (1965) 47–57. doi:10.1016/0020-7225(65)90019-4.
- [34] B. V. Derjaguin, V.M. Muller, Y.P. Toporov, Effect of contact deformations on the adhesion of particles, J. Colloid Interface Sci. 53 (1975) 314–326. doi:10.1016/0021-9797(75)90018-1.
- [35] K.L. Johnson, J.A. Greenwood, Adhesive Contact of Elastic Bodies: The JKR Theory, in: *Encycl. Tribol.*, Springer US, 2013: pp. 42–49. doi:10.1007/978-0-387-92897-5\_1086.
- [36] D. Maugis, Rupture and Adherence of Elastic Solids, in: 2000: pp. 133–202. doi:10.1007/978-3-662-04125-3\_3.
- [37] D. Maugis, Frictionless Elastic Contact, in: 2000: pp. 203–344. doi:10.1007/978-3-662-04125-3\_4.
- [38] D. Maugis, Contact, Adhesion, and Rupture of Elastic Solids, Springer, 2000. doi:10.1007/978-3-662-04125-3.
- [39] Y.M. Efremov, T. Okajima, A. Raman, Measuring viscoelasticity of soft biological samples using atomic force microscopy, Soft Matter. 16 (2019) 64–81. doi:10.1039/c9sm01020c.
- [40] T. MEIDAV, VISCOELASTIC PROPERTIES OF THE STANDARD LINEAR SOLID\*, Geophys. Prospect. 12 (1964) 80–99. doi:10.1111/j.1365-2478.1964.tb01891.x.
- [41] A. Morro, Modelling of viscoelastic materials and creep behaviour, Meccanica. 52 (2017) 3015–3021. doi:10.1007/s11012-016-0585-x.
- [42] M.L. Oyen, Nanoindentation of biological and biomimetic materials, Exp. Tech. 37 (2013) 73–87. doi:10.1111/j.1747-1567.2011.00716.x.
- [43] M.L. Oyen, R.F. Cook, A practical guide for analysis of nanoindentation data, J. Mech. Behav. Biomed. Mater. 2 (2009) 396–407. doi:10.1016/j.jmbbm.2008.10.002.
- [44] C.C. White, M.R. Vanlandingham, P.L. Drzal, N.K. Chang, S.H. Chang, Viscoelastic characterization of polymers using instrumented indentation. II. Dynamic testing, J. Polym. Sci. Part B Polym. Phys. 43 (2005) 1812–1824. doi:10.1002/polb.20455.
- [45] E.G. Herbert, W.C. Oliver, G.M. Pharr, Nanoindentation and the dynamic characterization of viscoelastic solids, J. Phys. D. Appl. Phys. 41 (2008). doi:10.1088/0022-3727/41/7/074021.
- [46] E.G. Herbert, G.M. Pharr, W.C. Oliver, B.N. Lucas, J.L. Hay, On the measurement of stress – strain curves by spherical indentation, 399 (2001) 331–335.
- [47] A.. Fischer-Cripps, A review of analysis methods for sub-micron indentation testing, Vacuum. 58 (2000) 569–585. doi:10.1016/S0042-207X(00)00377-8.



- [48] M. Marrese, V. Guarino, L. Ambrosio, Atomic Force Microscopy: A Powerful Tool to Address Scaffold Design in Tissue Engineering, *J. Funct. Biomater.* 8 (2017) 7. doi:10.3390/jfb8010007.
- [49] D. Chavan, T.C. Van De Watering, G. Gruca, J.H. Rector, K. Heeck, M. Slaman, D. Iannuzzi, Ferrule-top nanoindenter: An optomechanical fiber sensor for nanoindentation, *Rev. Sci. Instrum.* 83 (2012). doi:10.1063/1.4766959.
- [50] H. Van Hoorn, N.A. Kurniawan, G.H. Koenderink, D. Iannuzzi, Local dynamic mechanical analysis for heterogeneous soft matter using ferrule-top indentation, *Soft Matter*. 12 (2016) 3066–3073. doi:10.1039/c6sm00300a.
- [51] G. Gruca, S. De Man, M. Slaman, J.H. Rector, D. Iannuzzi, Ferrule-top micromachined devices: Design, fabrication, performance, *Meas. Sci. Technol.* 21 (2010) 094033. doi:10.1088/0957-0233/21/9/094033.
- [52] D. Chavan, G. Gruca, S. De Man, M. Slaman, J.H. Rector, K. Heeck, D. Iannuzzi, Ferrule-top atomic force microscope, *Rev. Sci. Instrum.* 81 (2010). doi:10.1063/1.3516044.
- [53] M. Marrese, N. Antonovaite, B.K.A. Nelemans, T.H. Smit, D. Iannuzzi, Micro-indentation and optical coherence tomography for the mechanical characterization of embryos: Experimental setup and measurements on chicken embryos, *Acta Biomater.* (2019). doi:10.1016/j.actbio.2019.07.056.
- [54] S. V. Beekmans, D. Iannuzzi, Characterizing tissue stiffness at the tip of a rigid needle using an opto-mechanical force sensor, *Biomed. Microdevices.* 18 (2016) 1–8. doi:10.1007/s10544-016-0039-1.
- [55] N. Antonovaite, S. V. Beekmans, E.M. Hol, W.J. Wadman, D. Iannuzzi, Regional variations in stiffness in live mouse brain tissue determined by depth-controlled indentation mapping, *Sci. Rep.* 8 (2018) 12517. doi:10.1038/s41598-018-31035-y.
- [56] G. Mattei, L. Cacopardo, A. Ahluwalia, Micro-Mechanical Viscoelastic Properties of Crosslinked Hydrogels Using the Nano-Epsilon Dot Method, *Materials (Basel)*. 10 (2017) 889. doi:10.3390/ma10080889.
- [57] D. Chavan, G. Gruca, T. van de Watering, K. Heeck, J. Rector, M. Slaman, D. Andres, B. Tiribilli, G. Margheri, D. Iannuzzi, Fiber-top and ferrule-top cantilevers for atomic force microscopy and scanning near field optical microscopy, *Proc. SPIE.* 8430 (2012) 84300Z-84300Z-8. doi:10.1117/12.922117.
- [58] D.P. Popescu, L.P. in. Choo-Smith, C. Flueraru, Y. Mao, S. Chang, J. Disano, S. Sherif, M.G. Sowa, Optical coherence tomography: Fundamental principles, instrumental designs and biomedical applications, *Biophys. Rev.* 3 (2011) 155–169. doi:10.1007/s12551-011-0054-7.
- [59] F.-M. Lu, Z. Yuan, PET/SPECT molecular imaging in clinical neuroscience: recent advances in the investigation of CNS diseases., *Quant. Imaging Med. Surg.* 5 (2015) 433–47. doi:10.3978/j.issn.2223-4292.2015.03.16.
- [60] R. Weissleder, U. Mahmood, Molecular imaging, *Radiology.* 219 (2001) 316–333. doi:10.1148/radiology.219.2.r01ma19316.
- [61] M. Wu, J. Shu, Multimodal Molecular Imaging: Current Status and Future Directions, *Contrast Media Mol. Imaging.* 2018 (2018). doi:10.1155/2018/1382183.
- [62] A.F. Fercher, W. Drexler, C.K. Hitzenberger, T. Lasser, Optical coherence tomography-principles and applications, 2003.

- [63] D. Huang, E.E.A. Swanson, C.P. Lin, J.S. Schuman, W.G. Stinson, W. Chang, M.R. Hee, T. Flotte, K. Gregory, C.A. Puliafito, A. et, et al., Optical coherence tomography., 1991. doi:10.1126/science.1957169.
- [64] E.H. Martinez-Lapiscina, S. Arnow, J.A. Wilson, S. Saidha, J.L. Preiningerova, T. Oberwahrenbrock, A.U. Brandt, L.E. Pablo, S. Guerrieri, I. Gonzalez, O. Outteryck, A.K. Mueller, P. Albrecht, W. Chan, S. Lukas, L.J. Balk, C. Fraser, J.L. Frederiksen, J. Resto, T. Frohman, C. Cordano, I. Zubizarreta, M. Andorra, B. Sanchez-Dalmau, A. Saiz, R. Bermel, A. Klistorner, A. Petzold, S. Schippling, F. Costello, O. Aktas, P. Vermersch, C. Oreja-Guevara, G. Comi, L. Leocani, E. Garcia-Martin, F. Paul, E. Havrdova, E. Frohman, L.J. Balcer, A.J. Green, P.A. Calabresi, P. Villoslada, Retinal thickness measured with optical coherence tomography and risk of disability worsening in multiple sclerosis: A cohort study, *Lancet Neurol.* 15 (2016) 574–584. doi:10.1016/S1474-4422(16)00068-5.
- [65] M. Mogensen, L. Thrane, T.M. Jørgensen, P.E. Andersen, G.B.E. Jemec, OCT imaging of skin cancer and other dermatological diseases, *J. Biophotonics.* 2 (2009) 442–451. doi:10.1002/jbio.200910020.
- [66] N.D. Gladkova, G.A. Petrova, N.K. Nikulin, S.G. Radenska-Lopovok, L.B. Snopova, Y.P. Chumakov, V.A. Nasonova, V.M. Gelikonov, G. V. Gelikonov, R. V. Kuranov, A.M. Sergeev, F.I. Feldchtein, In vivo optical coherence tomography imaging of human skin: norm and pathology, *Ski. Res. Technol.* 6 (2000) 6–16. doi:10.1034/j.1600-0846.2000.006001006.x.
- [67] M. Mogensen, L. Thrane, T.M. Joergensen, P.E. Andersen, G.B.E. Jemec, Optical Coherence Tomography for Imaging of Skin and Skin Diseases, *Semin. Cutan. Med. Surg.* 28 (2009) 196–202. doi:10.1016/j.sder.2009.07.002.
- [68] Y.S. Hsieh, Y.C. Ho, S.Y. Lee, C.C. Chuang, J. che Tsai, K.F. Lin, C.W. Sun, Dental optical coherence tomography, *Sensors (Basel).* 13 (2013) 8928–8949. doi:10.3390/s130708928.
- [69] M. Satue, J. Obis, M.J. Rodrigo, S. Otin, M.I. Fuertes, E. Vilades, H. Gracia, J.R. Ara, R. Alarcia, V. Polo, J.M. Larrosa, L.E. Pablo, E. Garcia-Martin, Optical Coherence Tomography as a Biomarker for Diagnosis, Progression, and Prognosis of Neurodegenerative Diseases, *J. Ophthalmol.* 2016 (2016). doi:10.1155/2016/8503859.
- [70] J. Doustar, T. Torbati, K.L. Black, Y. Koronyo, M. Koronyo-Hamaoui, Optical coherence tomography in Alzheimer's disease and other neurodegenerative diseases, *Front. Neurol.* 8 (2017). doi:10.3389/fneur.2017.00701.
- [71] J.M. Larrosa, E. Garcia-Martin, M.P. Bambo, J. Pinilla, V. Polo, S. Otin, M. Satue, R. Herrero, L.E. Pablo, Potential new diagnostic tool for Alzheimer's disease using a linear Discriminant function for Fourier domain optical coherence tomography, *Investig. Ophthalmol. Vis. Sci.* 55 (2014) 3043–3051. doi:10.1167/iovs.13-13629.
- [72] M.U. Farooq, A. Khasnis, A. Majid, M.Y. Kassab, The role of optical coherence tomography in vascular medicine, *Vasc. Med.* 14 (2009) 63–71. doi:10.1177/1358863X08095153.
- [73] Y. Jiaa, S.T. Baileya, T.S. Hwanga, S.M. McClintica, S.S. Gaoa, M.E. Pennesia, C.J. Flaxela, A.K. Lauera, D.J. Wilsona, J. Hornegegerb, J.G. Fujimoto, D. Huanga, Quantitative optical coherence tomography angiography of vascular

- abnormalities in the living human eye, *Proc. Natl. Acad. Sci. U. S. A.* 112 (2015) E2395–E2402. doi:10.1073/pnas.1500185112.
- [74] R.F. Spaide, J.G. Fujimoto, N.K. Waheed, S.R. Sadda, G. Staurengi, Optical coherence tomography angiography, *Prog. Retin. Eye Res.* 64 (2018) 1–55. doi:10.1016/j.preteyeres.2017.11.003.
- [75] J. Fujimoto, E.S.-I. ophthalmology & visual, undefined 2016, The development, commercialization, and impact of optical coherence tomography, *Tvst.Arvojournals.Org.* (n.d.). <https://tvst.arvojournals.org/article.aspx?articleid=2536019> (accessed August 9, 2020).
- [76] J.F. de Boer, B. Cense, B.H. Park, M.C. Pierce, G.J. Tearney, B.E. Bouma, Improved signal-to-noise ratio in spectral-domain compared with time-domain optical coherence tomography, *Opt. Lett.* 28 (2003) 2067. doi:10.1364/OL.28.002067.
- [77] J. Walther, M. Gaertner, P. Cimalla, A. Burkhardt, L. Kirsten, S. Meissner, E. Koch, Optical coherence tomography in biomedical research, *Anal. Bioanal. Chem.* 400 (2011) 2721–2743. doi:10.1007/s00216-011-5052-x.
- [78] S. Aumann, S. Donner, J. Fischer, F. Müller, Optical Coherence Tomography (OCT): Principle and Technical Realization, in: *High Resolut. Imaging Microsc. Ophthalmol.*, Springer International Publishing, 2019: pp. 59–85. doi:10.1007/978-3-030-16638-0\_3.
- [79] A.G. Podoleanu, Optical coherence tomography, *J. Microsc.* 247 (2012) 209–219. doi:10.1111/j.1365-2818.2012.03619.x.
- [80] R. Leitgeb, C. Hitzenberger, A.F.-O. express, undefined 2003, Performance of fourier domain vs. time domain optical coherence tomography, *Osapublishing.Org.* (n.d.). <https://www.osapublishing.org/abstract.cfm?uri=oe-11-8-889> (accessed August 9, 2020).
- [81] A.B. Vakhtin, D.J. Kane, W.R. Wood, K. a Peterson, Common-path interferometer for frequency-domain optical coherence tomography., *Appl. Opt.* 42 (2003) 6953–6958. doi:10.1364/AO.42.006953.
- [82] K. Zhang, J.U. Kang, Common-path low-coherence interferometry fiber-optic sensor guided microincision, *J. Biomed. Opt.* 16 (2011) 095003. doi:10.1117/1.3622492.
- [83] K. Singh, D. Yamada, G. Tearney, Common Path Side Viewing Monolithic Ball Lens Probe for Optical Coherence Tomography, *Sovrem. Tehnol. v Med.* 7 (2015) 29–33. doi:10.17691/stm2015.7.1.04.
- [84] K.M. Tan, M. Mazilu, T.H. Chow, W.M. Lee, K. Taguchi, B.K. Ng, W. Sibbett, C.S. Herrington, C.T.A. Brown, K. Dholakia, T. Flotte, K. Gregory, C.A. Puliafito, J.G. Fujimoto, O. Coherence, In-fiber common-path optical coherence tomography using a conical-tip fiber, 17 (2009) 2231–2235.
- [85] Y. Verma, P. Nandi, K.D. Rao, M. Sharma, P.K. Gupta, Use of common path phase sensitive spectral domain optical coherence tomography for refractive index measurements, *Appl. Opt.* 50 (2011) E7. doi:10.1364/AO.50.0000E7.
- [86] K. Zhang, E. Katz, D.H. Kim, J.U. Kang, I.K. Ilev, Common-path optical coherence tomography guided fibre probe for spatially precise optical nerve stimulation, *Electron. Lett.* 46 (2010) 118. doi:10.1049/el.2010.3221.

- [87] A.B. Schwartz, Movement: How the Brain Communicates with the World, *Cell*. 164 (2016) 1122–1135. doi:10.1016/j.cell.2016.02.038.
- [88] Neuronal Activity - an overview | ScienceDirect Topics, (n.d.). <https://www.sciencedirect.com/topics/neuroscience/neuronal-activity> (accessed August 9, 2020).
- [89] J.A. Assad, L. Berdondini, L. Cancedda, F. De Angelis, A. Diaspro, M. Dipalo, T. Fellin, A. Maccione, S. Panzeri, L. Sileo, Brain function: Novel technologies driving novel understanding, in: *Bioinspired Approaches Human-Centric Technol.*, Springer International Publishing, 2014: pp. 299–334. doi:10.1007/978-3-319-04924-3\_10.
- [90] B. He, L. Yang, C. Wilke, H. Yuan, Electrophysiological imaging of brain activity and connectivity-challenges and opportunities, *IEEE Trans. Biomed. Eng.* 58 (2011) 1918–1931. doi:10.1109/TBME.2011.2139210.
- [91] M.E.J. Obien, K. Deligkaris, T. Bullmann, D.J. Bakkum, U. Frey, Revealing neuronal function through microelectrode array recordings, *Front. Neurosci.* 9 (2015) 423. doi:10.3389/fnins.2014.00423.
- [92] D.J. Bakkum, U. Frey, M. Radivojevic, T.L. Russell, J. Müller, M. Fiscella, H. Takahashi, A. Hierlemann, Tracking axonal action potential propagation on a high-density microelectrode array across hundreds of sites, *Nat. Commun.* 4 (2013). doi:10.1038/ncomms3181.
- [93] L. Berdondini, P.D. Van Der Wal, O. Guenat, N.F. De Rooij, M. Koudelka-Hep, P. Seitz, R. Kaufmann, P. Metzler, N. Blanc, S. Rohr, High-density electrode array for imaging in vitro electrophysiological activity, *Biosens. Bioelectron.* 21 (2005) 167–174. doi:10.1016/j.bios.2004.08.011.
- [94] L. Berdondini, T. Overstolz, N.F. De Rooij, M. Koudelka-Hep, M. Wány, P. Seitz, High-density microelectrode arrays for electrophysiological activity imaging of neuronal networks, in: *Proc. IEEE Int. Conf. Electron. Circuits, Syst.*, 2001: pp. 1239–1242. doi:10.1109/icecs.2001.957439.
- [95] L. Berdondini, K. Imfeld, A. MacCione, M. Tedesco, S. Neukom, M. Koudelka-Hep, S. Martinoia, Active pixel sensor array for high spatio-temporal resolution electrophysiological recordings from single cell to large scale neuronal networks, *Lab Chip*. 9 (2009) 2644–2651. doi:10.1039/b907394a.
- [96] G. Hilgen, M. Sorbaro, S. Pirmoradian, J.O. Muthmann, I.E. Kepiro, S. Ullo, C.J. Ramirez, A. Puente Encinas, A. Maccione, L. Berdondini, V. Murino, D. Sona, F. Cella Zanicchi, E. Sernagor, M.H. Hennig, Unsupervised Spike Sorting for Large-Scale, High-Density Multielectrode Arrays, *Cell Rep.* 18 (2017) 2521–2532. doi:10.1016/j.celrep.2017.02.038.
- [97] A. Maccione, M. Gandolfo, S. Zordan, H. Amin, S. Di Marco, T. Nieuw, G.N. Angotzi, L. Berdondini, Microelectronics, bioinformatics and neurocomputation for massive neuronal recordings in brain circuits with large scale multielectrode array probes, *Brain Res. Bull.* 119 (2015) 118–126. doi:10.1016/j.brainresbull.2015.07.008.
- [98] A. Maccione, M.H. Hennig, M. Gandolfo, O. Muthmann, J. van Coppenhagen, S.J. Eglen, L. Berdondini, E. Sernagor, Following the ontogeny of retinal waves: Pan-retinal recordings of population dynamics in the neonatal mouse, *J. Physiol.* 592 (2014) 1545–1563. doi:10.1113/jphysiol.2013.262840.

- [99] H. Amin, A. Maccione, F. Marinaro, S. Zordan, T. Nieuw, L. Berdondini, Electrical responses and spontaneous activity of human iPS-derived neuronal networks characterized for 3-month culture with 4096-electrode arrays, *Front. Neurosci.* 10 (2016). doi:10.3389/fnins.2016.00121.
- [100] M. Marrese, D. Lonardoni, F. Boi, H. van Hoorn, A. Maccione, S. Zordan, D. Iannuzzi, L. Berdondini, Investigating the effects of mechanical stimulation on retinal ganglion cell spontaneous spiking activity, *Front. Neurosci.* 13 (2019) 1–13. doi:10.3389/fnins.2019.01023.
- [101] C.J. Miller, L.A. Davidson, The interplay between cell signalling and mechanics in developmental processes, *Nat. Rev. Genet.* 14 (2013) 733–744. doi:10.1038/nrg3513.
- [102] M.A. Wozniak, C.S. Chen, Mechanotransduction in development: a growing role for contractility., *Nat. Rev. Mol. Cell Biol.* 10 (2009) 34–43. doi:10.1038/nrm2592.
- [103] V.D. Varner, D.A. Voronov, L.A. Taber, Mechanics of head fold formation: investigating tissue-level forces during early development, *Development.* 137 (2010) 3801–3811. doi:10.1242/dev.054387.
- [104] V.D. Varner, L.A. Taber, Not just inductive: a crucial mechanical role for the endoderm during heart tube assembly., *Development.* 139 (2012) 1680–90. doi:10.1242/dev.073486.
- [105] P. Patwari, R.T. Lee, Mechanical control of tissue morphogenesis., *Circ. Res.* 103 (2008) 234–43. doi:10.1161/CIRCRESAHA.108.175331.
- [106] G.F. Oster, J.D. Murray, a K. Harris, Mechanical aspects of mesenchymal morphogenesis., *J. Embryol. Exp. Morphol.* 78 (1983) 83–125.
- [107] P.-A. Pouille, P. Ahmadi, A.-C. Brunet, E. Farge, Mechanical Signals Trigger Myosin II Redistribution and Mesoderm Invagination in *Drosophila* Embryos, *Sci. Signal.* 2 (2009) ra16–ra16. doi:10.1126/scisignal.2000098.
- [108] C.J. Miller, L.A. Davidson, The interplay between cell signalling and mechanics in developmental processes, *Nat. Rev. Genet.* 14 (2013) 733–744. doi:10.1038/nrg3513.
- [109] T. Mammoto, D.E. Ingber, Mechanical control of tissue and organ development., *Development.* 137 (2010) 1407–20. doi:10.1242/dev.024166.
- [110] J. Zhou, H.Y. Kim, L.A. Davidson, Actomyosin stiffens the vertebrate embryo during crucial stages of elongation and neural tube closure., *Development.* 136 (2009) 677–88. doi:10.1242/dev.026211.
- [111] M. von Dassow, L.A. Davidson, Natural variation in embryo mechanics: gastrulation in *Xenopus laevis* is highly robust to variation in tissue stiffness, *Dev. Dyn.* 238 (2009) 2–18. doi:10.1002/dvdy.21809.
- [112] M.T. Valentine, Z.E. Perlman, T.J. Mitchison, D.A. Weitz, Mechanical Properties of *Xenopus* Egg Cytoplasmic Extracts, *Biophys. J.* 88 (2005) 680–689. doi:10.1529/BIOPHYSJ.104.048025.
- [113] S.W. Moore, A fiber optic system for measuring dynamic mechanical properties of embryonic tissues, *IEEE Trans. Biomed. Eng.* 41 (1994) 45–50. doi:10.1109/10.277270.
- [114] E.A. Zamir, L.A. Taber, On the effects of residual stress in microindentation tests of soft tissue structures., *J. Biomech. Eng.* 126 (2004) 276–83. <http://www.ncbi.nlm.nih.gov/pubmed/15179859> (accessed October 17, 2018).

- [115] E.A. Zamir, L.A. Taber, Material properties and residual stress in the stage 12 chick heart during cardiac looping., *J. Biomech. Eng.* 126 (2004) 823–30. <http://www.ncbi.nlm.nih.gov/pubmed/15796341> (accessed October 17, 2018).
- [116] U. Agero, J.A. Glazier, M. Hosek, Bulk elastic properties of chicken embryos during somitogenesis, *Biomed. Eng. Online.* 9 (2010) 1–16. doi:10.1186/1475-925X-9-19.
- [117] N.R. Chevalier, E. Gazquez, S. Dufour, V. Fleury, Measuring the micromechanical properties of embryonic tissues, *Methods.* 94 (2016) 120–128. doi:10.1016/j.ymeth.2015.08.001.
- [118] M. Liebling, A.S. Forouhar, R. Wolleschensky, B. Zimmermann, R. Ankerhold, S.E. Fraser, M. Gharib, M.E. Dickinson, Rapid three-dimensional imaging and analysis of the beating embryonic heart reveals functional changes during development, *Dev. Dyn.* 235 (2006) 2940–2948. doi:10.1002/dvdy.20926.
- [119] J.R. Hove, R.W. Köster, A.S. Forouhar, G. Acevedo-Bolton, S.E. Fraser, M. Gharib, Intracardiac fluid forces are an essential epigenetic factor for embryonic cardiogenesis, *Nature.* 421 (2003) 172–177. doi:10.1038/nature01282.
- [120] E.A.V. Jones, M.H. Baron, S.E. Fraser, M.E. Dickinson, Measuring hemodynamic changes during mammalian development, *Am. J. Physiol. Circ. Physiol.* 287 (2004) H1561–H1569. doi:10.1152/ajpheart.00081.2004.
- [121] D.I. Hollnagel, P.E. Summers, S.S. Kollias, D. Poulikakos, Laser Doppler velocimetry (LDV) and 3D phase-contrast magnetic resonance angiography (PC-MRA) velocity measurements: Validation in an anatomically accurate cerebral artery aneurysm model with steady flow, *J. Magn. Reson. Imaging.* 26 (2007) 1493–1505. doi:10.1002/jmri.21179.
- [122] G. Xu, P.S. Kemp, Opening Angles and Material Properties of the Early Embryonic Chick Brain, *J. Biomech. Eng.* 132 (2010) 1–17. doi:10.1115/1.4000169.Opening.
- [123] L.A. Davidson, G.F. Oster, R.E. Keller, M.A.R. Koehl, Measurements of Mechanical Properties of the Blastula Wall Reveal Which Hypothesized Mechanisms of Primary Invagination Are Physically Plausible in the Sea Urchin *Strongylocentrotus purpuratus*, *Dev. Biol.* 209 (1999) 221–238. doi:10.1006/dbio.1999.9249.
- [124] D.S. Adams, R. Keller, M.A. Koehl, The mechanics of notochord elongation, straightening and stiffening in the embryo of *Xenopus laevis*, *Development.* 110 (1990) 115–30. <http://www.ncbi.nlm.nih.gov/pubmed/2081454> (accessed October 18, 2018).
- [125] H. Greven, K. Zanger, G. Schwinger, Mechanical properties of the skin of *Xenopus laevis* (Anura, Amphibia), *J. Morphol.* 224 (1995) 15–22. doi:10.1002/jmor.1052240103.
- [126] O. Luu, R. David, H. Ninomiya, R. Winklbauer, Large-scale mechanical properties of *Xenopus* embryonic epithelium, *Proc. Natl. Acad. Sci.* 108 (2011) 4000–4005. doi:10.1073/pnas.1010331108.
- [127] S.W. Moore, R.E. Keller, M.A. Koehl, The dorsal involuting marginal zone stiffens anisotropically during its convergent extension in the gastrula of *Xenopus laevis*, *Development.* 121 (1995).
- [128] P. Li, A. Liu, L. Shi, X. Yin, S. Rugonyi, R.K. Wang, Assessment of strain and strain

- rate in embryonic chick heart *in vivo* using tissue Doppler optical coherence tomography, *Phys. Med. Biol.* 56 (2011) 7081–7092. doi:10.1088/0031-9155/56/22/006.
- [129] H.-J. Ko, W. Tan, R. Stack, S.A. Boppart, Optical Coherence Elastography of Engineered and Developing Tissue, *Tissue Eng.* 12 (2006) 63–73. doi:10.1089/ten.2006.12.63.
- [130] K. V Larin, D.D. Sampson, Optical coherence elastography - OCT at work in tissue biomechanics [Invited], *Biomed. Opt. Express.* 8 (2017) 1172–1202. doi:10.1364/BOE.8.001172.
- [131] J.M. Schmitt, OCT elastography: imaging microscopic deformation and strain of tissue, *Opt. Express.* 3 (1998) 199. doi:10.1364/OE.3.000199.
- [132] B.A. Filas, G. Xu, L.A. Taber, Probing Regional Mechanical Properties of Embryonic Tissue Using Microindentation and Optical Coherence Tomography, in: *Methods Mol. Biol.*, 2015: pp. 3–16. doi:10.1007/978-1-4939-1164-6\_1.
- [133] R. Raghunathan, J. Zhang, C. Wu, J. Rippey, M. Singh, K. V Larin, G. Scarcelli, Evaluating biomechanical properties of murine embryos using Brillouin microscopy and optical coherence tomography., *J. Biomed. Opt.* 22 (2017) 1–6. doi:10.1117/1.JBO.22.8.086013.
- [134] R. Schlüßler, S. Möllmert, S. Abuhattum, G. Cojoc, P. Müller, K. Kim, C. Möckel, C. Zimmermann, J. Czarske, J. Guck, Mechanical Mapping of Spinal Cord Growth and Repair in Living Zebrafish Larvae by Brillouin Imaging., *Biophys. J.* 115 (2018) 911–923. doi:10.1016/j.bpj.2018.07.027.
- [135] P.-J. Wu, I. V. Kabakova, J.W. Ruberti, J.M. Sherwood, I.E. Dunlop, C. Paterson, P. Török, D.R. Overby, Water content, not stiffness, dominates Brillouin spectroscopy measurements in hydrated materials, *Nat. Methods.* 15 (2018) 561–562. doi:10.1038/s41592-018-0076-1.
- [136] G. Scarcelli, S.H. Yun, Reply to 'Water content, not stiffness, dominates Brillouin spectroscopy measurements in hydrated materials,' *Nat. Methods.* 15 (2018) 562–563. doi:10.1038/s41592-018-0075-2.
- [137] V. Hamburger, H.L. Hamilton, A series of normal stages in the development of the chick embryo, *Dev. Dyn.* 195 (1992) 231–272. doi:10.1002/aja.1001950404.
- [138] S.C. Chapman, J. Collignon, G.C. Schoenwolf, A. Lumsden, Improved method for chick whole-embryo culture using a filter paper carrier, *Dev. Dyn.* 220 (2001) 284–289. doi:10.1002/1097-0177(20010301)220:3<284::AID-DVDY1102>3.0.CO;2-5.
- [139] M. Schmitz, B.K.A. Nelemans, T.H. Smit, A Submerged Filter Paper Sandwich for Long-term &lt;em>Ex Ovo</em> Time-lapse Imaging of Early Chick Embryos, *J. Vis. Exp.* 2016 (2016) e54636. doi:10.3791/54636.
- [140] I. Palmeirim, D. Henrique, D. Ish-Horowicz, O. Pourquié, Avian hairy gene expression identifies a molecular clock linked to vertebrate segmentation and somitogenesis., *Cell.* 91 (1997) 639–48. <http://www.ncbi.nlm.nih.gov/pubmed/9393857> (accessed October 19, 2018).
- [141] H. Van Hoorn, N.A. Kurniawan, G.H. Koenderink, D. Iannuzzi, Local dynamic mechanical analysis for heterogeneous soft matter using ferrule-top indentation, *Soft Matter.* 12 (2016) 3066–3073. doi:10.1039/c6sm00300a.
- [142] D.C. Lin, D.I. Shreiber, E.K. Dimitriadis, F. Horkay, Spherical indentation of soft

- matter beyond the Hertzian regime: numerical and experimental validation of hyperelastic models, *Biomech. Model. Mechanobiol.* 8 (2009) 345–358. doi:10.1007/s10237-008-0139-9.
- [143] G. Gruca, S. de Man, M. Slaman, J.H. Rector, D. Iannuzzi, Ferrule-top micromachined devices: design, fabrication, performance, *Meas. Sci. Technol.* 21 (2010) 094033. doi:10.1088/0957-0233/21/9/094033.
- [144] N. Antonovaite, S. V Beekmans, E.M. Hol, W.J. Wadman, D. Iannuzzi, Regional variations in stiffness in live mouse brain tissue determined by depth-controlled indentation mapping, *Sci. Rep.* 8 (2018) 12517. doi:10.1038/s41598-018-31035-y.
- [145] D. Corallo, V. Trapani, P. Bonaldo, The notochord: structure and functions, *Cell. Mol. Life Sci.* 72 (2015) 2989–3008. doi:10.1007/s00018-015-1897-z.
- [146] S.F. Gilbert, Paraxial and Intermediate Mesoderm, in: *Dev. Biol.*, 10th ed., 2013: pp. 415–448. doi:10.1026/1616-3443.33.2.130.
- [147] G. Forgacs, R.A. Foty, Y. Shafrir, M.S. Steinberg, Viscoelastic properties of living embryonic tissues: A quantitative study, *Biophys. J.* 74 (1998) 2227–2234. doi:10.1016/S0006-3495(98)77932-9.
- [148] J. Yao, V.D. Varner, L.L. Brilli, J.M. Young, L.A. Taber, R. Perucchio, Viscoelastic Material Properties of the Myocardium and Cardiac Jelly in the Looping Chick Heart, *J. Biomech. Eng.* 134 (2012) 024502. doi:10.1115/1.4005693.
- [149] V. Fleury, N.R. Chevalier, F. Furfaro, J.-L. Duband, Buckling along boundaries of elastic contrast as a mechanism for early vertebrate morphogenesis, *Eur. Phys. J. E.* 38 (2015) 6. doi:10.1140/epje/i2015-15006-7.
- [150] B.F. Kennedy, K.M. Kennedy, A.L. Oldenburg, S.G. Adie, S.A. Boppart, D.D. Sampson, Optical Coherence Elastography, in: *Opt. Coherence Tomogr.*, Springer International Publishing, Cham, 2015: pp. 1007–1054. doi:10.1007/978-3-319-06419-2\_33.
- [151] J.L. HUTTER, J. CHEN, W.K. WAN, S. UNİYAL, M. LEABU, B.M.C. CHAN, Atomic force microscopy investigation of the dependence of cellular elastic moduli on glutaraldehyde fixation, *J. Microsc.* 219 (2005) 61–68. doi:10.1111/j.1365-2818.2005.01497.x.
- [152] J.H. Hoh, C.A. Schoenenberger, Surface morphology and mechanical properties of MDCK monolayers by atomic force microscopy, *J. Cell Sci.* 107 ( Pt 5) (1994) 1105–14. <http://www.ncbi.nlm.nih.gov/pubmed/7929621> (accessed March 20, 2019).
- [153] R. Thavarajah, V.K. Mudimbaimannar, J. Elizabeth, U.K. Rao, K. Ranganathan, Chemical and physical basics of routine formaldehyde fixation, *J. Oral Maxillofac. Pathol.* 16 (2012) 400–5. doi:10.4103/0973-029X.102496.
- [154] Y.; Ling, C.; Li, K.; Feng, R.; Duncan, R.; Eisma, Z.; Huang, G. Nabi, Effects of fixation and preservation on tissue elastic properties measured by quantitative optical coherence elastography (OCE), *J. Biomech.* 49 (2016) 1009. doi:10.1016/j.jbiomech.2016.02.013.
- [155] S.-O. Kim, J. Kim, T. Okajima, N.-J. Cho, Mechanical properties of paraformaldehyde-treated individual cells investigated by atomic force microscopy and scanning ion conductance microscopy, *Nano Converg.* 4 (2017) 5. doi:10.1186/s40580-017-0099-9.
- [156] Alan Mathison Turing, The chemical basis of morphogenesis, *Philos. Trans. R.*



- Soc. Lond. B. Biol. Sci. 237 (1952) 37–72. doi:10.1098/rstb.1952.0012.
- [157] N. Gjorevski, C.M. Nelson, The mechanics of development: Models and methods for tissue morphogenesis., *Birth Defects Res. C. Embryo Today*. 90 (2010) 193–202. doi:10.1002/bdrc.20185.
- [158] C.J. Miller, L.A. Davidson, The interplay between cell signalling and mechanics in developmental processes., *Nat. Rev. Genet.* 14 (2013) 733–44. doi:10.1038/nrg3513.
- [159] O. Pourquié, The segmentation clock: Converting embryonic time into spatial pattern, *Science* (80-. ). 301 (2003) 328–330. doi:10.1126/science.1085887.
- [160] D.E. Discher, P. Janmey, Y.L. Wang, Tissue cells feel and respond to the stiffness of their substrate, *Science* (80-. ). 310 (2005) 1139–1143. doi:10.1126/science.1116995.
- [161] A.J. Engler, S. Sen, H.L. Sweeney, D.E. Discher, Matrix Elasticity Directs Stem Cell Lineage Specification, *Cell*. 126 (2006) 677–689. doi:10.1016/j.cell.2006.06.044.
- [162] C.M. Lo, H.B. Wang, M. Dembo, Y.L. Wang, Cell movement is guided by the rigidity of the substrate, *Biophys. J.* 79 (2000) 144–152. doi:10.1016/S0006-3495(00)76279-5.
- [163] A.J. Engler, H.L. Sweeney, D.E. Discher, J.E. Schwarzbauer, Extracellular matrix elasticity directs stem cell differentiation, *J Musculoskelet. Neuronal Interact.* 7 (2007) 335.
- [164] Z.T. Calamari, J.K.H. Hu, O.D. Klein, Tissue Mechanical Forces and Evolutionary Developmental Changes Act Through Space and Time to Shape Tooth Morphology and Function, *BioEssays*. 40 (2018). doi:10.1002/bies.201800140.
- [165] T. Mammoto, A. Mammoto, Y. suke Torisawa, T. Tat, A. Gibbs, R. Derda, R. Mannix, M. de Bruijn, C.W. Yung, D. Huh, D.E. Ingber, Mechanochemical Control of Mesenchymal Condensation and Embryonic Tooth Organ Formation, *Dev. Cell*. 21 (2011) 758–769. doi:10.1016/j.devcel.2011.07.006.
- [166] B.J. Damon, N. V. Mezentseva, J.S. Kumaratilake, G. Forgacs, S.A. Newman, Limb bud and flank mesoderm have distinct “physical phenotypes” that may contribute to limb budding, *Dev. Biol.* 321 (2008) 319–330. doi:10.1016/j.ydbio.2008.06.018.
- [167] M. Zhu, H. Tao, M. Samani, M. Luo, X. Wang, S. Hopyan, Y. Sun, Spatial mapping of tissue properties in vivo reveals a 3D stiffness gradient in the mouse limb bud, *Proc. Natl. Acad. Sci. U. S. A.* 117 (2020) 4781–4791. doi:10.1073/pnas.1912656117.
- [168] Linnaeus, *Gallus gallus subsp. domesticus* (Linnaeus, 1758), (1758). <https://www.gbif.org/species/113256841> (accessed February 8, 2020).
- [169] V. Hamburger, H.L. Hamilton, A series of normal stages in the development of the chick embryo, *J. Morphol.* 88 (1951) 49–92. doi:10.1002/jmor.1050880104.
- [170] M. Schmitz, B.K.A. Nelemans, T.H. Smit, A Submerged Filter Paper Sandwich for Long-term Ex Ovo Time-lapse Imaging of Early Chick Embryos, (2016) e54636. doi:doi:10.3791/54636.
- [171] I. Palmeirim, D. Henrique, D. Ish-Horowicz, O. Pourquié, Avian hairy gene expression identifies a molecular clock linked to vertebrate segmentation and somitogenesis., *Cell*. 91 (1997) 639–48.

- [172] D.C. Lin, D.I. Shreiber, E.K. Dimitriadis, F. Horkay, Spherical indentation of soft matter beyond the Hertzian regime: Numerical and experimental validation of hyperelastic models, *Biomech. Model. Mechanobiol.* (2009). doi:10.1007/s10237-008-0139-9.
- [173] B. Bénazéraf, P. Francois, R.E. Baker, N. Denans, C.D. Little, O. Pourquié, A random cell motility gradient downstream of FGF controls elongation of an amniote embryo, *Nature*. 466 (2010) 248–252. doi:10.1038/nature09151.
- [174] G.F. Oster, J.D. Murray, A.K. Harris, Mechanical aspects of mesenchymal morphogenesis, *Development*. 78 (1983).
- [175] C.M. Cheney, J.W. Lash, An increase in cell-cell adhesion in the chick segmental plate results in a meristic pattern., *J. Embryol. Exp. Morphol.* 79 (1984) 1–10.
- [176] Y. Sato, K. Nagatoshi, A. Hamano, Y. Imamura, D. Huss, S. Uchida, R. Lansford, Basal filopodia and vascular mechanical stress organize fibronectin into pillars bridging the mesoderm-endoderm gap, *Dev.* 144 (2017) 281–291. doi:10.1242/dev.141259.
- [177] T.T.K. Vuong-Brender, M. Ben Amar, J. Pontabry, M. Labouesse, The interplay of stiffness and force anisotropies drives embryo elongation, *Elife*. 6 (2017). doi:10.7554/eLife.23866.
- [178] J.U. Kang, J.-H. Han, X. Liu, K. Zhang, Common-Path Optical Coherence Tomography for Biomedical Imaging and Sensing., *J. Opt. Soc. Korea*. 14 (2010) 1–13. doi:10.3807/JOSK.2010.14.1.001.
- [179] L. Liu, J.A. Gardecki, S.K. Nadkarni, J.D. Toussaint, Y. Yagi, B.E. Bouma, G.J. Tearney, Imaging the subcellular structure of human coronary atherosclerosis using micro-optical coherence tomography, *Nat. Med.* 17 (2011) 1010–1014. doi:10.1038/nm.2409.
- [180] X. Liu, M.J. Cobb, Y. Chen, M.B. Kimmey, X. Li, Rapid-scanning forward-imaging miniature endoscope for real-time optical coherence tomography, *Opt. Lett.* 29 (2004) 1763. doi:10.1364/OL.29.001763.
- [181] A.D. Aguirre, J. Sawinski, S.-W. Huang, C. Zhou, W. Denk, J.G. Fujimoto, High speed optical coherence microscopy with autofocus adjustment and a miniaturized endoscopic imaging probe, *Opt. Express*. 18 (2010) 4222. doi:10.1364/OE.18.004222.
- [182] J. Li, M. de Groot, F. Helderma, J. Mo, J.M.A. Daniels, K. Grünberg, T.G. Sutedja, J.F. de Boer, High speed miniature motorized endoscopic probe for optical frequency domain imaging, *Opt. Express*. 20 (2012) 24132. doi:10.1364/OE.20.024132.
- [183] K.M. Kennedy, B.F. Kennedy, R.A. McLaughlin, D.D. Sampson, Needle optical coherence elastography for tissue boundary detection, *Opt. Lett.* 37 (2012) 2310. doi:10.1364/OL.37.002310.
- [184] M.S. Jafri, R. Tang, C.-M. Tang, Optical coherence tomography guided neurosurgical procedures in small rodents, *J. Neurosci. Methods*. 176 (2009) 85–95. doi:10.1016/j.jneumeth.2008.08.038.
- [185] C. Sun, K.K.C. Lee, B. Vuong, M.D. Cusimano, A. Brukson, A. Mauro, N. Munce, B.K. Courtney, B.A. Standish, V.X.D. Yang, Intraoperative handheld optical coherence tomography forward-viewing probe: physical performance and preliminary animal imaging., *Biomed. Opt. Express*. 3 (2012) 1404–12.

- doi:10.1364/BOE.3.001404.
- [186] C. Song, D.Y. Park, P.L. Gehlbach, S.J. Park, J.U. Kang, Fiber-optic OCT sensor guided micro-forceps for microsurgery., *Biomed. Opt. Express*. 4 (2013) 1045–50. doi:10.1364/BOE.4.001045.
- [187] Y. Mao, S. Chang, S. Sherif, C. Flueraru, Graded-index fiber lens proposed for ultrasmall probes used in biomedical imaging, *Appl. Opt.* 46 (2007) 5887. doi:10.1364/AO.46.005887.
- [188] K.M. Joos, J.-H. Shen, Miniature real-time intraoperative forward-imaging optical coherence tomography probe., *Biomed. Opt. Express*. 4 (2013) 1342–50. doi:10.1364/BOE.4.001342.
- [189] W. Jung, W. Benalcazar, A. Ahmad, U. Sharma, H. Tu, S.A. Boppart, Numerical analysis of gradient index lens-based optical coherence tomography imaging probes, *J. Biomed. Opt.* 15 (2010) 066027. doi:10.1117/1.3523374.
- [190] J. Kim, J. Han, J. Jeong, S. Member, Common-Path Optical Coherence Tomography Using a Conical-Frustum-Tip Fiber Probe, *IEEE J. Sel. Top.* 20 (2014).
- [191] K.M. Tan, M. Mazilu, T.H. Chow, W.M. Lee, K. Taguchi, B.K. Ng, W. Sibbett, C.S. Herrington, C.T.A. Brown, K. Dholakia, In-fiber common-path optical coherence tomography using a conical-tip fiber, *Opt. Express*. 17 (2009) 2375. doi:10.1364/OE.17.002375.
- [192] P.N. Minh, T. Ono, Y. Haga, K. Inoue, M. Sasaki, K. Hane, M. Esashi, Bach fabrication of microlens at the end of optical fiber using self-photolithography and etching techniques, *Opt. Rev.* 10 (2003) 150–154. doi:10.1007/s10043-003-0150-4.
- [193] T. Okayama, H. Seki, Fabrication and evaluation of silica-based optical fiber probes by chemical etching method, *Opt. Rev.* 12 (2005) 25–28. doi:10.1007/s10043-005-0025-y.
- [194] K.M. Tan, M. Mazilu, T.H. Chow, W.M. Lee, K. Taguchi, B.K. Ng, W. Sibbett, C.S. Herrington, C.T.T.A. Brown, K. Dholakia, K. Taguchi, B.K. Ng, W. Sibbett, C.S. Herrington, C.T.T.A. Brown, K. Dholakia, T. Flotte, K. Gregory, C.A. Puliafito, J.G. Fujimoto, O. Coherence, In-fiber common-path optical coherence tomography using a conical-tip fiber, *Opt. Express*. 17 (2009) 2231–2235. doi:10.1364/OE.17.002375.
- [195] M. Zhao, Y. Huang, J.U. Kang, Sapphire ball lens-based fiber probe for common-path optical coherence tomography and its applications in corneal and retinal imaging, *Opt. Lett.* 37 (2012) 4835. doi:10.1364/OL.37.004835.
- [196] C.-P. Liang, J. Wierwille, T. Moreira, G. Schwartzbauer, M.S. Jafri, C.-M. Tang, Y. Chen, A forward-imaging needle-type OCT probe for image guided stereotactic procedures., *Opt. Express*. 19 (2011) 26283–94. doi:10.1364/OE.19.026283.
- [197] X. Fu, D. Patel, H. Zhu, G. MacLennan, Y.T. Wang, M.W. Jenkins, A.M. Rollins, Miniature forward-viewing common-path OCT probe for imaging the renal pelvis., *Biomed. Opt. Express*. 6 (2015) 1164–71. doi:10.1364/BOE.6.001164.
- [198] N.-E.E. Demagh, A. Guessoum, R. Zegari, T. Gharbi, Self-centring technique for fibre optic microlens mounting using a concave cone-etched fibre, *Meas. Sci. Technol.* 22 (2011) 115302. doi:10.1088/0957-0233/22/11/115302.
- [199] G.M. Philip, N.K. Viswanathan, Fabrication of negative micro axicons in optical

- fibers via chemical etching, *Int. Conf. Opt. Photonics*. (2009) 1–3.
- [200] N.E. Demagh, A. Guessoum, H. Aissat, Chemical etching of concave cone fibre ends for core fibre alignment, *Meas. Sci. Technol.* 17 (2006) 119–122. doi:10.1088/0957-0233/17/1/019.
- [201] M. Zhao, Y. Huang, J.U. Kang, Sapphire ball lens-based fiber probe for common-path optical coherence tomography and its applications in corneal and retinal imaging., *Opt. Lett.* 37 (2012) 4835–7. <http://www.ncbi.nlm.nih.gov/pubmed/23202062> (accessed August 17, 2018).
- [202] T. Pangaribuan, K. Yamada, S. Jiang, M. Ohtsu, H. Ohsawa, Reproducible fabrication technique of nanometric tip diameter fiber probe for photon Scanning Tunneling Microscope, *Jpn. J. Appl. Phys.* 31 (1992) L1302–L1304. doi:10.1143/JJAP.31.L1302.
- [203] V.M. Weaver, Cell and tissue mechanics: The new cell biology frontier, *Mol. Biol. Cell.* 28 (2017) 1815–1818. doi:10.1091/mbc.E17-05-0320.
- [204] G.T. Fallenstein, V.D. Hulce, J.W. Melvin, Dynamic mechanical properties of human brain tissue, *J. Biomech.* 2 (1969) 217–226. doi:10.1016/0021-9290(69)90079-7.
- [205] Y.M. Efremov, E.A. Pukhlyakova, D. V. Bagrov, K. V. Shaitan, Atomic force microscopy of living and fixed *Xenopus laevis* embryos, *Micron.* 42 (2011) 840–852. doi:10.1016/j.micron.2011.05.010.
- [206] M.R. Bonilla, J.R. Stokes, M.J. Gidley, G.E. Yakubov, Interpreting atomic force microscopy nanoindentation of hierarchical biological materials using multi-regime analysis, *Soft Matter.* 11 (2015) 1281–1292. doi:10.1039/c4sm02440k.
- [207] M. Dokukin, I. Sokolov, High-resolution high-speed dynamic mechanical spectroscopy of cells and other soft materials with the help of atomic force microscopy, *Sci. Rep.* 5 (2015) 1–14. doi:10.1038/srep12630.
- [208] A. Cartagena, A. Raman, Local viscoelastic properties of live cells investigated using dynamic and quasi-static atomic force microscopy methods, *Biophys. J.* 106 (2014) 1033–1043. doi:10.1016/j.bpj.2013.12.037.
- [209] G. Thomas, N.A. Burnham, T.A. Camesano, Q. Wen, Measuring the Mechanical Properties of Living Cells Using Atomic Force Microscopy, *J. Vis. Exp.* (2013) 1–8. doi:10.3791/50497.
- [210] D. Iannuzzi, K. Heeck, M. Slaman, S. De Man, J.H. Rector, H. Schreuders, J.W. Berenschot, V.J. Gadgil, R.G.P. Sanders, M.C. Elwenspoek, S. Deladi, Fibre-top cantilevers: Design, fabrication and applications, *Meas. Sci. Technol.* 18 (2007) 3247–3252. doi:10.1088/0957-0233/18/10/S30.
- [211] O. Wintner, N. Hirsch-Attas, M. Schlossberg, F. Brofman, R. Friedman, M. Kupervaser, D. Kitsberg, A. Buxboim, A Unified Linear Viscoelastic Model of the Cell Nucleus Defines the Mechanical Contributions of Lamins and Chromatin, *Adv. Sci.* 7 (2020) 1901222. doi:10.1002/advs.201901222.
- [212] A. Karoutas, W. Szymanski, T. Rausch, S. Guhathakurta, E.A. Rog-Zielinska, R. Peyronnet, J. Seyfferth, H.R. Chen, R. de Leeuw, B. Herquel, H. Kimura, G. Mittler, P. Kohl, O. Medalia, J.O. Korbel, A. Akhtar, The NSL complex maintains nuclear architecture stability via lamin A/C acetylation, *Nat. Cell Biol.* 21 (2019) 1248–1260. doi:10.1038/s41556-019-0397-z.
- [213] P.T.M. Albers, S.P.W. Govers, J. Laven, L.G.J. van der Ven, R.A.T.M. van

- Bentham, G. de With, A.C.C. Esteves, Design of dual hydrophobic–hydrophilic polymer networks for highly lubricious polyether-urethane coatings, *Eur. Polym. J.* 111 (2019) 82–94. doi:10.1016/j.eurpolymj.2018.12.004.
- [214] T.H. Qazi, D.J. Mooney, G.N. Duda, S. Geissler, Niche-mimicking interactions in peptide-functionalized 3D hydrogels amplify mesenchymal stromal cell paracrine effects, *Biomaterials*. 230 (2020) 119639. doi:10.1016/j.biomaterials.2019.119639.
- [215] X. Yue, T.D. Nguyen, V. Zellmer, S. Zhang, P. Zorlutuna, Stromal cell-laden 3D hydrogel microwell arrays as tumor microenvironment model for studying stiffness dependent stromal cell-cancer interactions, *Biomaterials*. 170 (2018) 37–48. doi:10.1016/j.biomaterials.2018.04.001.
- [216] G. Mattei, L. Cacopardo, A. Ahluwalia, Engineering Gels with Time-Evolving Viscoelasticity, *Materials (Basel)*. 13 (2020) 438. doi:10.3390/ma13020438.
- [217] D.T. Nguyen, N. Nagarajan, P. Zorlutuna, Effect of Substrate Stiffness on Mechanical Coupling and Force Propagation at the Infarct Boundary, *Biophys. J.* 115 (2018) 1966–1980. doi:10.1016/j.bpj.2018.08.050.
- [218] A.O. Moghaddam, J. Wei, J. Kim, A.C. Dunn, A.J. Wagoner Johnson, An indentation-based approach to determine the elastic constants of soft anisotropic tissues, *J. Mech. Behav. Biomed. Mater.* 103 (2020) 103539. doi:10.1016/j.jmbbm.2019.103539.
- [219] F. Martorina, C. Casale, F. Urciolo, P.A. Netti, G. Imparato, In vitro activation of the neuro-transduction mechanism in sensitive organotypic human skin model, *Biomaterials*. 113 (2017) 217–229. doi:10.1016/j.biomaterials.2016.10.051.
- [220] S.L. Arias, A. Shetty, J. Devorkin, J.P. Allain, Magnetic targeting of smooth muscle cells in vitro using a magnetic bacterial cellulose to improve cell retention in tissue-engineering vascular grafts, *Acta Biomater.* 77 (2018) 172–181. doi:10.1016/j.actbio.2018.07.013.
- [221] S.A. Xie, T. Zhang, J. Wang, F. Zhao, Y.P. Zhang, W.J. Yao, S.S. Hur, Y.T. Yeh, W. Pang, L.S. Zheng, Y.B. Fan, W. Kong, X. Wang, J.J. Chiu, J. Zhou, Matrix stiffness determines the phenotype of vascular smooth muscle cell in vitro and in vivo: Role of DNA methyltransferase 1, *Biomaterials*. 155 (2018) 203–216. doi:10.1016/j.biomaterials.2017.11.033.
- [222] A. Bokemeyer, P.R. Tepaspe, L. Quill, P. Lenz, E. Rijcken, M. Vieth, N. Ding, S. Ketelhut, F. Rieder, B. Kemper, D. Bettenworth, Quantitative Phase Imaging Using Digital Holographic Microscopy Reliably Assesses Morphology and Reflects Elastic Properties of Fibrotic Intestinal Tissue, *Sci. Rep.* 9 (2019) 1–11. doi:10.1038/s41598-019-56045-2.
- [223] C.Y. Chen, M.A. Caporizzo, K. Bedi, A. Vite, A.I. Bogush, P. Robison, J.G. Heffler, A.K. Salomon, N.A. Kelly, A. Babu, M.P. Morley, K.B. Margulies, B.L. Prosser, Suppression of deetyrosinated microtubules improves cardiomyocyte function in human heart failure, *Nat. Med.* 24 (2018) 1225–1233. doi:10.1038/s41591-018-0046-2.
- [224] E. Amann, P. Wolff, E. Breel, M. van Griensven, E.R. Balmayor, Hyaluronic acid facilitates chondrogenesis and matrix deposition of human adipose derived mesenchymal stem cells and human chondrocytes co-cultures, *Acta Biomater.* 52 (2017) 130–144. doi:10.1016/j.actbio.2017.01.064.

- [225] D. Chavan, J. Mo, M. de Groot, A. Meijering, J.F. de Boer, D. Iannuzzi, Collecting optical coherence elastography depth profiles with a micromachined cantilever probe, *Opt. Lett.* 38 (2013) 1476. doi:10.1364/OL.38.001476.
- [226] L. Bartolini, F. Feroldi, J.J.A. Weda, M. Slaman, J.F. De Boer, D. Iannuzzi, Multimodal probe for optical coherence tomography epidetection and micron-scale indentation, (2017). doi:10.1142/S179354581742007X.
- [227] M. Marrese, H. Offerhaus, E. Paardekam, D. Iannuzzi, 70  $\mu\text{m}$  diameter optical probe for common-path optical coherence tomography in air and liquids, *Opt. Lett.* 43 (2018) 5929. doi:10.1364/OL.43.005929.
- [228] L. Bartolini, D. Iannuzzi, G. Mattei, Comparison of frequency and strain-rate domain mechanical characterization, *Sci. Rep.* (2018). doi:10.1038/s41598-018-31737-3.
- [229] G.C. Reilly, A.J. Engler, Intrinsic extracellular matrix properties regulate stem cell differentiation, *J. Biomech.* (2010). doi:10.1016/j.jbiomech.2009.09.009.
- [230] V. Vogel, M. Sheetz, Local force and geometry sensing regulate cell functions, *Nat. Rev. Mol. Cell Biol.* (2006). doi:10.1038/nrm1890.
- [231] E.K.F. Yim, M.P. Sheetz, Force-dependent cell signaling in stem cell differentiation, *Stem Cell Res. Ther.* (2012). doi:10.1186/scrt132.
- [232] K.H. Vining, D.J. Mooney, Mechanical forces direct stem cell behaviour in development and regeneration, *Nat. Rev. Mol. Cell Biol.* (2017). doi:10.1038/nrm.2017.108.
- [233] M.R. Franz, D. Burkhoff, D.T. Yue, K. Sagawa, Mechanically induced action potential changes and arrhythmia in isolated and in situ canine hearts, *Cardiovasc. Res.* (1989). doi:10.1093/cvr/23.3.213.
- [234] L. Terracio, B. Miller, T.K. Borg, Effects of cyclic mechanical stimulation of the cellular components of the heart: In vitro, *Vitr. Cell. Dev. Biol.* (1988). doi:10.1007/BF02623815.
- [235] P. Kohl, C. Bollensdorff, A. Garny, Effects of mechanosensitive ion channels on ventricular electrophysiology: Experimental and theoretical models, *Exp. Physiol.* (2006). doi:10.1113/expphysiol.2005.031062.
- [236] H.R. Wirtz, L.G. Dobbs, The effects of mechanical forces on lung functions, *Respir. Physiol.* (2000). doi:10.1016/S0034-5687(99)00092-4.
- [237] J.M. Barnes, L. Przybyla, V.M. Weaver, Tissue mechanics regulate brain development, homeostasis and disease, *J. Cell Sci.* 130 (2017) 71–82. doi:10.1242/jcs.191742.
- [238] K. Franze, The Integration of Mechanical and Chemical Signalling in the Developing Brain, *Biophys. J.* 114 (2018) 19a. doi:10.1016/j.bpj.2017.11.146.
- [239] W.J. Tyler, The mechanobiology of brain function, *Nat. Rev. Neurosci.* 13 (2012) 867–878. doi:10.1038/nrn3383.
- [240] D. Ingber, Mechanobiology and diseases of mechanotransduction, *Ann. Med.* 35 (2003) 564–577. doi:10.1080/07853890310016333.
- [241] M.A. Hemphill, S. Dauth, C.J. Yu, B.E. Dabiri, K.K. Parker, Traumatic Brain Injury and the Neuronal Microenvironment: A Potential Role for Neuropathological Mechanotransduction, *Neuron* 85 (2015) 1177–1192. doi:10.1016/j.neuron.2015.02.041.
- [242] M.F. Marmor, Mechanisms of retinal adhesion, *Prog. Retin. Res.* 12 (1993) 179–

204. doi:10.1016/0278-4327(93)90009-l.
- [243] T. Wygnanski-Jaffe, C.J. Murphy, C. Smith, M. Kubai, P. Christopherson, C.R. Ethier, A. V. Levin, Protective ocular mechanisms in woodpeckers, *Eye*. 21 (2007) 83–89. doi:10.1038/sj.eye.6702163.
- [244] J.C.H. Tan, F.B. Kalapesi, M.T. Coroneo, Mechanosensitivity and the eye: Cells coping with the pressure, *Br. J. Ophthalmol.* 90 (2006) 383–388. doi:10.1136/bjo.2005.079905.
- [245] L. Bonomi, G. Marchini, M. Marraffa, R. Morbio, The relationship between intraocular pressure and glaucoma in a defined population: Data from the Egna-Neumarkt glaucoma study, *Ophthalmologica*. 215 (2001) 34–38. doi:10.1159/000050823.
- [246] R.M. Sappington, T. Sidorova, N.J. Ward, R. Chakravarthy, K.W. Ho, D.J. Calkins, Activation of transient receptor potential vanilloid-1 (TRPV1) influences how retinal ganglion cell neurons respond to pressure-related stress, *Channels*. 9 (2015) 102–113. doi:10.1080/19336950.2015.1009272.
- [247] M. Manivannan, P.K. Suresh, On the somatosensation of vision, *Ann. Neurosci.* 19 (2012) 31–39. doi:10.5214/ans.0972.7531.180409.
- [248] S.N. Skatchkov, M.J. Eaton, Y.M. Shuba, Y. V. Kucheryavykh, C. Derst, R.W. Veh, A. Wurm, I. Iandiev, T. Pannicke, A. Bringmann, A. Reichenbach, Tandem-pore domain potassium channels are functionally expressed in retinal (müller) glial cells, *Glia*. 53 (2006) 266–276. doi:10.1002/glia.20280.
- [249] D. Križaj, Polymodal sensory integration in retinal ganglion cells, in: *Adv. Exp. Med. Biol.*, Springer, Cham, 2016: pp. 693–698. doi:10.1007/978-3-319-17121-0\_92.
- [250] D.A. Ryskamp, P. Witkovsky, P. Barabas, W. Huang, C. Koehler, N.P. Akimov, S.H. Lee, S. Chauhan, W. Xing, R.C. Renteria, W. Liedtke, D. Krizaj, The Polymodal Ion Channel Transient Receptor Potential Vanilloid 4 Modulates Calcium Flux, Spiking Rate, and Apoptosis of Mouse Retinal Ganglion Cells, *J. Neurosci.* 31 (2011) 7089–7101. doi:10.1523/JNEUROSCI.0359-11.2011.
- [251] S. Agte, T. Pannicke, E. Ulbricht, A. Reichenbach, A. Bringmann, Two different mechanosensitive calcium responses in Müller glial cells of the guinea pig retina: Differential dependence on purinergic receptor signaling, *Glia*. 65 (2017) 62–74. doi:10.1002/glia.23054.
- [252] S.M. Munsaka, M. Agsalda, D. Troelstrup, N. Hu, Q. Yu, B. Shiramizu, Characteristics of activated monocyte phenotype support R5-tropic human immunodeficiency virus, *Immunol. Immunogenet. Insights*. 1 (2009) 15–20. doi:10.1007/978-1-62703-673-3.
- [253] N. Lindqvist, Q. Liu, J. Zajadacz, K. Franze, A. Reichenbach, Retinal Glial (Müller) Cells: Sensing and Responding to Tissue Stretch, *Investig. Ophthalmology Vis. Sci.* 51 (2010) 1683. doi:10.1167/iovs.09-4159.
- [254] O.J. Grüsser, U. Grüsser-Cornehls, R. Kusel, A.W. Przybyszewski, Responses of retinal ganglion cells to eyeball deformation: A neurophysiological basis for “pressure phosphenes,” *Vision Res.* 29 (1989) 181–194. doi:10.1016/0042-6989(89)90123-5.
- [255] C.M. Rountree, C. Meng, J.B. Troy, L. Saggere, Mechanical stimulation of the retina: Therapeutic feasibility and cellular mechanism, *IEEE Trans. Neural Syst.*

- Rehabil. Eng. 26 (2018) 1075–1083. doi:10.1109/TNSRE.2018.2822322.
- [256] M. Fujii, G.A. Sunagawa, M. Kondo, M. Takahashi, M. Mandai, Evaluation of micro Electroretinograms Recorded with Multiple Electrode Array to Assess Focal Retinal Function, *Sci. Rep.* 6 (2016) 30719. doi:10.1038/srep30719.
- [257] K. Franze, M. Francke, K. Günter, A.F. Christ, N. Kö rber, A. Reichenbach, J. Guck, Spatial mapping of the mechanical properties of the living retina using scanning force microscopy, *Soft Matter.* 7 (2011) 3147–3154. doi:10.1039/cosmo1017k.
- [258] H. Van Hoorn, N.A. Kurniawan, G.H. Koenderink, D. Iannuzzi, Local dynamic mechanical analysis for heterogeneous soft matter using ferrule-top indentation, *Soft Matter.* 12 (2016) 3066–3073. doi:10.1039/c6sm00300a.
- [259] N. Antonovaite, S. V. Beekmans, E.M. Hol, W.J. Wadman, D. Iannuzzi, Structure-stiffness relation of live mouse brain tissue determined by depth-controlled indentation mapping, (2018). doi:10.1038/s41598-018-31035-y.
- [260] S. V. Beekmans, D. Iannuzzi, A metrological approach for the calibration of force transducers with interferometric readout, *Surf. Topogr. Metrol. Prop.* 3 (2015) 025004. doi:10.1088/2051-672X/3/2/025004.
- [261] Hierarchical clustering (scipy.cluster.hierarchy) — SciPy v1.1.0 Reference Guide, (n.d.).
- [262] sklearn.metrics.silhouette\_score — scikit-learn 0.20.0 documentation, (n.d.).
- [263] S.M. Carcieri, Classification of Retinal Ganglion Cells: A Statistical Approach, *J. Neurophysiol.* 90 (2003) 1704–1713. doi:10.1152/jn.00127.2003.
- [264] scikit-learn: machine learning in Python — scikit-learn 0.20.2, (n.d.).
- [265] Y.-B. Lu, K. Franze, G. Seifert, C. Steinhauser, F. Kirchhoff, H. Wolburg, J. Guck, P. Janmey, E.-Q. Wei, J. Kas, A. Reichenbach, Viscoelastic properties of individual glial cells and neurons in the CNS, *Proc. Natl. Acad. Sci.* 103 (2006) 17759–17764. doi:10.1073/pnas.0606150103.
- [266] Z.H. Zhang, M.X. Pan, J.T. Cai, J.D. Weiland, K. Chen, Viscoelastic properties of the posterior eye of normal subjects, patients with age-related macular degeneration, and pigs, *J. Biomed. Mater. Res. - Part A.* 106 (2018) 2151–2157. doi:10.1002/jbm.a.36417.
- [267] R.E. Mahaffy, S. Park, E. Gerde, J. Käs, C.K. Shih, Quantitative Analysis of the Viscoelastic Properties of Thin Regions of Fibroblasts Using Atomic Force Microscopy, *Biophys. J.* (2004). doi:10.1016/S0006-3495(04)74245-9.
- [268] M. Hrapko, J.A.W. Van Dommelen, G.W.M. Peters, J.S.H.M. Wismans, The mechanical behaviour of brain tissue: Large strain response and constitutive modelling, in: *Int. Res. Counc. Biomech. Impact - 2005 Int. IRCOBI Conf. Biomech. Impact, Proc.*, 2005.
- [269] D.K. Temple, A.A. Cederlund, B.M. Lawless, R.M. Aspden, D.M. Espino, Viscoelastic properties of human and bovine articular cartilage: a comparison of frequency-dependent trends, *BMC Musculoskelet. Disord.* (2016). doi:10.1186/s12891-016-1279-1.
- [270] H.E. Burton, J.M. Freij, D.M. Espino, Dynamic Viscoelasticity and Surface Properties of Porcine Left Anterior Descending Coronary Arteries, *Cardiovasc. Eng. Technol.* (2017). doi:10.1007/s13239-016-0288-4.
- [271] F.B. Kalapesi, J.C. Tan, M.T. Coroneo, Stretch-activated channels: a mini-review. Are stretch-activated channels an ocular barometer?, *Clin. Exp. Ophthalmol.* 33



- (2005) 210–217. doi:10.1111/j.1442-9071.2005.00981.x.
- [272] E.A. Newman, K.R. Zahs, Calcium waves in retinal glial cells, *Science* (80-. ). 275 (1997) 844–845. doi:10.1126/science.275.5301.844.
- [273] E.A. Newman, K.R. Zahs, Modulation of neuronal activity by glial cells in the retina., *J. Neurosci.* 18 (1998) 4022–8.
- [274] M. Fujii, G.A. Sunagawa, M. Kondo, M. Takahashi, M. Mandai, Evaluation of micro Electroretinograms Recorded with Multiple Electrode Array to Assess Focal Retinal Function., *Sci. Rep.* 6 (2016) 30719. doi:10.1038/srep30719.
- [275] P.E. Crago, J.C. Houk, Z. Hasan, Regulatory actions of human stretch reflex, *J. Neurophysiol.* (1976). doi:10.1152/jn.1976.39.5.925.
- [276] C.C. Hunt, The effect of stretch receptors from muscle on the discharge of motoneurons, *J. Physiol.* (1952). doi:10.1113/jphysiol.1952.sp004754.
- [277] V.G. Chouvardas, A.N. Miliou, M.K. Hatalis, Tactile displays: Overview and recent advances, *Displays.* (2008). doi:10.1016/j.displa.2007.07.003.





## Publications list

1. Marrese, M. <sup>†</sup>, Antonovaite, N. <sup>†</sup>, Nelemans, B. K. A., Smit, T. H., and Iannuzzi, D. (2019) Micro-indentation and optical coherence tomography for the mechanical characterization of embryos: Experimental setup and measurements on chicken embryos. *Acta Biomater.* 97, 524–534 (**Chapter 2**)
2. Marrese, M., Antonovaite, N., Nelemans, B. K. A., Smit, T. H., and Iannuzzi, D. (2019) Micro-indentation and optical coherence tomography for the mechanical characterization of embryos: Experimental setup and measurements on chicken embryos. *The FASEB Journal.* 34, 12269–12277 (**Chapter 3**)
3. Marrese, M., Offerhaus, H., Paardekam, E., and Iannuzzi, D. (2018) 70  $\mu$  m diameter optical probe for common-path optical coherence tomography in air and liquids. *Opt. Lett.* 43, 5929 (**Chapter 4**)
4. Marrese, M., Paardekam, E., and Iannuzzi, D. (2020) Indentation probe with optical fiber array for Optical Coherence Tomography. Accepted with minor in *J. of Microscopy* (**Chapter 5**)
5. Marrese, M. <sup>†</sup>, Lonardoni, D. <sup>†</sup>, Boi, F. <sup>†</sup>, van Hoorn, H., Maccione, A., Zordan, S., Iannuzzi, D., and Berdondini, L. (2019) Investigating the effects of mechanical stimulation on retinal ganglion cell spontaneous spiking activity. *Front. Neurosci.* 13, 1–13 (**Chapter 6**)

<sup>†</sup> These authors contributed equally.



# Acknowledgments

The Ph.D. journey has been a roller coaster for me. In one single day, I experienced stress, depression, loneliness, sadness, joy, and excitement. The Ph.D. can be very difficult for many of us and full of doubts and insecurities due to all the challenges (scientific and not) we are up to every day. Naturally, one cannot undergo all this without help from many others. I want to express my gratitude to everybody who has helped me directly and indirectly, inside and outside the university, during this emotional, painful, yet rewarding scientific journey!

First of all, I would like to express my gratitude and appreciation to my supervisor **Davide Iannuzzi** for the opportunity to conduct the research for my doctoral thesis in his group. Thank you for the tremendous guidance, encouragement, and support during these years. I am particularly grateful to you for all the constructive feedback and your continuous help not only as a scientist but also as a person. In the beginning, I had a hard time understanding your way of doing science, but I suddenly realized my limits in understanding your envision of research. I admire your creativity and the ability to see the value in any kind of idea and create a new project (or patent!) out of it. Your effort was a major factor in bringing this work in its present form, thank you, **Davide**!

Secondly, I would like to thank all members of the committee for taking the time and effort to review this thesis and for their suggestions for the last improvements.

Then, I want to thank my paranymphs, **Luca** and **Nelda**. Over the years we have become such good friends, even if at the beginning you have not been the most welcoming people...

**Luca**, when I joined the group, I tried to interact immediately with you (since we are both Italians), but I remember your first words: "I am Italian, but I am in the Netherlands and I do not want to hang out with Italians also here". It did not take long for me to figure out that it was a huge lie :P! However, over the years we have become more than just good friends, and I am so happy that besides the different paths we took and the busy schedule we both have, we always try to find the time to spend together!

**Nelda**, I arrived in the Netherlands on a rainy Sunday in November, and I was supposed to meet you for the key to my new apartment... you never showed up and you did not answer the phone! I was so mad at you! However, during the years I had the chance to know you as a person and I enjoyed being your colleague but even more your friend. You are one of the most driven and competitive scientists I have ever met. I remember (almost) every long discussion in the office about new ideas and interesting small project to publish a paper on nature. Unfortunately, it never happened mostly because the ideas were generated on drunken nights and the morning after was always a bit fuzzy! Besides the work and our differences, we know that we can always rely on each other, even now!

**Steven** and **Kingson**, my dream team! Two completely different personalities but both able to make me smile on a sad evening in the lab! **Kingson**, I appreciated your calm, peaceful, and very precise way of working. You never complained about anything, but you were always there to listen to my complaints and to help me in the lab. **Steven**, a typically dutch Ph.D. student, always incredibly positive about everything. Over the years, you have become a mentor for me, and I will never forget our long conversations about football on Monday morning, and of course our coffee at 4 pm every day! Many great memories to cherish, let's make sure we keep on making new ones!

I also want to thank **Erik** and **Martin** for their support and helpful discussions, both the scientific and the nonscientific ones during the coffee break! **Erik**, thank you for also the wonderful time outside the university.

I cannot forget the time spent with the 'old Iannuzzi group'. **Hedde**, **Atta**, **Camiel**, and **Rene** you always gave me helpful advice, helped me with experiments and the planning of it, taught me handy tricks in the lab, with LabVIEW, and more. Thank you all!

Then, I would like to thank all other members of the whole section for the good research environment, the discussions in section meetings, and the super fun evenings. **Kari**, **Max**, **Fabio**, and **Mathi** thank you so much for offering me a drink every time I needed it! Sometimes, when nothing seemed to work, and I was hopeless I could find comfort in your office. There you were able to turn any depressing things into jokes! I enjoyed getting to know you guys and share many memorable evenings. **Andy**, **Ben**, **Liron**, **Judith**, **Bram**, **Laura**, **Ludo**, and the Other **Max**, thank you all for the friendly atmosphere. I wish you guys all the best and thanks again for all the good times! Many thanks also to my students for all the work during their internships.

Furthermore, I want to thank **Margherita** and **Agata**. My last year would never be the same without the coolest scientists of the VU. The parties, all the brunches, and dinners are one of my best memories. Thank you for all the funny moments and to be my friends, I know I can always count on you! Good luck with your Ph.D.

Thanks also to all my collaborators. **Ben** and **Theo**, for the wonderful work, carried out on chicken embryos and the countless discussions. **Fabio**, **Davide**, and **Stefano** thank you for introducing me to the MEAs, and for the amazing time at the IIT in Genova!

Last but not least, I am thankful for the support system I have had throughout the years: my family, friends, and loved ones (especially my beautiful twin nephews), who helped me deal with the obstacles and curveballs that come my way. My friends **Rossella** and **Matthias** with whom I spent almost all my spare time outside the university. To all my oldest friends who have been always supporting me beside the physical distances! And of course, to the only one who combines the rule of friend and family, husband and the love of my life: **Marco**. After 12 years together and besides some ups and downs, you have been always supporting me with love and without asking anything else in return. I love you!

**Mamma** e **Papà**, la dedica più grande è per voi. Il sacrificio di aver visto vostra figlia

andare via da casa per realizzarsi e farsi valere è impagabile. Nonostante la sofferenza di non avermi lì con voi non mi avete mai fatto pesare questa decisione. Al contrario mi avete sempre sostenuta e motivata. Senza di voi, non avrei mai raggiunto questo obiettivo. **Mamma**, questo ultimo anno è stato particolarmente difficile per tutta la famiglia, ma soprattutto per te. Sei una donna forte e sei e sarai sempre la mia ispirazione. Grazie per aver trovato le parole giuste per confortare me quando in realtà avrei dovuto farlo io. Siete la mia forza e non riuscirò mai a ringraziarvi abbastanza per tutti i sacrifici che avete fatto per me.

Mi sento di dedicare questa tesi ai miei due zii, **Sergio** e **Vincenzo** che purtroppo ci hanno lasciato prematuramente.